

HIGH-RESOLUTION ROTATION CURVES AND GALAXY MASS MODELS FROM THINGS

W. J. G. DE BLOK¹, F. WALTER², E. BRINKS³, C. TRACHTERNACH⁴, S.-H. OH⁵, AND R. C. KENNICUTT, JR.⁶

¹ Department of Astronomy, University of Cape Town, Rondebosch 7700, South Africa; edeblok@ast.uct.ac.za

² Max Planck Institute für Astronomie, Königstuhl 17, 69117 Heidelberg, Germany; walter@mpia.de

³ Centre for Astrophysics Research, Science & Technology Research Institute, University of Hertfordshire, Hatfield AL10 9AB, UK; e.brinks@herts.ac.uk

⁴ Astronomisches Institut, Ruhr-Universität Bochum, Universitätsstraße 150, 44780 Bochum, Germany; trichter@astro.rub.de

⁵ Research School of Astronomy & Astrophysics, Mount Stromlo Observatory, Cotter Road, Weston Creek, ACT 2611, Australia; seheon@mso.anu.edu.au

⁶ Institute of Astronomy, University of Cambridge, Madingley Road, Cambridge CB3 0HA, UK; robk@ast.cam.ac.uk

Received 2007 November 23; accepted 2008 July 23; published 2008 November 18

ABSTRACT

We present rotation curves of 19 galaxies from The H_I Nearby Galaxy Survey (THINGS). The high spatial and velocity resolution of THINGS make these the highest quality H_I rotation curves available to date for a large sample of nearby galaxies, spanning a wide range of H_I masses and luminosities. The high quality of the data allows us to derive the geometric and dynamical parameters using H_I data alone. We do not find any declining rotation curves unambiguously associated with a cut-off in the mass distribution out to the last measured point. The rotation curves are combined with 3.6 μ m data from the *Spitzer* Infrared Nearby Galaxies Survey to construct mass models. Our best-fit dynamical disk masses, derived from the rotation curves, are in good agreement with photometric disk masses derived from the 3.6 μ m images in combination with stellar population synthesis arguments and two different assumptions for the stellar initial mass function (IMF). We test the cold dark matter (CDM) motivated cusp model, and the observationally motivated central density core model and find that (independent of IMF) for massive, disk-dominated galaxies, all halo models fit apparently equally well; for low-mass galaxies, however, a core-dominated halo is clearly preferred over a cusp-like halo. The empirically derived densities of the dark matter halos of the late-type galaxies in our sample are half of what is predicted by CDM simulations, again independent of the assumed IMF.

Key words: dark matter – galaxies: dwarf – galaxies: fundamental parameters – galaxies: kinematics and dynamics – galaxies: spiral – galaxies: structure

1. INTRODUCTION

Early observations of the rotation curves of spiral galaxies clearly indicated the presence of “missing” matter in these objects (e.g., Bosma 1978; Rubin et al. 1978; Bosma 1981; see also Sofue & Rubin 2001). This “missing” or “dark” matter, as it is now more commonly called, has since become one of the pillars of modern cosmology. An elaborate framework, explaining and describing the properties of the Universe has been built, involving a cosmological constant, Λ , and a form of collisionless cold dark matter (CDM). The Λ CDM paradigm provides a comprehensive description of the Universe at large (as shown by the *Wilkinson Microwave Anisotropy Probe* (WMAP) results; see Spergel et al. 2007), but problems on smaller (galaxy) scales remain.

A well-known problem is that galaxy-scale structures formed in cosmological Λ CDM simulations are too compact. One symptom of this is the well-known missing satellite problem (simulations produce an overabundance of dwarf galaxy halos, cf., Moore et al. 1999a). This seems to have been alleviated somewhat by the recent discovery of many faint dwarfs in our Local Group—some of which seem to be dominated by dark matter—but the discrepancy is still significant (Simon & Geha 2007).

The so-called cusp-core discrepancy (the predicted dark matter density profiles in galaxy halos are too steep; cf., de Blok et al. 2001) is another manifestation of the (too) compact structures in CDM simulations. Galaxy rotation curves have in the last decade taken center stage in the debate about this problem. Going into some more detail, results from cosmological Λ CDM simulations suggest that the density profiles of dark matter halos should be nearly universal, independent of the mass of the halo. This density profile has a characteristic steep mass-density slope in the inner parts which can be approximated with a power-law $\rho \sim r^\alpha$ with $\alpha \lesssim -1$; this is the so-called “cusp”

(e.g., Navarro et al. 1996, 1997; Klypin et al. 2001; Hayashi et al. 2004; Diemand et al. 2005).

Extensive observational determinations of this inner mass-density distribution seem, however, to indicate that the mass-density profiles of dark matter halos can be better described using an approximately constant-density inner “core” ($\rho \sim r^\alpha$ with $\alpha \simeq 0$). This core has a typical size of order a kpc (e.g., Moore 1994; de Blok et al. 1996; de Blok & McGaugh 1997; de Blok et al. 2001; de Blok & Bosma 2002; Marchesini et al. 2002; Weldrake et al. 2003; Gentile et al. 2005; Kuzio de Naray et al. 2006; Gentile et al. 2007). The discrepancy between these two outcomes has been much debated, as the presence of cusps is a fundamental feature of current cosmological simulations, confirmed many times by large increases in resolution and computing power that have been achieved over the years.

A large part of this debate has focused on possible systematic effects in the observations. Resolution of the data, accuracy of the positions of centers of galaxies, as well as presence of noncircular motions have featured prominently in these discussions (e.g., Swaters 1999; van den Bosch et al. 2000; Swaters et al. 2000; Simon et al. 2003; Rhee et al. 2004). Nevertheless, multiple, repeated, independent long-slit measurements of rotation curves as well as analyses using two-dimensional optical velocity fields consistently yield results suggesting the presence of a dark matter core in the inner parts of disk galaxies (e.g., Marchesini et al. 2002; de Blok 2004; de Blok & Bosma 2002; Kuzio de Naray et al. 2006; Gentile et al. 2007; Spano et al. 2008).⁷

⁷ Note that the paper by Swaters et al. (2003), which is often quoted as an observational counter-example, states that their results “cannot rule out cusp slopes this steep,” but also that most of their rotation curves “are equally well or better explained by halos with constant density cores (Swaters et al. 2003, page 732).”

$\text{H}\alpha$ synthesis observations of disk galaxies would, in principle, be eminently suited to address this problem. The $\text{H}\alpha$ disks of galaxies have a higher filling factor than the often patchy $\text{H}\alpha$ distributions used for optical rotation curves. Measuring accurate velocities and modeling them across the entire, two-dimensional, filled $\text{H}\alpha$ disks is therefore one of the strengths of radio synthesis observations. This means that possible effects of noncircular motions, which may not always be recognized in one-dimensional slit observations, can be analyzed within the context of the surrounding rotating disk (Oh et al. 2008; Trachternach et al. 2008). Furthermore, a determination of the position of the dynamical center can be made, enabling a direct and independent comparison with the position of the photometric center (Trachternach et al. 2008). In short, the rotation curve, as well as the uncertainties that could affect it, can be constrained by the same observation.

The one major disadvantage which hitherto hampered making the fullest possible use of $\text{H}\alpha$ data in these analyses has been their modest angular resolution, especially when compared with optical observations: to directly address cosmologically relevant questions regarding the distribution of dark matter requires high spatial resolution. For example, unambiguously distinguishing between a core and a cusp requires physical resolutions better than ~ 1 kpc (de Blok 2004). Also, to determine the importance of noncircular motions within the disks of galaxies, one needs to resolve the size scales associated with features that cause these motions, such as bars, spiral arms, and oval distortions.

The majority of published $\text{H}\alpha$ synthesis observations have at best beam sizes $\gtrsim 15''$, meaning they can reach the desired sub-kpc resolution only out to distances of ~ 4 Mpc. This, of course, severely limits the number of galaxies available for study. The $\text{H}\alpha$ Nearby Galaxy Survey (THINGS) has addressed this by observing in $\text{H}\alpha$ a sample of 34 nearby galaxies at the desired sub-kpc resolution. To achieve this, it used the NRAO⁸ Very Large Array (VLA) in its B, C, and D configurations. The total observing time (including data retrieved from the archive) was ~ 500 hr. The maximum angular resolution that can be achieved with these data is $\sim 6''$ for robust weighting and $\sim 12''$ for natural weighting. The velocity resolution is 5.2 km s^{-1} or better. With the sample galaxies at distances between 2 and 15 Mpc, the typical linear resolution varies between ~ 100 and ~ 500 pc. For further discussion on the sample, aims, and scientific goals of THINGS, as well as the technical details of the observations, we refer to Walter et al. (2008).

The current paper focuses on the rotation curves of THINGS galaxies. We use a subsample of the THINGS galaxies (discussed in Section 2) and present their velocity fields, tilted-ring models, and the rotation curves. Additionally, we combine our $\text{H}\alpha$ data with $3.6 \mu\text{m}$ data from the *Spitzer* Infrared Nearby Galaxies Survey (SINGS; Kennicutt et al. 2003), and derive well-constrained stellar mass-to-light ratios for the stellar disks. We use these to investigate the mass distributions in the sample galaxies using core- and cusp-dominated dark matter halo models. A number of galaxies presented here have been observed in the past, in some cases as part of the pioneering work on $\text{H}\alpha$ rotation curves in the 1970s and 1980s,⁹ but this is the first time

that such a large sample of galaxies is analyzed and modeled in a uniform way at sub-kpc resolution.

In Section 2 we summarize the selection of our sample. Section 3 describes the creation of the velocity fields as well as the derivation of the rotation curves. Section 4 presents the rotation curves and velocity fields of the individual galaxies in more detail. In Section 5 the mass models are presented, and in Section 6 these models are discussed in more detail for individual galaxies. The results are discussed in Section 7 and summarized in Section 8. Technical aspects of the analysis are presented in the Appendix.

2. THE SAMPLE

Our goal in this paper is to derive rotation curves of THINGS galaxies which depend on a minimum amount of external information. That is, we aim to derive the geometrical and kinematical parameters of the galaxies (inclination (i), position angle (P.A.), rotation velocity, etc.) as much as possible from the THINGS $\text{H}\alpha$ data alone. This limits our analysis to rotationally dominated galaxies with favorable orientations. Although using additional information (such as derived from optical data) would, in principle, increase the number of THINGS galaxies for which a rotation curve can be determined, the unquantifiable systematic effects associated with this introduce their own difficulties, as discussed below.

There are practical upper and lower limits to the inclinations of galaxies for which one can reliably derive rotation curves using standard methods. At very high inclinations ($i \gtrsim 80^\circ$), the line-of-sight crosses a large range of projected velocities and it becomes difficult to quantify the typical rotation velocity (although not impossible; see, for example, Kregel & van der Kruit 2004). Such high-inclination galaxies are, however, not present in the THINGS sample.

At low inclinations, the practical limit lies at $\sim 40^\circ$ (Begeman 1987, 1989). At lower inclinations, the velocity dispersion of the gas starts to become an important contaminant. As rotation takes place in a two-dimensional disk, the line-of-sight (projected) component of this rotation velocity decreases in amplitude with decreasing inclination, whereas the contribution due to random motions, which take place in three dimensions, remains the same. This leads to unacceptably large uncertainties in the deprojected rotational velocity.

Independent of inclination, we also require our sample galaxies to be dominated by rotation. This is not the case for a small number of THINGS galaxies. These are M81dWA (Sargent et al. 1983) and M81dwB, as well as NGC 1569 (dynamics disturbed by a starburst; Stil & Israel 2002), NGC 3077 (heavily interacting with M81; Walter et al. 2002), and NGC 4449 (tidally disturbed; Hunter et al. 1999). We do not consider these galaxies further.

To quantify our sample selection further, we consider indicative $\text{H}\alpha$ inclinations derived from ellipse fits to the outer $\text{H}\alpha$ disks, in addition to optical inclinations from LEDA (Paturel et al. 2003). These values are listed in Table 1. In determining the $\text{H}\alpha$ inclinations, using the maps presented in Walter et al. (2008), care was taken that these fits were not affected by the tails, clouds, and other features often seen in the outer parts of the $\text{H}\alpha$ disks. The $\text{H}\alpha$ inclinations listed here are deemed to be as reliable as their optical counterparts, and, in some cases, even preferable (compare the values for DDO 154 and the associated images in Walter et al. 2008). We stress that determining precise values for these inclinations is not the issue here, as we merely use them to clarify our sample selection. They are not used for any subsequent dynamical analyses.

⁸ The National Radio Astronomy Observatory is a facility of the National Science Foundation operated under cooperative agreement by Associated Universities, Inc.

⁹ See for example, Figure 1 in Bosma (1981) for a proto-THINGS depiction of the velocity fields of 22 nearby spiral galaxies. Half of these are also part of THINGS.

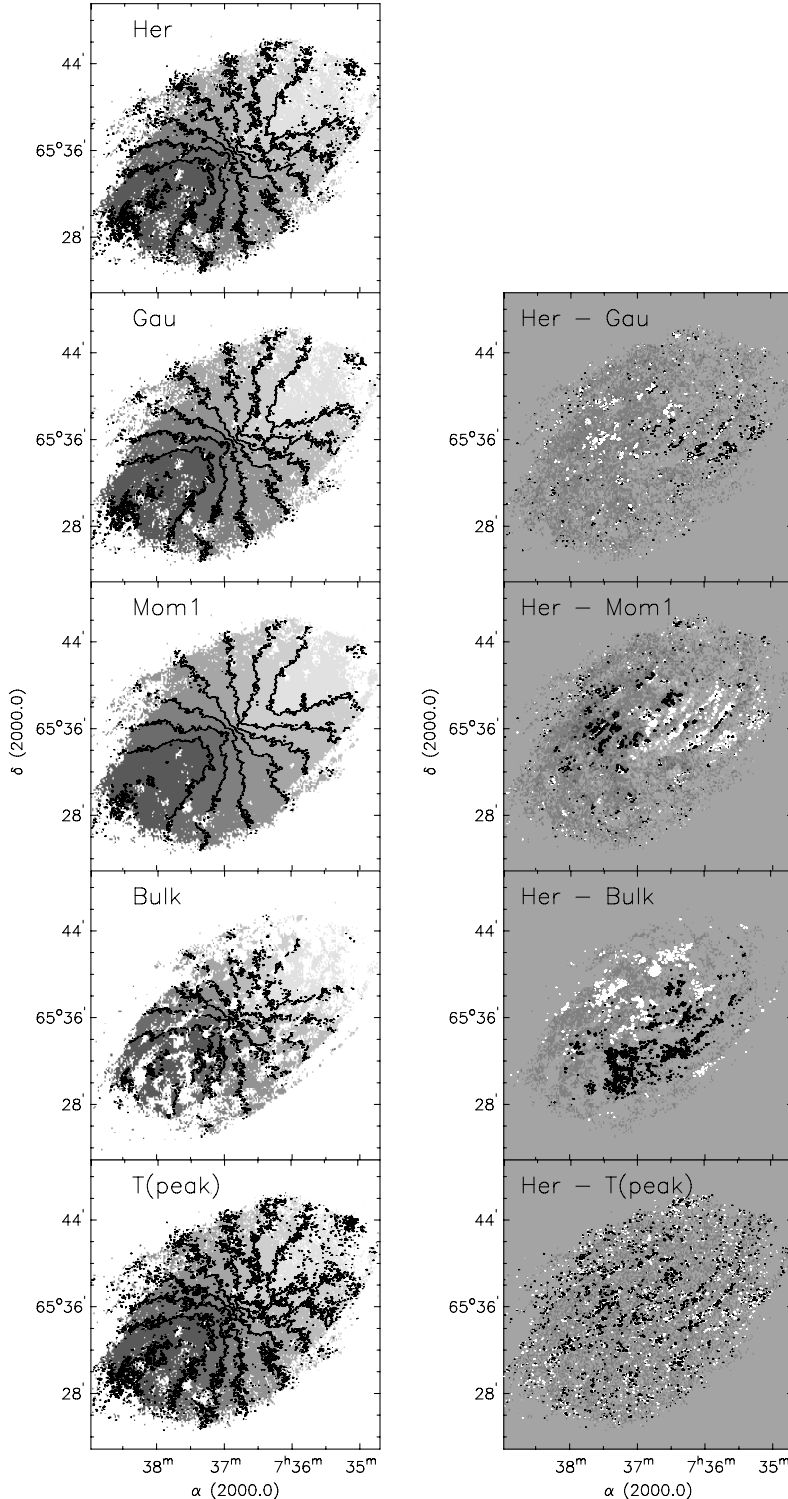


Figure 1. Different types of velocity fields derived for NGC 2403. In the left column are shown, from top to bottom, the Hermite velocity [Her], the single Gaussian [Gau], the intensity-weighted first-moment (Mom1), the bulk [Bulk] and the peak amplitude [T(peak)] velocity fields. The velocity contours run from 10 km s^{-1} (top-right; light gray scales) to 250 km s^{-1} (bottom-left; dark gray scales) in steps of 30 km s^{-1} . The minor axis contour is at 130 km s^{-1} . The right column shows the difference velocity fields with respect to the Hermite velocity field, as indicated in the figure. Gray scales run from -15 (black) to $+15$ (white) km s^{-1} , in steps of 5 km s^{-1} . The white contour shows the -10 km s^{-1} level, the black contour the $+10 \text{ km s}^{-1}$ level.

A first analysis of the velocity fields presented in Walter et al. (2008) showed that THINGS galaxies with indicative H I inclinations higher than 40° are all suitable for rotation curve

analysis. These galaxies are all discussed in the current paper. Galaxies with H I inclinations less than 30° are unsuitable and will not be discussed any further here. Of the galaxies with

Table 1
Indicative Global Inclinations of the THINGS Galaxies

Name	$i_{\text{H}\alpha}$ ($^{\circ}$)	i_{LEDA} ($^{\circ}$)	Name	$i_{\text{H}\alpha}$ ($^{\circ}$)	i_{LEDA} ($^{\circ}$)
NGC 628	15	21	NGC 4449	...	54
NGC 925	50	58	NGC 4736	44	29
NGC 1569	...	55	NGC 4826	64	58
NGC 2366	65	71	NGC 5055	51	53
NGC 2403	55	61	NGC 5194	30	32
NGC 2841	69	61	NGC 5236	31	21
NGC 2903	66	64	NGC 5457	30	12
NGC 2976	54	58	NGC 6946	35	17
NGC 3031	59	58	NGC 7331	77	67
NGC 3077	...	35	NGC 7793	43	56
NGC 3184	29	12	IC 2574	51	67
NGC 3198	72	74	DDO 53	33	46
NGC 3351	39	53	DDO 154	70	29
NGC 3521	69	58	Ho I	27	17
NGC 3621	62	66	Ho II	31	45
NGC 3627	61	63	M81 dwA	27	...
NGC 4214	38	39	M81 dwB	28	63

Note. Galaxies that have rotation curves presented in this paper are printed in bold. For some galaxies, a representative inclination could not be determined. All inclinations listed here are indicative and are not used in the dynamical analysis presented in this paper.

$\text{H}\alpha$ inclinations between 30° and 40° , only NGC 6946 proved suitable. The reason why a rotation curve can be derived for this galaxy, whereas this was not possible for, e.g., NGC 4214 (which has a comparable indicative $\text{H}\alpha$ inclination), is the large ratio of galaxy size to beam size. The resulting larger number of resolution elements in the NGC 6946 velocity field help constrain the kinematics better than for the other galaxies in that ($\text{H}\alpha$) inclination range.

A look at Table 1 shows that there are a few cases where the $\text{H}\alpha$ and optical inclinations differ substantially. These can, however, be readily explained. DDO 154 ($i_{\text{H}\alpha} > 40^{\circ}$, $i_{\text{LEDA}} < 40^{\circ}$) has a well-defined and regular $\text{H}\alpha$ disk, but a low surface brightness ill-defined optical component. The $\text{H}\alpha$ inclination is thus far more reliable. M81 dwB ($i_{\text{H}\alpha} < 40^{\circ}$, $i_{\text{LEDA}} > 40^{\circ}$) has a high-surface brightness central bar-like structure that affects the optically derived inclination. NGC 3351 ($i_{\text{H}\alpha} < 40^{\circ}$, $i_{\text{LEDA}} > 40^{\circ}$) has a fairly face-on and regular $\text{H}\alpha$ disk, but optically is dominated by a very strong central bar. NGC 4736 ($i_{\text{H}\alpha} > 40^{\circ}$, $i_{\text{LEDA}} < 40^{\circ}$) is the only galaxy where the outer $\text{H}\alpha$ disk seems to have a genuinely higher inclination than the central optical component.¹⁰

One might argue that our choice to consider only galaxies for which the geometrical parameters can be kinematically determined is needlessly strict, and that rotation curves could in principle be derived for the lower inclination galaxies by using additional information, such as the axis ratios of the optical or $\text{H}\alpha$ disks. However, in these cases, the best one can do is assume a *constant* inclination. This will then ignore intrinsic inclination changes (due to, e.g., the presence of warps), which can strongly affect the derived rotation velocities: an estimate that is only a few degrees off at these low inclinations readily leads to spurious rotation velocities. To illustrate this, at an inclination of $\sim 20^{\circ}$, a 5° uncertainty, equivalent to a 3% uncertainty in the axial ratio, leads to a 25% uncertainty in the deprojected rotation velocity. Furthermore, as discussed earlier, at low inclinations, random or

streaming motions can be as important as the *projected* rotation velocity and these will therefore severely affect the resulting rotation curve.

In the following, we will limit ourselves to the subsample of galaxies indicated in Table 1, i.e., all high-inclination THINGS galaxies ($i \gtrsim 40^{\circ}$) that are dominated by rotation, and, in addition, NGC 6946, leading to a total sample size of 19 galaxies. In our analysis we will use the natural-weighted THINGS data sets. The robust weighting does give a higher angular resolution, but at a decreased column density sensitivity. We found that the small loss in resolution due to the use of the natural-weighted data is more than compensated for by the increased column density sensitivity and, hence, increased usable area of the velocity fields.

We did apply neither residual-scaling corrections, nor primary beam corrections (as described in Walter et al. 2008). The reason for not using these corrections is that for the construction of our velocity fields (described in the next section), we need a constant noise level throughout each galaxy's data cube. Primary beam corrections introduce a noise and flux scaling dependent on the distance to the pointing center. Residual scaling, in essence, artificially decreases the noise in the data cubes in order to produce correct flux densities. All velocities mentioned in this paper are heliocentric using the optical velocity definition.

3. VELOCITY FIELDS AND ROTATION CURVES

3.1. Velocity Field Types

$\text{H}\alpha$ rotation curves are most often derived from velocity fields. A velocity field aims to give a compact and accurate “short-hand” description of the dynamics of a galaxy by assigning a “typical” velocity to every spatial position. That is, for every position, one uses the velocity that most accurately represents the circular motion of the bulk of the quiescent component of the gas as it moves around the center of the galaxy. In an ideal case (quiescent, purely rotating disk, infinite resolution, intermediate inclination) this velocity corresponds to the velocity associated with the peak emission in the velocity profile.

In practice, however, the observed velocity profiles are affected by several systematic effects. These can be divided into effects inherent to the observations themselves, and those due to physical processes within the galaxy.

The first category, instrumental and observational effects, is especially important in lower resolution observations. Here the effect of the relatively large beam (compared with the size of the galaxy) causes asymmetrical velocity profiles, with the long tail always pointing toward the systemic velocity. This is known as “beam smearing.” Generally, one attempts to correct for this by choosing a typical velocity close to the maximum velocity (i.e., furthest away from the systemic velocity) found in the velocity profile (e.g., Sancisi & Allen 1979). When left uncorrected, these resolution-related effects (including finite velocity resolution) always *lower* the apparent velocity.

The second category is due to physical processes within the galaxy that cause noncircular motions. These will show up as deviations both toward and away from the systemic velocity. For our galaxies, this is discussed extensively in accompanying papers by Oh et al. (2008) and Trachternach et al. (2008).

To minimize the impact these effects can have, different methods to construct velocity fields have been used in the past (discussed below). The THINGS observations have high enough spatial and velocity resolutions that the resolution effects are no longer a problem (see Section 3.4); they also give us a detailed

¹⁰ This is consistent with the results we will derive later in this paper. NGC 4736 shows a well-defined inclination trend, varying from $i \sim 30^{\circ}$ in the inner parts to $i \sim 50^{\circ}$ in the outer parts.

enough view of the small-scale movements of the H_I within the galaxies to enable us to quantify the noncircular motions. Nevertheless, each method determines the “typical” velocity in a slightly different way, and it is worth exploring these to quantify their impact on the final results.

In principle, our data are of high enough quality that (barring large noncircular motions) the velocity of the peak emission in a profile is representative of the total rotational motion. The most direct way to create a velocity field is therefore to simply determine the velocity at which this peak occurs. A. Usero et al. (2008, in preparation) derive these velocity fields in their study of the distribution of brightness temperatures within galaxy disks. For our purposes, these velocity fields are less suited, due to the decreased signal-to-noise (S/N) in the outer parts of the galaxies and their smaller usable areas. As mentioned, in the following we briefly discuss alternative methods most commonly used to construct velocity fields, list their pros and cons, and present our favored method.

A practical comparison of the outcomes of the various methods is shown in Figures 1–4 and discussed in more detail below as well as in Sections 3.2 and 3.3.

First-moment or intensity-weighted mean velocity. One of the most well-known and widely-used methods involves taking the first moment or intensity-weighted mean along the velocity axis in the data cube. The procedure is straightforward, but has the disadvantage that, if the velocity distributions are not symmetrical, the “typical” velocities are biased toward the longest tail of the velocity profile. Also, to avoid noise at outlying velocity values affecting the mean, one needs to carefully identify the regions with significant emission in the data cube and use only those areas when constructing the velocity field. This method is the one most commonly implemented in astronomical software.

Peak velocity fields. Using the velocity where the H_I profile flux peaks has the great advantage that it is totally independent from assumptions on profile shapes. A disadvantage is that as the profile peak value decreases, the velocity values become more and more affected by noise. The peak velocity field is therefore best used in regions of high S/N.

Gaussian profiles. An alternative is to fit single Gaussian functions to the velocity profiles. The velocity of the peak of the Gaussian profile is then taken to be the velocity field value. This method is less sensitive to noise and (moderate) asymmetries in the profiles than the first-moment method, but can still suffer from biased velocities if the asymmetries are strong or if multiple components are present. The single Gaussian fit method is best used in cases where the instrumental resolution is comparable to the typical width of the profiles. Many of the “classical” H_I rotation curve studies from the 1970s and 1980s fall in this category, and used this method to derive rotation curves.

Multiple Gaussian profiles. A logical extension is to fit multiple Gaussian functions to the velocity profiles. In many cases, however, the narrow width of the H_I profiles combined with limited velocity resolution yields only a relatively small number of independent profile data points with sufficiently high S/N. *Simultaneous* fits with two or more Gaussian functions can in these cases become sensitive to the choice of initial values, or have more free parameters than data points. A careful fine-tuning is in any case needed to provide optimum fits. An additional uncertainty is how to decide which of the components represents the true rotation velocity, and which one characterizes noncircular, random motions (induced by, e.g., star formation or

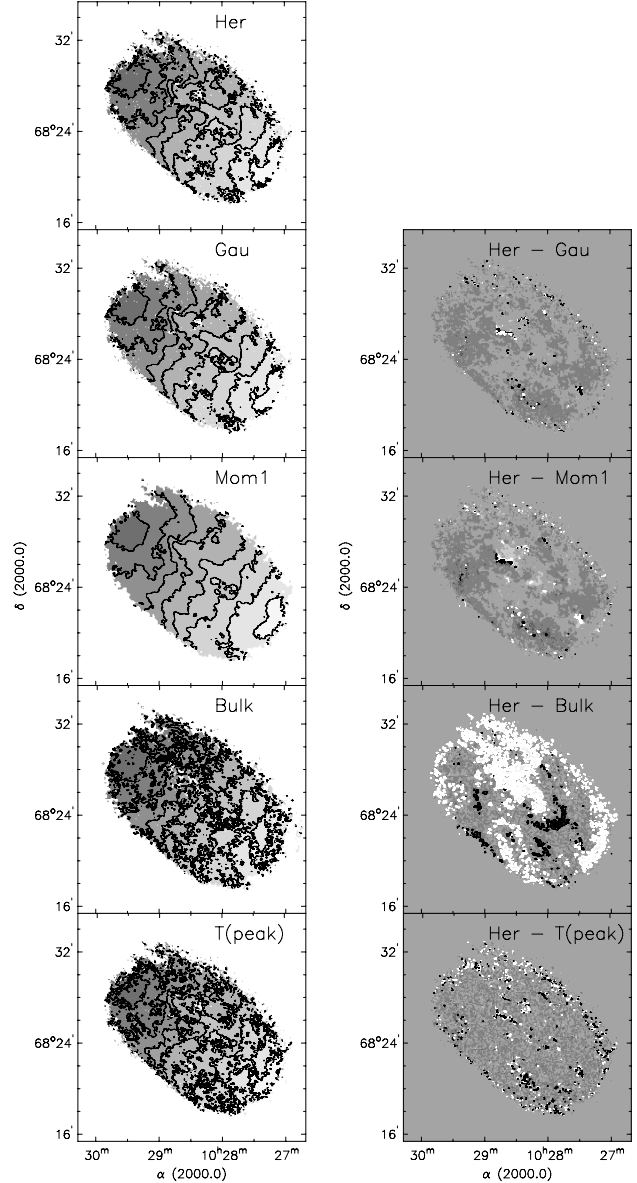


Figure 2. Different types of velocity fields derived for IC 2574. In the left column are shown, from top to bottom, the Hermite velocity (Her), the single Gaussian (Gau), the intensity-weighted first-moment (Mom1), the bulk (Bulk) and the peak amplitude [T(peak)] velocity fields. The velocity contours run from -5 km s^{-1} (bottom-right; light gray scales) to $+100 \text{ km s}^{-1}$ (top-left; dark gray scales) in steps of 15 km s^{-1} . The right column shows the difference velocity fields with respect to the Hermite velocity field, as indicated in the figure. Gray scales run from -15 (black) to $+15$ (white) km s^{-1} , in steps of 5 km s^{-1} . The white contour shows the -10 km s^{-1} level, the black contour the $+10 \text{ km s}^{-1}$ level.

spiral arms). As stated, these uncertainties apply to *simultaneous* fitting of multiple Gaussian functions. An alternative method is to optimally fit a single Gaussian function to the profile, subtract it, and subsequently make a second Gaussian fit to the residual profile. A robust application of this method is presented in Oh et al. (2008). This method is remarkably effective in separating random motions from the average rotation velocity (or “bulk” velocity, to use the terminology from Oh et al. 2008).

Hermite h_3 polynomials. A robust way to minimize the number of components is to include in the fitting function a

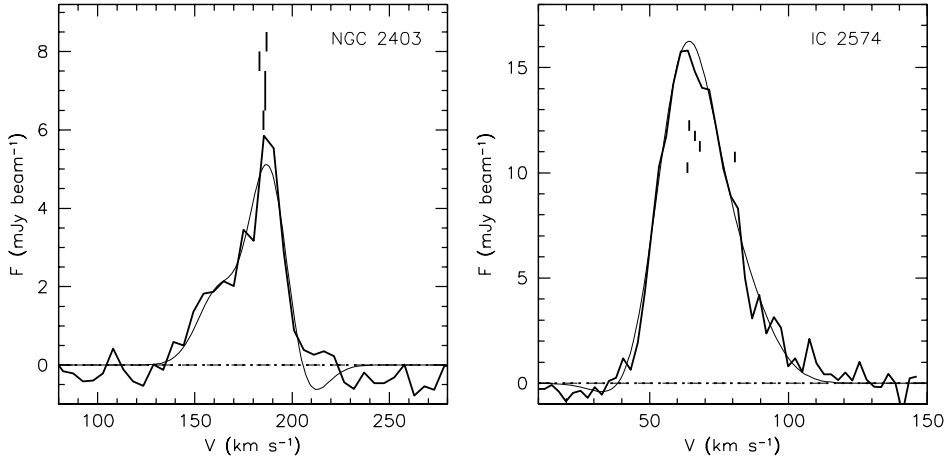


Figure 3. Left: observed profile of the H I emission in NGC 2403 at position $(\alpha, \delta)(2000.0) = 07^{\text{h}}37^{\text{m}}36\overset{\text{s}}{.}7, 65^{\circ}36'46\overset{\text{s}}{.}3$ (thick line). We adopt the notation given in Figure 1. The five vertical lines indicate the derived typical velocities using, from top to bottom, the Her ($V = 186.9 \text{ km s}^{-1}$), the Gau ($V = 183.2 \text{ km s}^{-1}$), the Mom1 ($V = 186.2 \text{ km s}^{-1}$), the Bulk ($V = 186.1 \text{ km s}^{-1}$) and the T(peak) velocity fields ($V = 185.4 \text{ km s}^{-1}$). The curve shows the Hermite fit. Right: observed profile of the H I emission in IC 2574 at position $(\alpha, \delta)(2000.0) = 10^{\text{h}}28^{\text{m}}51\overset{\text{s}}{.}4, 68^{\circ}28'13\overset{\text{s}}{.}0$ (thick line). The five vertical lines indicate the derived typical velocities using, from top to bottom, the Her ($V = 64.2 \text{ km s}^{-1}$), the Gau ($V = 66.3.2 \text{ km s}^{-1}$), the Mom1 ($V = 68.1.2 \text{ km s}^{-1}$), the Bulk ($V = 80.8 \text{ km s}^{-1}$), and the T(peak) velocity field ($V = 63.8 \text{ km s}^{-1}$).

prescription of the typical asymmetry encountered. A convenient function to use for this purpose is a *Gauss–Hermite polynomial* that includes an h_3 (skewness) term (see van der Marel & Franx 1993). The Hermite method has already been applied successfully to derive rotation curves of early-type galaxies in Noordermeer et al. (2007), and we will use it as our primary method to derive velocity fields. We do not include an additional h_4 term in the fit, which would provide a measure of the kurtosis of the profile (i.e., whether the profile is “fatter” or more “pinched” than a Gaussian function). Attempts to include an h_4 term show that, for the purposes of determining a velocity field, this leads to diminishing returns: the fits become less stable and need increasingly fine-tuned initial estimates. For high S/N profiles, the velocities derived using the Hermite profile will be close to those as derived from the peak-velocity fields. One could, therefore, argue that the latter are preferable, as they are model independent. However, in low S/N regions the Hermite velocity field results are more stable as more data points (from neighboring channels) are used to minimize the effects of the noise. We therefore prefer to use the Hermite velocity fields.

We illustrate the various methods for two representative galaxies. The first is NGC 2403 (Section 3.2, Figure 1), which is dominated by rotation, and where most of the asymmetrical profiles are associated with streaming motions along the spiral arms. The second example is the dwarf galaxy IC 2574 (Section 3.3, Figure 2) where a large fraction of the profiles is affected by asymmetries and random motions.

3.2. NGC 2403: A Galaxy Dominated by Regular Rotation

Figure 1 shows the velocity fields for NGC 2403, derived using the procedures described above, together with difference velocity fields with respect to the Hermite velocity field. The absolute differences between the Hermite velocity field and the Gaussian and first-moment velocity fields are larger than 10 km s^{-1} for only a small fraction of the area. For the peak velocity field, the difference with the Hermite field is consistent with pure noise (mostly caused by the lower S/N of the peak velocity field).

Figure 3 shows an example of an asymmetrical profile in NGC 2403, together with the values for the typical velocity,

again derived using the methods described above. Shown in Figure 4 are the rotation curves derived from the respective velocity fields, using otherwise identical assumptions and methods (see Section 3.5). Any difference is thus entirely due to the manner in which the velocity field was derived. The curve based on the Hermite velocity field systematically shows the highest rotation velocities and agrees best with the peak velocity field curve. The curves based on the Gaussian and first-moment fields are progressively more affected: the latter curve systematically underestimates the rotation velocity by $\sim 4 \text{ km s}^{-1}$ over the inner half of the disk. The bulk velocity field curve is also consistent with the Hermite field rotation curve, but with a larger scatter.

3.3. IC 2574: A Galaxy with Substantial Random Motions

A second example is IC 2574, where the velocity field is clearly affected by noncircular, random motions (compare with Walter & Brinks 1999). These are clearly visible as “kinks” in the iso-velocity contours in all of the Hermite, Gaussian, first-moment, and peak velocity fields shown in Figure 2. It is clear that before a rotation curve can be derived, some correction for the noncircular motions must first be made. This process is described in detail for IC 2574 in Oh et al. (2008). The effect of this correction is illustrated in Figure 3. The resulting “bulk” velocity field, showing the rotational part of the kinematics, is also shown in Figure 2. Though noisier than the other velocity fields, the kinks have largely disappeared, and the velocity field is consistent with simple solid-body rotation. The resulting bulk rotation curve also differs significantly from those derived from the uncorrected velocity field as shown in the bottom panel of Figure 4.

Further analysis shows that in our sample only NGC 2366 and IC 2574 are significantly affected by these random motions and they are therefore the only two galaxies where the bulk velocity field differs significantly from the Hermite velocity field (Oh et al. 2008). For these two galaxies, we will use the latter in the rest of this paper. For the other galaxies, the differences are negligible and we will use the Hermite velocity fields.

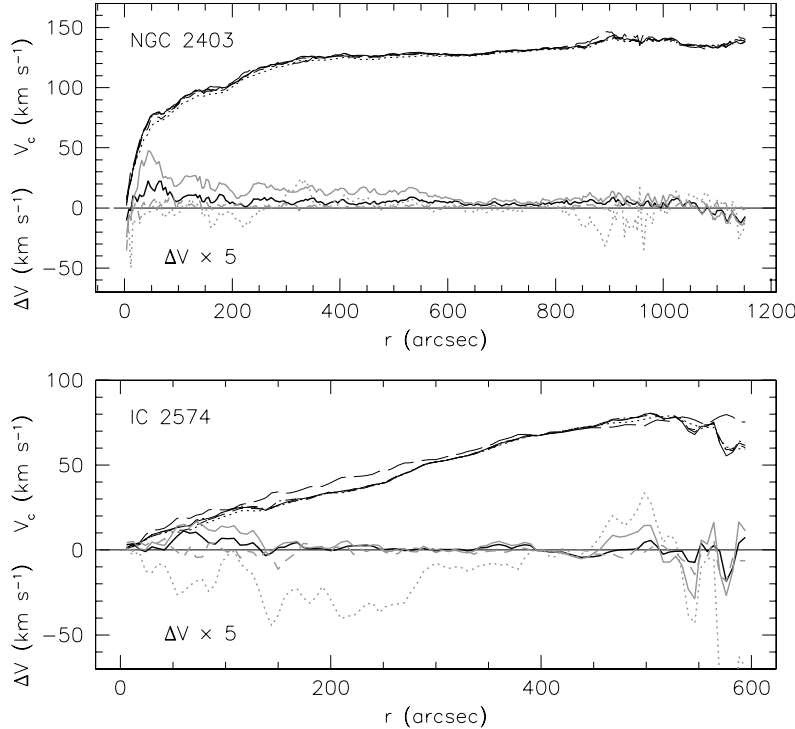


Figure 4. Rotation curves for NGC 2403 derived using the five different velocity fields. Dotted curve: Mom1; dashed curve: Gau; full curve: Her; long-dashed curve: Bulk; dot-short dash curve: T(peak). Also shown are the differences with respect to the Hermite curve. Thick black curve: Her–Gau; thick gray full curve: Her–Mom1; thick dotted gray curve: Her–Bulk; thick dashed gray curve: Her–T(peak). The differences have been multiplied by a factor of 5 for clarity. Bottom: rotation curves and differences for IC2574. Line types as described above.

3.4. Resolution Effects

The THINGS data are extremely well resolved. For example, the ratio of galaxy size to beam size for NGC 2403 is $\sim 350:1$. Nevertheless, some galaxies, including NGC 2403, show steep increases in velocity in their inner parts and despite the high resolution, these small radii could potentially still be affected by beam smearing. We quantify this effect by constructing two model data cubes using the Groningen Image Processing SYstem (GIPSY; van der Hulst et al. 1992) task GALMOD. This task takes an input rotation curve, radial H_I distribution, *i* and P.A., as well as H_I scale height and velocity dispersion, and creates a model data cube at arbitrarily high resolution by distributing a large number of H_I “clouds” through this data cube using the input parameters as probability distributions. This cube can then be “observed,” e.g., by smoothing it to a lower resolution, and be used to construct velocity fields, derive rotation curves, etc.

To make the model galaxies as realistic as possible, we adopt the H_I distribution and average *i* and P.A. of NGC 2403. We assume a velocity dispersion of 8 km s^{-1} , and a vertical (Gaussian) scale height of 100 pc. None of these assumptions critically affect the results. For the input rotation curves, we adopt two extreme versions of the observed NGC 2403 rotation curve. For the first model, we assume a steep linear rise to 130 km s^{-1} (the maximum rotation velocity of NGC 2403) within 1 kpc ($65''$), and a flat 130 km s^{-1} rotation curve outside 1 kpc. The second model is identical, except that it rises to its maximum rotation velocity within 0.5 kpc ($33''$); compare these with the observed rotation curve of NGC 2403 described in Section 4.3, and indicated in Figure 5.

The resulting model cubes were smoothed to a resolution of $8''$ (the natural-weighted beam size for the NGC 2403 observations; see Walter et al. 2008) and a channel spacing of 5.2 km s^{-1} was adopted. The resulting “observed” cubes were then used to construct Hermite velocity fields and rotation curves were derived (see Sections 3.5 and 3.6).

We compare the derived curves with the respective input models in Figure 5. Though we did calculate the cube for the entire radial extent of our pseudo-NGC 2403, we only show the inner portions of the rotation curves in Figure 5 to focus on the rising part of these curves. It is clear that beam smearing is not a serious problem, with most of the curves differing by less than 1 km s^{-1} from the input model. The only significant difference occurs around $R = 65''$ for the 1 kpc model and around $R = 33''$ for the 0.5 kpc model, but this is entirely due to the unrealistically sharp break in our input curves. The innermost point of both curves is also somewhat affected, but only at the level of $\sim 3 \text{ km s}^{-1}$ for the 1 kpc model and at $\sim 6 \text{ km s}^{-1}$ for the 0.5 kpc model. In summary, this demonstrates that resolution effects such as beam smearing have no significant effect on the THINGS data.

3.5. Deriving the Velocity Fields

As mentioned before, we use data sets without primary-beam and residual-scaling corrections as we need the original noise properties of the data to perform the profile fitting. For each galaxy, Hermite h_3 polynomials were fitted to all velocity profiles with the GIPSY task XGAUFIT.

To ensure high-quality velocity fields, we retain only profiles with fitted intensity maxima higher than $3\sigma_{\text{chan}}$ (where σ_{chan} is

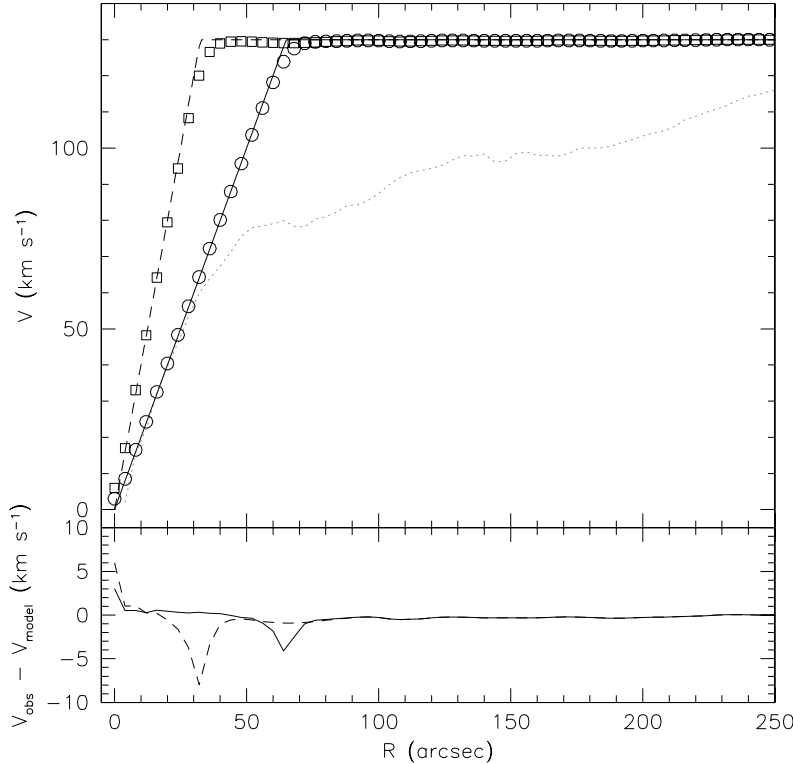


Figure 5. Top panel: comparison of input model rotation curves with “observed” curves as derived from model data cubes smoothed to the THINGS resolution. The full curve represents the input model rotation curve of a model that rises to its maximum rotation velocity within 1 kpc. The open circles represent the corresponding rotation curve as observed at the THINGS resolution. The dashed curve and open squares are the corresponding curves for a model rising to its maximum value within 0.5 kpc. The dotted curve represents the real rotation curve of NGC 2403. Bottom panel: difference between “observed” rotation velocity and input model velocity. The full line represents the 1 kpc model, the dashed curve the 0.5 kpc model.

the average noise in the line-free velocity channels in the relevant cube) and where the equivalent Gaussian dispersion of the fit is larger than the channel separation (see Walter et al. 2008 for the noise values and channel separations). To objectively remove a small number of noise pixels admitted by these filter criteria, we use the integrated H I column density map as an additional mask and retain the fits only at positions where the total flux value in the integrated H I map is higher than $3\sigma_N$, where σ_N is the noise in the integrated H I map. For independent channels (as is the case with the THINGS cubes), σ_N is defined as $\sigma_N = \sqrt{N}\sigma_{\text{chan}}$, where N is the number of channels with signal contributing to each pixel.¹¹ These various steps result in objectively defined Hermite velocity fields that form the basis of our analysis.

3.6. Deriving the Rotation Curves

The high spatial and velocity resolutions of the THINGS observations, as well as the favorable inclinations of the sample galaxies, make these objects ideal targets for a tilted-ring rotation curve analysis. In a standard tilted-ring analysis, a galaxy is described using a set of concentric rings, each with their own inclination i , P.A., systemic velocity V_{sys} , center position (x_0, y_0) , and rotation velocity V_C . Assuming that the gas moves in purely circular orbits, one can then describe the line-of-sight velocity for any position (x, y) on a ring with radius

R as

$$V(x, y) = V_{\text{sys}} + V_C(R) \sin(i) \cos(\theta). \quad (1)$$

In this equation, θ is the P.A. with respect to the receding major axis measured in the plane of the galaxy. This quantity is related to the P.A. in the plane of the sky by

$$\cos(\theta) = \frac{-(x - x_0) \sin(\text{P.A.}) + (y - y_0) \cos(\text{P.A.})}{R} \quad (2a)$$

$$\sin(\theta) = \frac{-(x - x_0) \cos(\text{P.A.}) - (y - y_0) \sin(\text{P.A.})}{R \cos(i)}. \quad (2b)$$

P.A. is defined as the angle measured counter-clockwise between the north direction on the sky and the major axis of the receding half of the galaxy. For each ring, the parameters are varied using a least-squares algorithm until an optimum fit with the velocity field is achieved.

We use the GIPSY task ROTCUR to make the tilted-ring fits and derive the rotation curves. As positions closer to the major axis carry more rotational information than positions near the minor axis, we use a $|\cos(\theta)|$ weighting for all fits. In defining the radii and widths of the rings, we sample the rotation curve at a rate of two points per synthesized beam width.

In this section we give a general description of the procedure we used. Detailed and more technical descriptions of the derivation of individual rotation curves are given in the Appendix. For each galaxy, first we fix the position of the dynamical center to that determined in the analysis of Trachternach et al. (2008) who used the same data. For completeness, the resulting coordinates of the dynamical centers are given in Table 2. After fixing the

¹¹ Note that in creating an integrated H I map one adds emission across a number of channels, rather than calculating the average. Provided the channels are independent, i.e., the noise is not correlated between channels, the noise thus increases as the square root of the number of channels added.

Table 2
Tilted-Ring Model Parameters of the THINGS Galaxies

Name (1)	α (2000.0) ($^{\text{h m s}}$) (2)	δ (2000.0) ($^{\circ} \text{' ''}$) (3)	D (Mpc) (4)	ΔR ($''$) (5)	V_{sys} (km s^{-1}) (6)	$\langle i \rangle$ ($^{\circ}$) (7)	$\langle \text{P.A.} \rangle$ ($^{\circ}$) (8)
NGC 925	02 27 16.5	+33 34 43.5	9.2	3.0	546.3	66.0	286.6
NGC 2366	07 28 53.4	+69 12 51.1	3.4	6.0	104.0	63.8	39.8
NGC 2403	07 36 51.1	+65 36 02.9	3.2	4.0	132.8	62.9	123.7
NGC 2841	09 22 02.6	+50 58 35.4	14.1	5.0	633.7	73.7	152.6
NGC 2903	09 32 10.1	+21 30 04.3	8.9	7.0	555.6	65.2	204.3
NGC 2976	09 47 15.3	+67 55 00.0	3.6	3.5	1.1	64.5	334.5
NGC 3031	09 55 33.1	+69 03 54.7	3.6	6.0	-39.8	59.0	330.2
NGC 3198	10 19 55.0	+45 32 58.9	13.8	6.0	660.7	71.5	215.0
IC 2574	10 28 27.7	+68 24 59.4	4.0	6.0	53.1	53.4	55.7
NGC 3521	11 05 48.6	-00 02 09.2	10.7	6.0	803.5	72.7	339.8
NGC 3621	11 18 16.5	-32 48 50.9	6.6	6.5	728.5	64.7	345.4
NGC 3627	11 20 15.0	+12 59 29.6	9.3	5.0	708.2	61.8	173.0
NGC 4736	12 50 53.0	+41 07 13.2	4.7	5.0	306.7	41.4	296.1
DDO 154	12 54 05.7	+27 09 09.9	4.3	6.5	375.9	66.0	229.7
NGC 4826	12 56 43.6	+21 41 00.3	7.5	5.0	407.4	65.2	120.9
NGC 5055	13 15 49.2	+42 01 45.3	10.1	5.0	496.8	59.0	101.8
NGC 6946	20 34 52.2	+60 09 14.4	5.9	3.0	43.7	32.6	242.7
NGC 7331	22 37 04.1	+34 24 56.5	14.7	3.0	818.3	75.8	167.7
NGC 7793	23 57 49.7	-32 35 27.9	3.9	6.0	226.2	49.6	290.1

Note. (1) Name of galaxy; (2) right ascension (J2000.0); (3) declination (J2000.0), center positions from Trachternach et al. (2008); (4) distance as given in Walter et al. (2008); (5) sampling increment used to derive the rotation curve; (6) adopted systemic velocity; (7) average value of the inclination; (8) average value of the P.A. of the receding side, measured from north to east, and in the plane of the sky.

center position, an additional ROTCUR run is used to determine V_{sys} (with P.A. and i still left as free parameters). In general, the systemic velocity has very little uncertainty associated with it. The adopted values are given in Table 2. After fixing the central position and systemic velocity, ROTCUR is run once more with P.A. and i as free parameters. The trends of i and (especially) P.A. with radius are generally well defined, varying smoothly with radius and exhibiting little scatter. Of the two fitting parameters, the P.A. is very stable, and any small perturbations in its value result in only second-order changes in the rotation curve. In some cases, small-scale fluctuations in the inclination are seen. These are mostly caused by effects such as streaming motions along spiral arms for which the fitting program tries to “compensate” by changing i .

To prevent these small spurious changes and to retrieve the underlying “bulk” rotation, we describe the P.A. and i distributions by slightly smoothed radial distributions that ignore these small-scale “wiggles.” A simple box-car smoothing with a kernel width of 3 or 5 data points was used in most cases. This affects only the point-to-point scatter of the i and P.A. values for the few galaxies where these wiggles are relevant, and does not affect the resolution of their radial distributions. With P.A. and i fixed using these radial distributions, we derive the final rotation curve. We also construct model velocity fields based on the tilted-ring models, as well as corresponding residual velocity fields containing the noncircular component.

The inclination wiggles described above, as caused by streaming motions, affect only a small part of the area of the velocity field for a small number of galaxies and do not affect the shape of the rotation curves in any critical way. Our treatment of the i and P.A. distributions assigns the dominant noncircular motions to the residual velocity field. An explicit comparison between the ROTCUR residual velocity fields and the results from a full rigorous treatment of the noncircular motions is made in

Trachternach et al. (2008), and shows that the above procedure is justified. Care was also taken to double-check that the solutions produced using our P.A. and i distributions were self-consistent (i.e., we checked whether running ROTCUR again with only P.A. and i free, and V_C fixed, yielded P.A. and i distributions consistent with our input values).

The method just described assumes galaxies are azimuthally symmetrical. However, asymmetries in the disk, or lopsidedness, can introduce intrinsic differences. To quantify the uncertainties introduced by this, we derive separate fits to the rotation curves of the approaching and receding sides of the galaxies.

A final issue is the definition of the final uncertainties in the rotation curves. Unfortunately, there is no consensus in the literature on how to quantify these. Sometimes the formal 1σ χ^2 -fit uncertainty in V_C is used. However, by their nature, these uncertainties are much smaller than the dispersion of individual velocity values found along a tilted ring. This dispersion is, therefore, also commonly used as an alternative definition, as it is more representative of the physical uncertainties than the formal fit error. For the NGC 3198 rotation curve (discussed in Section 4.8), for example, the average 1σ χ^2 fit error is ~ 17 times smaller than the average dispersion along the rings. Using only formal χ^2 -based error bars thus severely underestimates the true “physical” uncertainty.

An additional source of uncertainty is formed by possible differences in rotation velocity between the approaching and receding sides. Swaters (1999) assumes that the differences between the rotation curves derived for the entire disk and those for either the approaching or receding side represent a 2σ difference, and defines a pseudo- 1σ uncertainty due to asymmetries, as one fourth of the difference between the approaching and receding side velocities. Though this is only an assumption, we follow this convention and define the uncertainties in the rotation curves as the quadratic addition of the dispersions

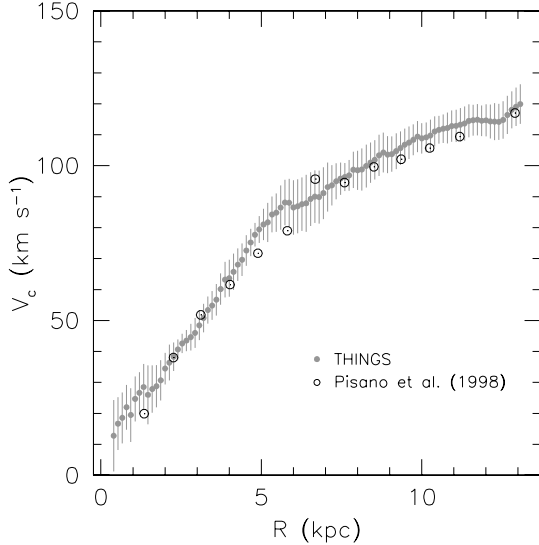


Figure 6. Comparison of the NGC 925 THINGS rotation curve with the curve derived in Pisano et al. (1998). Symbols as indicated in the figure. The uncertainties given in Pisano et al. (1998) are smaller than the symbol sizes. However, their uncertainties are the formal least-square fit errors and severely underestimate the true uncertainties in the measured rotation velocity (see discussion in Section 3.5).

found along the rings and the pseudo- 1σ uncertainties due to asymmetries between approaching and receding sides. Note that this is a very conservative definition: the difference in velocity between approaching and receding sides will already be partly reflected in the dispersion found along a ring. The uncertainties in the rotation velocities presented here thus give a realistic, and possibly even conservative, picture of the error budget of our rotation curve determinations.

4. INDIVIDUAL GALAXIES

Detailed descriptions of the data as well as the derivation of the tilted ring models and the resulting rotation curves of individual galaxies are given in the Appendix. In this section, we compare these results with previous determinations of the various H I rotation curves from the literature. (For NGC 3621 and NGC 3627 we could find no previous, published determinations of their H I rotation curves. These are therefore not discussed in this Section and we refer to the Appendix for more information.) We do not compare with H α or CO rotation curves. These are determined using different methods, and originate from different phases of the interstellar medium (ISM); systematic effects due to these differences are not straightforward to quantify and beyond the scope of the current paper.

For reference, a summary of the resulting tilted-ring parameters is given in Table 2. These include the position of the dynamical center, the rotation curve sampling interval, systemic velocity and radially averaged values of P.A. and i . For the central positions we use the results presented in Trachternach et al. (2008) as derived using the same data. We adopt luminosities and distances as given in Walter et al. (2008), and where necessary literature measurements have been corrected to the same distance scale.

4.1. NGC 925

NGC 925 is classified as a late-type barred spiral. It was previously observed in H I by Pisano et al. (1998). Figure 6

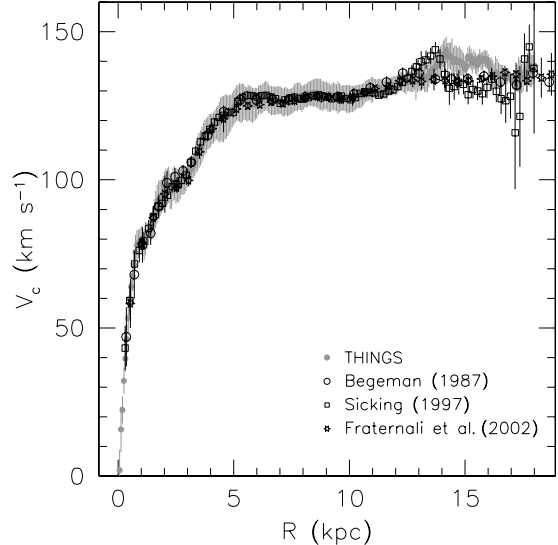


Figure 7. Comparison of the NGC 2403 THINGS rotation curve with recent determinations from the literature. Symbols and references are indicated in the figure.

compares the rotation curves. The main difference with our analysis, namely the position of the dynamical center, is discussed in Trachternach et al. (2008). This difference also explains the slightly higher value for V_{sys} of 551.5 km s $^{-1}$ found by Pisano et al. (1998), compared with our 546.3 km s $^{-1}$. Other than this, we derive broadly similar trends of i and P.A. with radius. The curves themselves agree within the uncertainties, showing that for solid-body (inner) rotation curves, such as this one, the shape does not critically depend on the position of the center. The uncertainties quoted in Pisano et al. (1998) are the formal fit errors. As discussed before, these are unrealistically small, representing the error in the mean velocity along a ring, rather than the scatter. In this case these formal errors are smaller than the sizes of the symbols in Figure 6. The uncertainties we have adopted are more representative of the true physical uncertainties.

4.2. NGC 2366

The data and analysis of NGC 2366 are given in Oh et al. (2008). We refer to their paper for a complete discussion.

4.3. NGC 2403

NGC 2403 is a late-type Sc spiral and member of the M81 group. Its H I rotation curve has been derived in many previous studies. The first measurement using a synthesis telescope was presented in Shostak (1973). NGC 2403 has since been re-observed and re-analyzed at ever-increasing sensitivity and resolution by, among others, Bosma (1978), Begeman (1987), Sicking (1997), and Fraternali et al. (2002). In Figure 7 we compare our curve with some of these analyses, all corrected to the same distance. There is generally good agreement between the various determinations. Beyond ~ 13 kpc the curves differ somewhat, but most of the velocity information at these radii originates from close to the minor axis of the velocity field, and thus depends on details such as the weighting used in the tilted ring fit and the flux limit used to mask the velocity field.

Other parameters also compare favorably: the average i and P.A. values found by Begeman (1987) were 60 $^{\circ}2$ and 122 $^{\circ}5$, respectively. Sicking (1997) found 60 $^{\circ}9$ and 123 $^{\circ}9$,

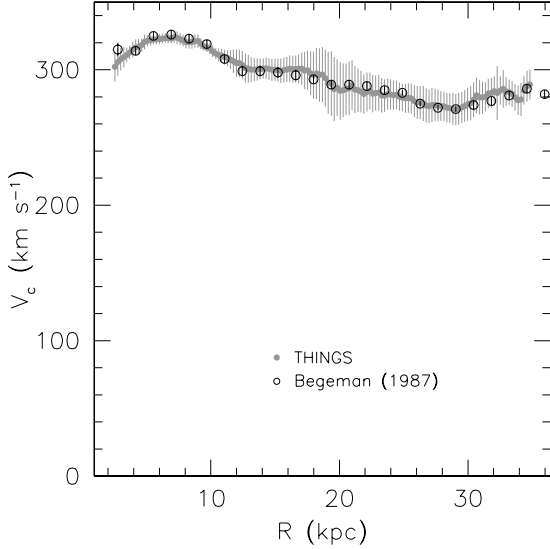


Figure 8. Comparison of the NGC 2841 THINGS rotation curve with the analysis by Begeman (1987). Symbols and references are indicated in the figure. Note the different nature of the uncertainties: the Begeman (1987) result uses the formal errors in the least-squares fit, whereas our definition takes into account the differences between the two sides of the galaxy, and the dispersion in velocity values found along the rings.

whereas Fraternali et al. (2002) derived 62°.9 and 124°.5. Our average values (defined as the average unweighted values of the model distributions) agree well, at 62°.9 and 123°.7, respectively. Similarly, the average absolute difference between our V_{sys} value and the three literature values is only 0.5 km s $^{-1}$.

The “bump” at $R \simeq 15$ kpc in the THINGS curve is real, in the sense that it cannot be explained by an incorrectly chosen i or P.A. Most of the information in this part of the curve originates from the two arms that are seen to stretch away in the outermost northern and southern parts of the H α map. Motions along these arms could explain the feature, as suggested by the kinks in the velocity contours at those radii. The velocity fields of NGC 2403 are also discussed in Section 3.2.

4.4. NGC 2841

NGC 2841 is an early-type (Sb) spiral and was previously observed at lower resolution in H α by Begeman (1987). We compare the curves in Figure 8 and find good correspondence overall. Begeman (1987) finds a systemic velocity of 631.1 ± 1.4 km s $^{-1}$, a difference of only 2.6 km s $^{-1}$ with our value of 633.7 ± 1.8 km s $^{-1}$. The average P.A. and i values found by Begeman (1987) are 154°.5 and 73°.1, respectively, and differ from our values by only a few degrees (see Table 2).

4.5. NGC 2903

NGC 2903 was previously observed in H α by Begeman (1987). Figure 9 compares the two rotation curves. The Begeman (1987) value of $V_{\text{sys}} = 557.3 \pm 1.3$ km s $^{-1}$ agrees well with our value of 555.6 ± 1.3 km s $^{-1}$. The outer declining parts of the rotation curves also agree well with each other. There are, however, significant differences in the inner, rising parts of the rotation curve, where the curve by Begeman (1987) rises much more steeply. His data did not allow a full tilted-ring model in the inner part of the galaxy, and the sudden changes in P.A. and i are therefore also not detected in his analysis. Rather, the innermost data points of the Begeman (1987) curve were derived from a

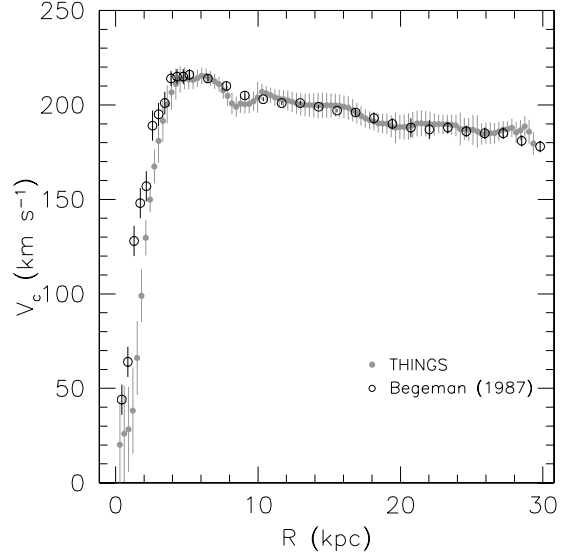


Figure 9. Comparison of the NGC 2903 THINGS rotation curve with the analysis by Begeman (1987). Symbols and references are indicated in the figure. See Figure 8 for a description of the uncertainties.

major axis position–velocity diagram. The higher spatial and velocity resolution of our data and the different methods used to extract the velocities both contribute to this large difference.

4.6. NGC 2976

NGC 2976 is classified as an Sc galaxy and was previously observed in H α by Stil & Israel (2002). They chose the center of mass of the H α disk as their dynamical center, and there is an offset of $\sim 10''$ with respect to our choice. Their choice for V_{sys} is also slightly different from ours: 4 ± 2 km s $^{-1}$ versus our 1.1 ± 1.3 km s $^{-1}$. Stil & Israel (2002) find $i = 65^\circ$ and P.A. = 326° versus our values of 64°.5 and 334°.5, respectively. Figure 10 compares the two curves. The Stil & Israel (2002) curve suggests a flattening toward the outer radii, whereas our curve keeps rising until the last measured point. The curves do, however, agree within their respective uncertainties.

4.7. NGC 3031

Better known as M81, this galaxy is the prototypical grand-design spiral and together with M82 and NGC 3077 forms an interacting system, (e.g., van der Hulst 1997; Yun et al. 1994). A previous determination of the H α rotation curve was by Visser (1978, 1980). We compare our results in Figure 11 after correction to the same distance scale. We find excellent agreement overall between his and our rotation curves where they overlap in radius. The differences we find are all attributable to different local values for P.A. and i : we allow i and P.A. to change with radius, whereas Visser (1980) uses a constant inclination of 59° and a P.A. value of 329°. However, these constant values agree, well with our average values of 59° and 330°.2, respectively.

4.8. NGC 3198

NGC 3198 is known for its prototypical flat rotation curve (see van Albada et al. 1985). We compare our rotation curve with those derived by Begeman (1987, 1989) and Sicking (1997) in Figure 12. The systemic velocities agree within their respective

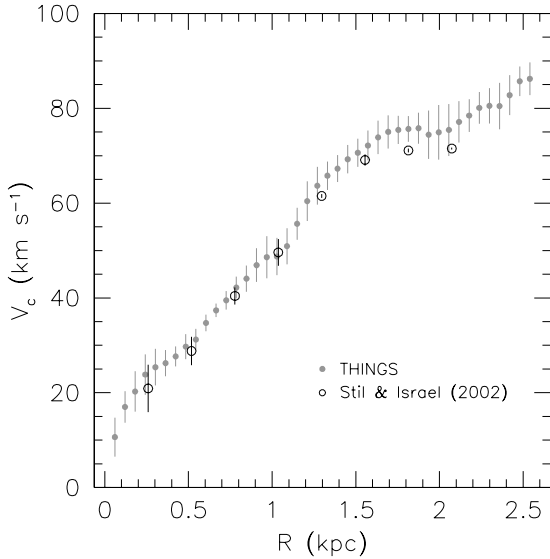


Figure 10. Comparison of the NGC 2976 THINGS rotation curve with the analysis by Stil & Israel (2002). Symbols and references are indicated in the figure. Note the different nature of the uncertainties: Stil & Israel (2002) use the difference between the approaching and receding sides as a measure for the uncertainty, whereas our definition additionally takes into account the dispersion in velocity values found along the rings.

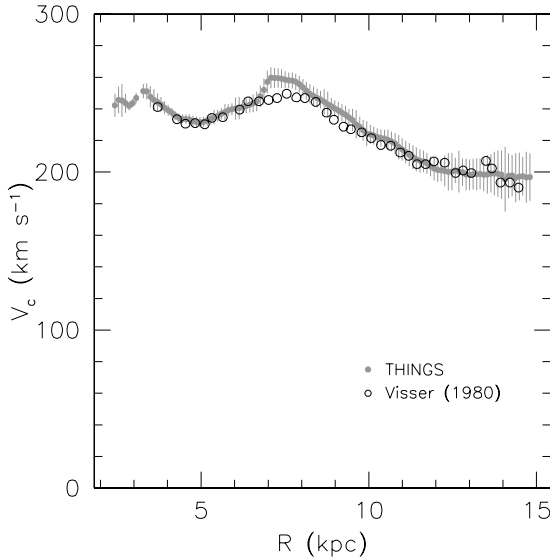


Figure 11. Comparison of the NGC 3031 THINGS rotation curve with the analysis by Visser (1980). Symbols and references are indicated in the figure. Note that no uncertainties are given in Visser (1980).

1σ uncertainties: our result is 660.7 ± 2.6 km s $^{-1}$, Begeman (1989) finds 660.4 ± 0.8 km s $^{-1}$, whereas Sicking (1997) finds 659.4 ± 2.6 km s $^{-1}$. The respective average P.A. and i values only show differences $\lesssim 1^\circ$.

Turning now to the rotation curves themselves and starting with the outer parts, we find that our curve agrees well with the Sicking (1997) result, but is a few km s $^{-1}$ higher than the Begeman (1989) data. Noting that the uncertainties in neither the Sicking nor the Begeman analysis take into account the difference between approaching and receding sides, the results are still consistent with each other.

In the inner parts, the Begeman (1989) data show consistently higher rotation velocities. These were, however, derived from

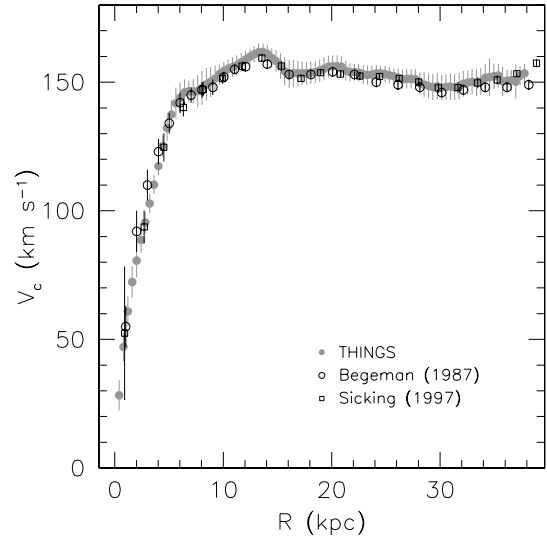


Figure 12. Comparison of the NGC 3198 THINGS rotation curve with recent determinations from the literature. All curves have been corrected to a distance of 13.80 Mpc. Symbols and references are indicated in the figure.

major-axis position velocity diagrams, rather than from a tilted-ring model. Due to the much lower resolution they were also explicitly corrected for beam smearing. The systematic offset could therefore imply an overcorrection of the Begeman (1989) data, or a systematic deviation due to the use of major axis profile velocities. Begeman (1987) mentions that the beam smearing corrections are only significant within $1'5$ (~ 6 kpc), precisely the radius within which the curves show disagreement. The inner parts of our curve are fully consistent with the Sicking (1997) rotation curve.

4.9. IC 2574

The data and analysis of IC 2574 are described by Oh et al. (2008) and we refer to their paper for a more complete discussion. The velocity fields of IC 2574 have also been discussed in Section 3.3.

4.10. NGC 3521

NGC 3521 was previously observed in H α by Casertano & van Gorkom (1991). Its rotation curve was presented as one of the first cases where a genuinely declining H α rotation curve was found in a spiral galaxy. We compare our curve with the Casertano & van Gorkom (1991) curve in Figure 13. The agreement is not perfect; the literature curve underestimates the rotation velocity in the inner parts whereas our curve does not show the steep drop in the outer parts. Unfortunately, Casertano & van Gorkom (1991) do not list the values they assume for i and P.A., which precludes a more detailed comparison. The high inclinations and resulting insensitivity of the rotation velocities to the exact inclination values, make it unlikely that the difference is a pure inclination issue. For example, a change in i of 5° , starting from an initial value of $i = 75^\circ$, only amounts to a change of some 2% or ~ 4 km s $^{-1}$, not the ~ 30 km s $^{-1}$ that is needed to bring the Casertano & van Gorkom (1991) in agreement with ours. In summary, even though we find rotation velocities in the outer parts that are lower than in the inner parts, we do not find evidence for the steep drop, nor for the negative gradient in outer velocities as presented in Casertano & van Gorkom (1991).

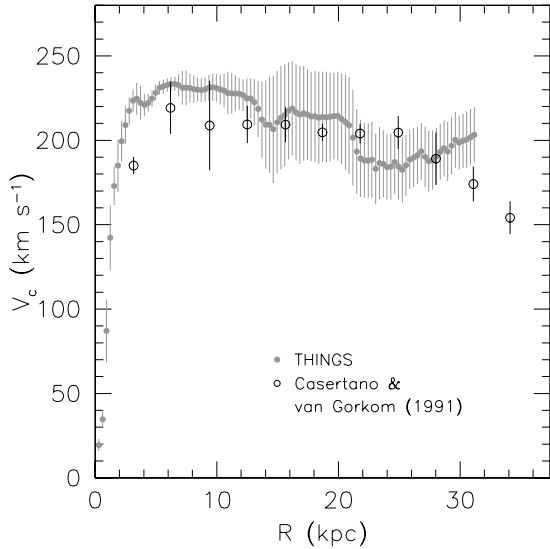


Figure 13. Comparison of the NGC 3521 THINGS rotation curve with the analysis by Casertano & van Gorkom (1991). Symbols and references are indicated in the figure.

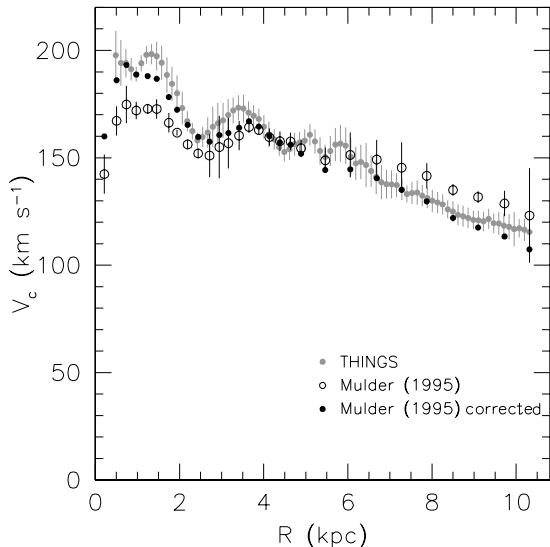


Figure 14. Comparison of the NGC 4736 THINGS rotation curve (gray points) with the analysis by Mulder (1995). The open circles show the rotation curve as published in Mulder (1995) assuming a constant inclination of 40°. The filled black circles show the same data but corrected using our inclinations.

4.11. NGC 4736

NGC 4736 was previously observed in H I by Mulder (1995) who also derived a rotation curve. Figure 14 shows a comparison between the respective rotation curves. Due to the lower resolution and sensitivity of his data, Mulder (1995) did not detect a trend of inclination with radius, and therefore assumed a constant value of 40°. In Figure 14 we therefore also show his rotation curve corrected using our inclination values. Although the large-scale trends are similar to those found for our curve, the THINGS curve, in general, shows more pronounced small-scale features.

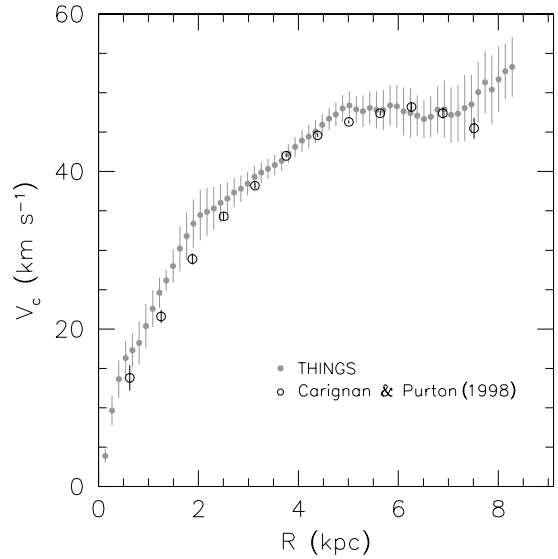


Figure 15. Comparison of the DDO 154 THINGS rotation curve with the curve derived in Carignan & Purton (1998). Symbols and references are indicated in the figure.

4.12. DDO 154

DDO 154 is a gas-rich dwarf galaxy whose rotation curve has been extensively studied (see Carignan & Freeman 1988; Carignan & Purton 1998). It was also one of the first galaxies whose rotation curve was used to illustrate the conflict with CDM predictions (Moore 1994). DDO 154 shows clear evidence of a warp in the outer parts. There is no evidence for large noncircular motions in the velocity field (Trachternach et al. 2008). This is evidenced by the residual velocity field where the absolute value of the residuals nowhere exceeds ~ 6 km s $^{-1}$.

Previous determinations of the rotation curve of DDO 154 (cf., Carignan & Freeman 1988; Carignan & Purton 1998) show an apparent drop in the rotation velocity in the outermost parts, which was interpreted as evidence that at these radii one has almost reached the edge of the dark matter halo. In Figure 15 we compare our rotation curve with one of these determinations. Contrary to the Carignan & Purton (1998) and Carignan & Freeman (1988) results, we do not find strong evidence for a decline and our rotation curve in the outer parts is consistent with being flat.

Given the differences found in the tilted ring parameters of the approaching and receding sides separately, the error bars belonging to the Carignan & Purton (1998) rotation curve most likely underestimate the true uncertainties. Also note that our rotation curve, in general, shows higher rotation velocities than the Carignan & Purton (1998) one. This is not merely an inclination effect, as our values for i are, in general, higher by a few degrees than those presented in Carignan & Purton (1998). Correcting the curves to the same inclinations would therefore only increase the difference. Note that a model with a decreasing inclination in the outer parts, as perhaps suggested by our analysis (see the Appendix), would lead to an *increasing* rotation velocity in the outer parts. The only way in which our determination of the rotation curve could be made consistent with a *declining* rotation curve is to increase the inclination, which is ruled out by our data.

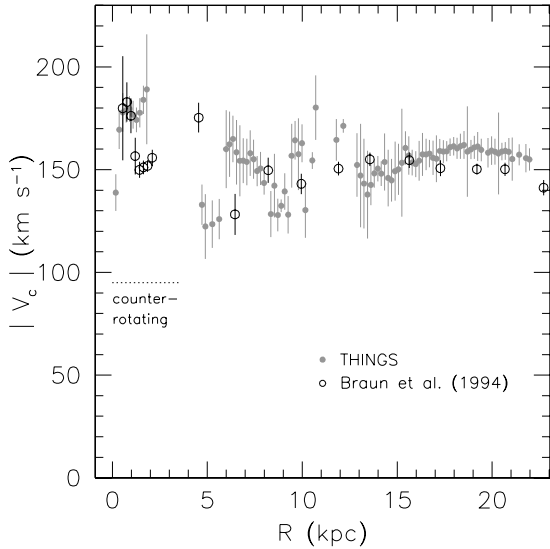


Figure 16. Comparison of the NGC 4826 THINGS rotation curve with the analysis by Braun et al. (1994). Symbols as indicated in the figure. Plotted are the *absolute* rotation velocities, the inner disk ($R < 4$ kpc; indicated by the horizontal dotted line) rotates in the opposite direction compared to the outer disk.

4.13. NGC 4826

NGC 4826, or the “Evil-Eye” galaxy, is an early-type spiral with the presence of two counter-rotating gas disks as its most remarkable kinematic feature (Braun et al. 1994). The inner high-column density H I disk is associated with the bright stellar disk and rotates in the same direction. The outer, much lower column-density H I disk rotates in the direction opposite to that of the stars. The transition between the two disks occurs around $\sim 100''$ radius. Braun et al. (1994) speculate that the outer disk might find its origin in a merger of a gas-poor spiral with a gas-rich and star-poor dwarf with a retrograde spin (with the mass ratio of the dwarf and the spiral $\lesssim 0.1$; Rix et al. 1995).

In Figure 16 we compare our rotation curve with that of Braun et al. (1994). Even though to first order there is reasonable agreement, the scatter in the velocities is much larger than in any of the other rotation curves presented here. Braun et al. remark that between $100'' \lesssim R \lesssim 300''$ (4 kpc $\lesssim R \lesssim 12$ kpc) the kinematic parameters are difficult to determine due to what they call a “severe distortion” in the velocity field, showing that the transition region between the two counter-rotating disks deviates from circular motions. Similar conclusions were reached for the ionized gas by Rix et al. (1995).

4.14. NGC 5055

NGC 5055 is an Sbc galaxy with an extended and warped tenuous outer H I disk. Its H I distribution and kinematics were recently analyzed by Battaglia et al. (2006). For V_{sys} , Battaglia et al. (2006) find a value of 497.6 ± 4.8 km s $^{-1}$, which is in close agreement with our value of 496.8 ± 0.7 km s $^{-1}$. Their distributions of i and P.A. are also in agreement, and they note a similar difference between the models for approaching and receding sides.

We compare the two rotation curves in Figure 17. The first inner maximum at $R \sim 2$ kpc is more pronounced in our data set. This is likely due to a combination of increased resolution and the use of Hermite polynomials as opposed to the Gaussian functions that Battaglia et al. (2006) used. This is also the most

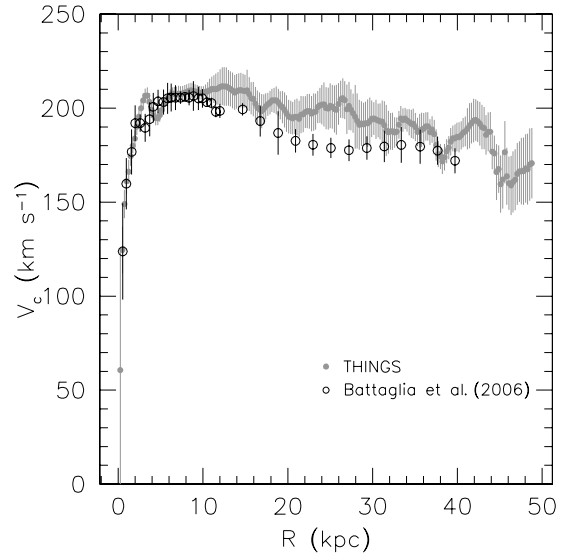


Figure 17. Comparison of the NGC 5055 THINGS rotation curve with the analysis by Battaglia et al. (2006). Symbols and references are indicated in the figure.

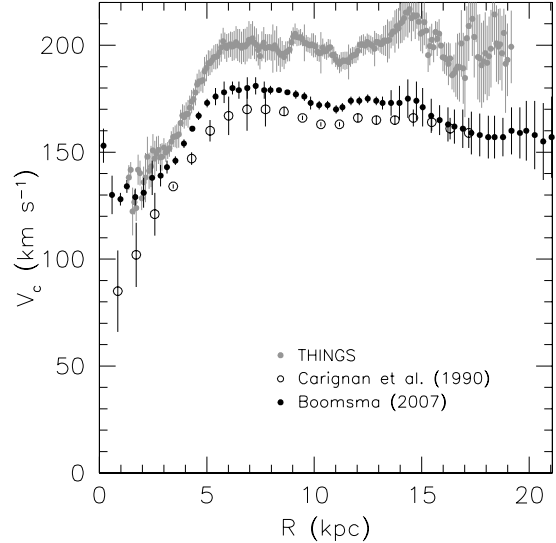


Figure 18. Comparison of the NGC 6946 THINGS rotation curve with the analyses by Carignan et al. (1990) and Boomsma (2007). Symbols and references are indicated in the figure.

likely explanation for the higher rotation velocities we find in the outer parts.

4.15. NGC 6946

NGC 6946 is a late-type spiral which, in terms of H I studies, is better known for its population of H I structures such as H I holes and high-velocity gas (e.g., Kamphuis & Sancisi 1993; Boomsma 2007). Its global dynamics have been relatively little studied. This can be partly attributed to its fairly low inclination which is at the limit of what is feasible using tilted-ring studies.

The rotation curve of NGC 6946 was determined before by Carignan et al. (1990) and more recently by Boomsma (2007). A comparison with our curve is made in Figure 18. Both Carignan et al. (1990) and Boomsma (2007) used a constant value of $i = 38^\circ$ in their analyses and these different inclinations, compared with our average value of 32.6° , explain the

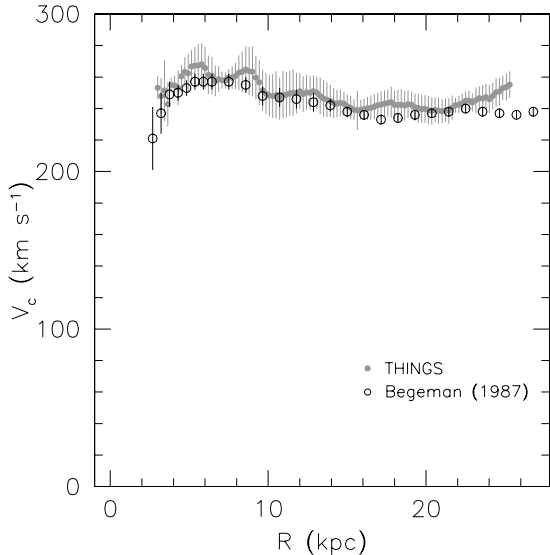


Figure 19. Comparison of the NGC 7331 THINGS rotation curve with the result by Begeman (1987). Symbols and references as indicated in the figure. Note the different nature of the uncertainties: the Begeman (1987) result uses the formal errors in the least-squares fit, whereas our definition takes into account the differences between the two sides of the galaxy, and the dispersion in velocity values found along the rings.

offset between the curves. Apart from this, the only prominent difference is the large rotation velocity Boomsma (2007) finds for the innermost point of the rotation curve. In our data the corresponding area of the velocity field is below our 3σ H α column density level, and we can therefore not comment on the presence of this feature in our data, though there is a hint of a turn-up in the major axis position–velocity diagram (see the description of NGC 6946 in the Appendix).

4.16. NGC 7331

NGC 7331 is an early-type Sb spiral with prominent spiral arms. It was previously observed in H α by Begeman (1987). Figure 19 compares both curves. It is clear that the two curves broadly agree, but there are many small differences. Most of them can be attributed to the very different spatial and velocity resolutions and different choices for the inclination distribution (see discussion in the Appendix). Note that the inner eight points of the Begeman (1987) curve are based on position–velocity diagrams and not on a tilted-ring fit to a velocity field. The differences in the outermost parts are due to the different inclinations used there.

4.17. NGC 7793

NGC 7793 is a late-type Sd spiral galaxy in the Sculptor group and was observed before in H α by Carignan & Puche (1990). In Figure 20 we compare our rotation curve with their results. The dynamical center and systemic velocity, as well as P.A., as found by Carignan & Puche (1990) agree with ours within the uncertainties. The behavior of the inclination is subtly different: whereas the Carignan & Puche (1990) analysis indicates a rising inclination in the outer parts, we find a (better defined) gradual decrease there. The resulting rotation curves on the whole agree reasonably well with each other, but differ in small but important respects. The most important one is the more gradual decline of our rotation curve in the outer parts. Even though Carignan &

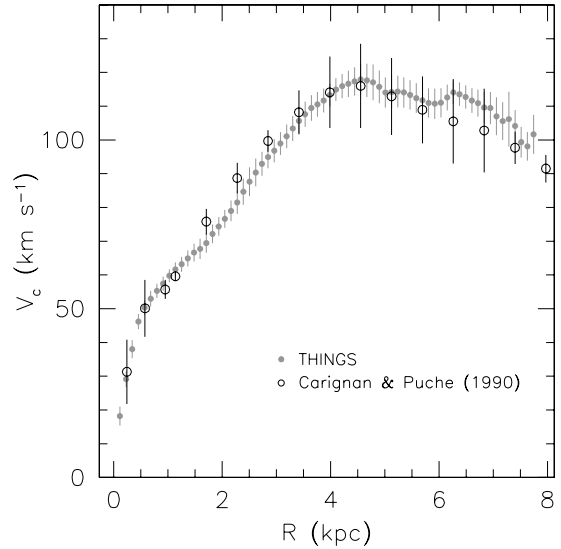


Figure 20. Comparison of the NGC 7793 THINGS rotation curve with the curve derived in Carignan & Puche (1990). Symbols and references are indicated in the figure.

Puche (1990) note that this is “one of the very few cases with a *truly declining* rotation curve” (their emphasis), we argue that any drop in rotation velocity is much less extreme, especially as there is some evidence that the inclination might decrease more strongly in the outer parts than we have assumed (see the description of NGC 7793 in the Appendix). Adopting this steeper drop would raise the rotation velocities we find in the outer parts by ~ 25 km s $^{-1}$. We stress that these inclination values are uncertain, and determined by only a small number of pixels, but they seem to suggest that a declining rotation curve cannot be unambiguously established.

4.18. Summary

In summary, we find, in general, good agreement with previous determinations of the rotation curves of the galaxies in our sample. The most notable differences are listed below.

1. We find some differences with previous determinations of the inner rotation curves of NGC 2903 and NGC 3198. Both galaxies contain a small central bar. The presence of this feature combined with the lower resolution of the literature data can contribute to this difference.
2. The outer rotation curve of NGC 5055 is higher than previously determined. Most likely, our use of a Hermite velocity field contributes to this difference.
3. We do not find steep declines in velocity in the outer rotation curves of NGC 3521, NGC 7793, DDO 154, and NGC 2366 (see Oh et al. 2008 for the latter curve). Where declines are observed, they are gentler, and (within the uncertainties in rotation velocity and inclination) consistent with flat rotation curves.

5. MASS MODELS

We now use the THINGS rotation curves, in combination with information on the distribution of gas and stars, to construct mass models of our sample galaxies. These models are then used to quantify the distribution of dark matter within the galaxies. We

calculate our best model estimate for the observed velocity as

$$V_{\text{obs}}^2 = V_{\text{gas}}^2 + \Upsilon_* V_*^2 + V_{\text{halo}}^2. \quad (3)$$

The mass models thus need the following as input: the observed rotation curve, V_{obs} , the rotation curve of the gas component, V_{gas} , and the rotation curve of the stellar component, V_* . The rotation curve from the halo, V_{halo} , can then be calculated from these known input curves. An additional free parameter is the stellar mass-to-light ratio, Υ_* , which is introduced as we generally can only measure the distribution of the *light* of the stellar population, rather than the required *mass*. This parameter introduces one of the largest uncertainties in the procedure and will be discussed in detail in Section 5.2.

While the *concept* of mass modeling is well described by Equation (3), there are some intricacies that warrant a brief discussion. The rotation velocities under consideration are in all cases the velocities of respective test particles moving in circular orbits in the plane of the galaxy. The rotation velocities of the gas, V_{gas} , and the stars, V_* , are defined as the velocities that each of the components would induce on a test particle in the plane of the galaxy if these disks were sitting in isolation without any external influences. These velocities in the plane are calculated from the observed baryonic mass density distributions, taking into account the (assumed) vertical density distribution. For the gas disk, one generally assumes a thin disk, while for the stellar disk, a thick, sech^2 distribution is chosen. These procedures and choices of parameters are described in more detail in Section 5.1 for the rotation curve of the gas and in Section 5.2 for the rotation curve of the stars. The latter section also describes in detail possible choices for Υ_* .

The halo velocities, V_{halo} , in Equation (3) (or rather the velocities induced on a test particle by the halo potential) are also measured in the plane of the galaxy and assume a spherical halo. Section 5.3 briefly discusses the dark matter models used, and in Section 5.4 the procedure of constructing the models is presented. Specific discussions dealing with individual galaxies are given in Section 6.

Initial analysis of the rotation curves of NGC 3627 and NGC 4826 showed their dynamics to be severely affected by noncircular motions (Trachternach et al. 2008) and we will therefore not consider these two galaxies further.

5.1. Neutral Gas Distribution

To derive the rotation curve associated with the neutral gas component, we use the primary beam and residual-scaled integrated H α maps from Walter et al. (2008). We derive neutral hydrogen surface density profiles using our previously derived tilted ring geometric parameters. The surface densities are corrected by a factor of 1.4 to take into account the presence of helium and metals (associated with the atomic hydrogen; the helium component by itself scales with a factor of 1.33). The ROTMOD task in GIPSY is then used to compute the corresponding rotation curve, under the assumption of an infinitely thin gas disk.

As we are dealing with a mass distribution in the form of a *disk*, rather than a sphere, the rules that generally apply to the gravitational force of a spherical mass distribution do not apply here. Most importantly, the convenient result that the mass distribution *outside* a particular radius does not affect the effective force inside that radius is not universally valid for a disk. Specifically, in the case of a disk with a sufficiently prominent central depression in the mass distribution, a test

particle located in or near it can feel a net *outward* force. A literal interpretation in the context of normal gravity would imply negative mass, an imaginary rotation velocity and therefore a negative value of V^2 . Here, following the convention in rotation curve literature, we plot the imaginary rotation velocities as negative velocities, keeping in mind that, in actuality, it is V^2 that is negative. We stress that this convention for representing the imaginary velocities is merely adopted for convenience and does not imply counter rotation or the presence of repulsive matter or other exotic phenomena; it is simply a short-hand to enable illustrating the effective force on a test particle caused by a nonspherical mass distribution with a central minimum. The mass model of NGC 3031 in Section 6.6 is a good example of this phenomenon.

5.2. Stellar Distribution

One of the main uncertainties in deriving mass models is the conversion from observed stellar luminosity to stellar mass (through the stellar mass-to-light ratio Υ_*). In the optical bands, Υ_* is dominated by the young stellar population, recent star formation events and the effects of dust and/or metallicity. Values of Υ_* derived in, e.g., the B band thus inherently have a large uncertainty that can be up to a factor of a few. These limitations are the reason why extreme mass-models involving so-called “maximum disks” or “minimum disks” (van Albada & Sancisi 1986) are often used. The maximum disk assumption maximizes the contribution of the baryonic matter by assuming the maximum value of Υ_* allowed by the total rotation curve. Minimum disk is the opposite and minimizes the baryonic contribution by setting $\Upsilon_* = 0$. Sometimes the contribution of the gas is also ignored (and all rotation is therefore assumed to be induced by the dark matter halo). These two extreme Υ_* assumptions can thus be regarded as “minimum halo” and “maximum halo” models, respectively, minimizing or maximizing the contribution of the dark matter. Though not necessarily physically plausible, they do provide hard upper and lower limits on the concentration and distribution of the dark matter.

Fortunately, the uncertainties in Υ_* decrease dramatically toward the near-infrared (NIR; from a factor ~ 10 in the B band to a factor ~ 3 in K ; see Bell & de Jong 2001). At NIR wavelengths one mostly probes the old stellar population containing the bulk of the stellar mass, as described in Bell & de Jong (2001) and Verheijen (1997). The range in plausible values for Υ_* is in the NIR only a shallow function of the color of the disk, and observations at these wavelengths are therefore useful in constraining the mass of the disk. Verheijen (1997) finds that maximum disk fits to a sample of HSB galaxies in the UMa cluster require only a small range of $\Upsilon_*^{K'} = 0.7 \pm 0.2$. Similarly, Bell & de Jong (2001) find, from population synthesis modeling, that disks of galaxies exhibit a typical range of $\Upsilon_*^K = 0.5 \pm 0.2$ measured over the full range of observed galaxy colors.

To characterize the stellar distributions in our sample galaxies, we use the 3.6 μm images from SINGS (Kennicutt et al. 2003; for NGC 2366, NGC 2903 and DDO 154, which are not part of the SINGS sample, we have retrieved data from the *Spitzer* archive.) These provide a good proxy for the emission of the (old) stellar disk (see Pahre et al. 2004). Note that some of the 3.6 μm emission may originate in asymptotic giant branch (AGB) stars, polycyclic aromatic hydrocarbons (PAHs), and hot young stars, but as we will only be using the radial distributions of the emission, their contribution (if present) will be strongly diminished by the azimuthal averaging.

After the images were cleaned of foreground stars, the tilted ring parameters were used to derive the radial luminosity profiles. We used the standard photometric calibration provided with the SINGS images to construct the surface brightness profiles. In most cases, the $3.6 \mu\text{m}$ surface brightness distributions can be well described by a single exponential disk. In a small number of galaxies, an additional central component was seen, containing only a small fraction of the total luminosity of the galaxy. It is a matter of debate whether it is appropriate to call this central component a “bulge.” The surface brightness distributions measured are not as steep as the canonical $R^{1/4}$ bulge surface distribution, which may reflect the THINGS sample selection criteria, with its emphasis on more late-type galaxies. Beyond this, the radial range over which this inner profile dominates the total emission is not large enough to accurately determine the value of n in an $R^{1/n}$ parameterization of the surface brightness profile of that central component. This is, however, not a major problem due to its rapid drop in surface brightness and we found that most often an exponential surface brightness distribution provides an adequate and convenient fit. We experimented with a number of different functional power-law forms, but found that this did not affect the shape of the (compact) rotation curve of this component to any relevant degree, and does not impact on our final mass models. Where necessary, we therefore decomposed the surface brightness profile in inner and outer exponential components. In the rest of this analysis, we refer to the outer component as the “outer disk,” or simply “disk.” The inner component we interchangeably call “inner disk” or “bulge.” This simply is a short-hand to indicate the components, and, especially for the inner component, should not be taken as a statement on its implied evolution or other physical properties. Central surface brightness values and scale lengths, where mentioned in the text, are not corrected for inclination. Needless to say that this correction *has* been applied prior to calculation of the rotation curve.

As far as we are aware, no exhaustive investigation has yet been made into the relation between $3.6 \mu\text{m}$ emission and Υ_* . We therefore use an empirical approach based on results derived using the Two Micron All Sky Survey (2MASS) J , H , and K bands to derive Υ_* in the $3.6 \mu\text{m}$ band (hereafter $\Upsilon_*^{3.6}$) from the *Spitzer* observations. All of our sample galaxies are included in the 2MASS Large Galaxy Atlas (Jarrett et al. 2003), and we use the $J - K$ colors given there, together with the relations between color and Υ_* given in Bell & de Jong (2001), as well as the relation between Υ_*^K and $\Upsilon_*^{3.6}$ from Oh et al. (2008), to derive the relation between $\Upsilon_*^{3.6}$ and $J - K$. We find

$$\log(\Upsilon_*^K) = 1.43(J - K) - 1.38 \quad (4)$$

and

$$\Upsilon_*^{3.6} = 0.92 \Upsilon_*^K - 0.05. \quad (5)$$

One of the largest uncertainties in determining Υ_* is the stellar initial mass function (IMF). Some aspects of this, within the context of THINGS, are discussed in Leroy et al. (2008); see also Bell & de Jong (2001) and Bell et al. (2003) for a more general discussion. Using stellar population synthesis models, Bell & de Jong (2001) show that a Salpeter (1955) IMF results in stellar disk masses that are too heavy to be consistent with dynamical (maximum disk) constraints from rotation curves. By scaling the stellar disk masses down by a factor of 0.7 in order to make them consistent with the rotation curves they introduce a “diet” Salpeter IMF, equivalent to a standard Salpeter IMF,

but with a reduced number of stars below $0.35 M_\odot$. This diet Salpeter is thus the maximum IMF (i.e., yielding the highest disk masses for a given photometric constraint) allowed by galaxy dynamics studies. Studies of the stellar population in the Milky Way suggest an IMF that produces lower disk masses (Kroupa 2001). The diet Salpeter disk masses are 0.15 dex (a factor 1.4) more massive than the Kroupa ones. We refer to Leroy et al. (2008) and Bell et al. (2003) for a discussion on other IMF indicators.

The disk masses as implied by Equation (4) assume the diet Salpeter IMF, and are therefore the maximum disk masses allowed for a given $J - K$ color. To gauge the effects of a “lighter” IMF on our rotation curve results we also derive disk masses assuming a Kroupa IMF by decreasing the constant term in Equation (4) by 0.15 dex.

Disk galaxies typically show radial color gradients of a few tenths of a magnitude, becoming bluer with radius. This is interpreted as a combined stellar age and metallicity gradient, with the outer regions younger and of lower metallicity; dust seems to play only a minor role in this regard (de Jong 1996). In the optical, these gradients are thought to imply radial Υ_* differences of a factor of ~ 2 between inner and outer parts of galaxies. Even in the K band where many of the effects of recent star formation and dust are minimized, changes in Υ_* of ~ 20 to $\sim 30\%$ are not uncommon. We therefore associate the ($J - K$) color gradients observed in the disks of our sample galaxies with variations in Υ_* . Oh et al. (2008) show that similar gradients in $\Upsilon_*^{3.6}$ are expected in the $3.6 \mu\text{m}$ band.¹² We refer to de Jong (1996) for an extensive discussion of color gradients in the optical and NIR. Our goal is to create mass models taking into account radial Υ_* variations within the stellar disk. We determine “ $\Upsilon_*^{3.6}$ -weighted” mass-surface density profiles for our galaxies and use these as input for ROTMOD to compute the rotation curve of the stellar disk. For these stellar disks we assume a vertical sech^2 distribution and use $z_0 = h/5$ where h is the exponential radial scale length (van der Kruit & Searle 1981a, 1981b).¹³ The rotation curve derived in this way does not critically depend on the value of h/z_0 .

One component we have not explicitly addressed is the molecular gas. However, as the molecular gas is (at least in non-dwarf THINGS disk galaxies) distributed like the stars (Leroy et al. 2008), and with a surface density only a few percent of that of the stars (Leroy et al. 2008), its (small) contribution is reflected in a small increase in Υ_* .

In an accompanying paper, Leroy et al. (2008) present an alternative empirical method to derive Υ_* values from the $3.6 \mu\text{m}$ images. They use the $3.6 \mu\text{m}$ and 2MASS K -band images themselves to directly derive an empirical pixel-to-pixel relation between the two bands, enabling them to predict K -band fluxes from the Infrared Array Camera (IRAC) images. Combining these K -band predictions with a constant $\Upsilon_*^K = 0.5$ then yields the stellar masses. We compare this with our results (discussed in Section 6) in Figure 21 for both our assumptions for the IMF. The masses we derive tend to be slightly larger; a least-squares fit yields a slope of 0.94 with a scatter of 0.12 dex. Given the empirical nature of both methods and the absence of

¹² Note that, as mentioned before, a small amount of dust emission due to, e.g., PAHs may be present; this emission will, however, be localized and have a small surface covering factor. The azimuthal averaging used will also tend to minimize its contribution.

¹³ This canonical ratio of $h/z_0 = 5$ has also been confirmed by Kregel et al. (2002), who for a sample of 34 edge-on galaxies find a value of $h/z_0 = 4.8 \pm 1.3$. This is consistent with $h/z_0 = 5$ which we will continue to use.

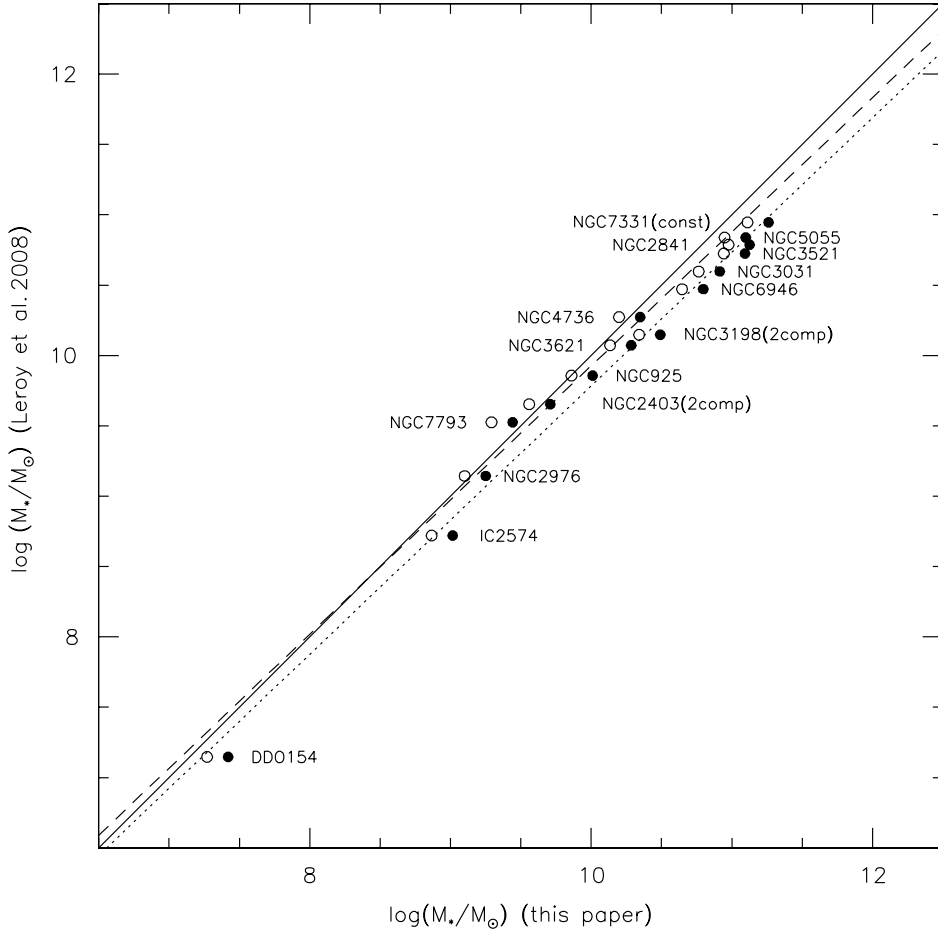


Figure 21. Comparison between the stellar disk masses derived using our method (horizontal axis) and the method described in Leroy et al. (2008; vertical axis). The filled circles indicate our dust Salpeter IMF masses and the open circles indicate the Kroupa IMF masses. The drawn line is the line of equality and the dotted line is a least-squares fit to the diet Salpeter IMF masses with a slope of 0.94 and an offset of 0.44. The scatter is 0.12 dex. The dashed line shows the fit to the Kroupa IMF masses with a slope of 0.95, an offset of 0.39, and a scatter of 0.13 dex.

a full set of rigorously computed population synthesis models, this should be regarded as a satisfactory agreement.

5.3. Dark Matter Halos

Here we describe the two well-known models for the dark matter distribution that we will use in our analysis. The first model is the Navarro-Frenk-White (NFW) halo (Navarro et al. 1996, 1997), which was derived from CDM simulations and is dominated by a central-density cusp. Second, we discuss the venerable, observationally motivated pseudo-isothermal (ISO) halo, dominated by a central constant-density core.

5.3.1. NFW Halo

The NFW mass density distribution takes the form

$$\rho_{\text{NFW}}(R) = \frac{\rho_i}{(R/R_s)(1+R/R_s)^2} \quad (6)$$

where R_s is the characteristic radius of the halo and ρ_i is related to the density of the universe at the time of collapse of the dark matter halo. This mass distribution gives rise to a halo rotation

curve

$$V(R) = V_{200} \left[\frac{\ln(1+cx) - cx/(1+cx)}{x[\ln(1+c) - c/(1+c)]} \right]^{1/2}, \quad (7)$$

where $x = R/R_{200}$. It is characterized by a concentration parameter $c = R_{200}/R_s$ and a velocity V_{200} . These are directly related to R_s and ρ_i and used to parameterize the rotation curve. The radius R_{200} is the radius where the density contrast with respect to the critical density of the universe exceeds 200, roughly the virial radius (Navarro et al. 1996). The characteristic velocity V_{200} is the velocity at this radius.

We can describe the steepness of the inner slope of the mass density profile with a power law $\rho \sim r^\alpha$. The NFW models then imply a value of $\alpha = -1$, the so-called “cusp.” Note that many different parameterizations of CDM halos exist in the literature (e.g., Navarro et al. 1996, 1997; Moore et al. 1999b; Navarro et al. 2004; Diemand et al. 2005). These all agree on the presence of a density cusp, but the steepness of the inner density profile depends slightly on the simulation used, with many models producing slopes that are steeper than the original NFW $\alpha = -1$ value. From an observational point of view, however, these models all give similar results, and we therefore use the conservative (in terms of inner slope) NFW parameterization.

The NFW c and V_{200} parameters are not independent and are set by the cosmology. McGaugh et al. (2007) presents the relation between c and V_{200} for two recent and representative Λ CDM models. The first one is the “vanilla CDM” model from Tegmark et al. (2004); the second one is based on WMAP results (Spergel et al. 2007). Both models predict a nearly flat distribution of c as a function of V_{200} . Simulations suggest a scatter in $\log(c)$ of ~ 0.18 (Bullock et al. 2001). The main difference between the two models is a different normalization, resulting in lower concentration values for the Spergel et al. (2007) model. If we consider the union of both models and take their respective 1σ scatters into account, we expect to find values $c \simeq 8^{+5}_{-3}$ for $V_{200} = 50 \text{ km s}^{-1}$, to values $c \simeq 6^{+4}_{-2}$ for $V_{200} = 200 \text{ km s}^{-1}$. Since we are considering the union of two models with different normalizations, this represents a generous allowable range of c values, comparable to a 2σ scatter for any of the two models separately. Anticipating our results, we note that the c parameter indicates the amount of collapse a halo has undergone. Larger values of c indicate a larger collapse factor. A value $c = 1$ indicates no collapse; a value $c < 1$ makes no sense within the CDM context, and we will refer to these as unphysical values in subsequent modeling.

5.3.2. ISO Halo

The spherical pseudo-ISO halo has a density profile

$$\rho_{\text{ISO}}(R) = \rho_0 \left[1 + \left(\frac{R}{R_C} \right)^2 \right]^{-1}, \quad (8)$$

where ρ_0 is the central density of the halo, and R_C is the core radius of the halo. The corresponding dark matter rotation curve is given by

$$V(R) = \sqrt{4\pi G \rho_0 R_C^2 \left[1 - \frac{R_C}{R} \arctan\left(\frac{R}{R_C}\right) \right]}. \quad (9)$$

The asymptotic velocity of the halo, V_∞ , is given by

$$V_\infty = \sqrt{4\pi G \rho_0 R_C^2}. \quad (10)$$

As the inner mass-density distribution is dominated by an (almost) constant-density core, it can be approximated by a power-law description $\rho \sim r^\alpha$ with $\alpha = 0$.

5.4. Constructing the Mass Models

We use the observed rotation curve, the derived gas rotation curve and the rotation curve(s) of the stellar component(s) as input for the mass modeling with the GIPSY task ROTMAS. This task subtracts the (squared) rotation curves of the baryonic components (after appropriate scaling with $\Upsilon_*^{3.6}$) from the (squared) observed rotation curve, and fits the desired dark matter halo model to the residuals. We use inverse-squared weighting of the rotation curve uncertainties in making the fits. For each combination of galaxy and dark matter halo model we derive two sets of fits. Firstly, we fix the $\Upsilon_*^{3.6}$ values of the stellar components to the values predicted by our empirical color- $\Upsilon_*^{3.6}$ relations for both the diet Salpeter and the Kroupa IMFs and determine the best-fitting NFW and ISO halo parameters. We will refer to these fits as the “fixed $\Upsilon_*^{3.6}$ ” models. Secondly, we derive a set of fits where $\Upsilon_*^{3.6}$ is left as a free parameter. That is, we ignore any prior knowledge derived from population synthesis models, and let the fitting program choose its best value. These will be referred to as the “free $\Upsilon_*^{3.6}$ ” models.

6. RESULTS FOR INDIVIDUAL GALAXIES

Below we describe the mass models for each galaxy along with a motivation for specific choices made for individual galaxies. The results for IC 2574 and NGC 2366 are described in Oh et al. (2008). The $\Upsilon_*^{3.6}$ values and halo model parameters (including those for IC 2574 and NGC 2366) are given in Table 3 for the fixed $\Upsilon_*^{3.6}$ models with a diet Salpeter IMF, in Table 4 for a fixed $\Upsilon_*^{3.6}$ with a Kroupa IMF, in Table 5 for the free $\Upsilon_*^{3.6}$ ISO models, and in Table 6 for the free $\Upsilon_*^{3.6}$ NFW models. The free $\Upsilon_*^{3.6}$ models do not depend on the IMF. The $3.6 \mu\text{m}$ surface brightness and $\Upsilon_*^{3.6}$ profiles, as well as the fixed and free $\Upsilon_*^{3.6}$ models assuming NFW and ISO models are shown in Figures 22–56. The relations of $\Upsilon_*^{3.6}$ with $(J - K)$ shown in these Figures are valid for a diet Salpeter IMF. Values for $\Upsilon_*^{3.6}$ assuming a Kroupa IMF can be obtained by shifting the relations down by 0.15 dex. In the interests of space, we show only the diet Salpeter mass models, as they are generally similar to those derived assuming a Kroupa IMF. Noteworthy exceptions are discussed below in the sections for individual galaxies. Readers more interested in the outcomes for the sample as a whole can at this point skip to Section 7. In the following discussion all $\Upsilon_*^{3.6}$ values assume a diet Salpeter IMF unless noted otherwise.

6.1. NGC 925

The surface brightness profiles of NGC 925 are shown in Figure 22. The 2MASS J , H , and K profiles can be traced out to $\sim 250''$; the $3.6 \mu\text{m}$ profile can be traced over the entire extent of the H α disk. NGC 925 shows no evidence for a bright central component. There is also no evidence for a strong color gradient, and we assume a constant $\Upsilon_*^{3.6} = 0.65$ for the disk.

The rotation curves are shown in Figure 23. The predicted $\Upsilon_*^{3.6}$ value make NGC 925 slightly exceed maximum disk. The ISO model can to some degree accommodate this, but the NFW model can do so to a lesser extent. This does not change when adopting the Kroupa $\Upsilon_*^{3.6}$ values. Fits with $\Upsilon_*^{3.6}$ free prefer lower values for $\Upsilon_*^{3.6}$. For the NFW case a negative $\Upsilon_*^{3.6}$ is preferred; we have assumed a fixed $\Upsilon_*^{3.6} = 0$ in this case. For both fixed and free $\Upsilon_*^{3.6}$ the NFW model yields parameters that are inconsistent with the CDM expectations (see Section 5.3.1), resulting in V_{200} values many times larger than the maximum rotation of the galaxy and c values approaching zero. This is a general symptom of an NFW halo trying to fit a linearly rising rotation curve (McGaugh & de Blok 1998). The ISO models in general fit the data better than the NFW models.

6.2. NGC 2403

Figure 24 shows the surface brightness profiles derived from the $3.6 \mu\text{m}$ data, as well as the 2MASS J , H , and K profiles. The $3.6 \mu\text{m}$ profile can be reliably traced to $\sim 430''$ galactocentric radius, and the 2MASS profiles out to $\sim 380''$. The $(J - K)$ color shows a clear trend, from ~ 0.9 in the inner parts to ~ 0.6 at the outermost measured radii. This translates into a trend of $\Upsilon_*^{3.6} \simeq 0.6$ in the center to an outer $\Upsilon_*^{3.6} \simeq 0.3$. Beyond the radius where $(J - K)$ (and therefore $\Upsilon_*^{3.6}$) could be reliably determined we assume a constant value $\Upsilon_*^{3.6} = 0.3$. The surface brightness profile shows evidence for a second component in the inner parts. Based on its rather modest appearance, it is not

Table 3
Mass Models with Fixed $\Upsilon_{\star}^{3.6}$ and Diet-Salpeter IMF

Name (1)	$\log M_{\star}^D$ (2)	$\langle \Upsilon_{\star,D}^{3.6} \rangle$ (3)	$\log M_{\star}^B$ (4)	$\langle \Upsilon_{\star,B}^{3.6} \rangle$ (5)	ISO Halo			NFW Halo		
					R_C (6)	ρ_0 (7)	χ_r^2 (8)	c (9)	V_{200} (10)	χ_r^2 (11)
NGC 925	10.01	0.65	16.86 ± 7.47	3.4 ± 0.5	2.15	<0.1	>500	2.81
NGC 2366	8.41	0.33	1.36 ± 0.07	34.8 ± 2.4	0.17	<0.1	>500	0.98
NGC 2403 (1 comp)	9.71	0.41	2.09 ± 0.05	81.2 ± 3.6	0.88	9.9 ± 0.2	109.5 ± 1.0	0.55
NGC 2403 (2 comp)	9.67	0.39	8.63	0.60	2.14 ± 0.05	77.9 ± 3.3	0.79	9.8 ± 0.2	110.2 ± 1.0	0.56
NGC 2841	11.04	0.74	10.40	0.84	2.03 ± 0.05	298.7 ± 14.9	0.27	16.1 ± 0.2	183.2 ± 1.2	0.42
NGC 2903 (outer)	10.15	0.61	9.33	1.30	$<0.01 \pm 0.09$	>1000	0.63	30.9 ± 0.6	112.9 ± 0.6	0.36
NGC 2976	9.25	0.55	>1000	11.7 ± 2.1	1.76	<0.1	>500	2.78
NGC 3031	10.84	0.80	10.11	1.00	5.25 ± 1.36	14.8 ± 4.2	3.93	3.0 ± 2.9	190.9 ± 161.1	4.36
NGC 3198 (1 comp)	10.40	0.80	3.22 ± 0.16	33.5 ± 3.0	0.84	7.5 ± 0.4	112.4 ± 2.1	1.37
NGC 3198 (2 comp)	10.45	0.80	9.46	0.73	4.97 ± 0.41	14.4 ± 2.0	2.15	5.1 ± 0.5	122.7 ± 4.9	2.88
IC 2574	9.02	0.44	7.23 ± 0.30	4.1 ± 0.1	0.17	<0.1	>500	1.81
NGC 3521	11.09	0.73	39.4 ± 90.4	1.3 ± 1.2	8.07	<0.1	403.2 ± 123.2	8.52
NGC 3621	10.29	0.59	5.54 ± 0.16	14.4 ± 0.6	0.62	3.7 ± 0.2	165.5 ± 5.9	0.81
NGC 4736	10.27	0.63	9.59 ^a	0.33 ^a	1.44 ± 1.57	22.4 ± 41.5	1.52	11.4 ± 9.8	35.2 ± 0.3	1.51
DDO 154	7.42	0.32	1.34 ± 0.06	27.6 ± 1.6	0.44	4.4 ± 0.4	58.7 ± 4.3	0.82
NGC 5055	11.09	0.79	9.32 ^b	0.11 ^b	45.63 ± 0.24	0.9 ± 0.2	8.13	<0.1	450.1 ± 32.4	10.31
NGC 6946	10.77	0.64	9.58	1.00	20.58 ± 3.77	5.4 ± 0.4	1.45	<0.1	>500	2.59
NGC 7331 (const) ^c	11.22	0.70	10.24	1.00	>1000	1.6 ± 0.1	2.93	<0.1	>500	4.08
NGC 7793	9.44	0.31	1.93 ± 0.15	77.2 ± 7.7	2.97	5.8 ± 1.4	156.6 ± 39.1	4.17
NGC 7793 (rising)	9.44	0.31	3.52 ± 0.51	50.9 ± 4.8	2.26	<0.1	>500	3.67

Notes. (2) Logarithm of the predicted stellar mass of the disk (M_{\odot}). (3) Average stellar mass-to-light ratio in the $3.6 \mu\text{m}$ band (M_{\odot}/L_{\odot}). (4) Logarithm of the predicted stellar mass of the bulge (M_{\odot}). (5) Average stellar mass-to-light ratio of the bulge component in the $3.6 \mu\text{m}$ band (M_{\odot}/L_{\odot}). (6) Core radius R_C and associated uncertainty (kpc). (7) Central density ρ_0 and associated uncertainty ($10^{-3} M_{\odot} \text{ pc}^{-3}$). (8) Reduced χ_r^2 . (9) NFW c parameter and associated uncertainty. (10) NFW parameter V_{200} and associated uncertainty (km s^{-1}). (11) Reduced χ_r^2 .

^a M_{bulge} is a free parameter. Predicted model values are $\Upsilon_{\star}^{3.6} = 0.9$ and $\log M_{\star}^B = 10.02$.

^b M_{bulge} is a free parameter. Predicted model values are $\Upsilon_{\star}^{3.6} = 1.3$ and $\log M_{\star}^B = 10.40$.

^c The model with the color gradient included severely overpredicts the data and is not listed here. Its parameters are $\Upsilon_{\star}^{3.6} = 0.96$ and $\log M_{\star}^D = 11.36$ for the main disk and $\Upsilon_{\star}^{3.6} = 1.08$ and $\log M_{\star}^B = 10.28$ for the inner disk.

clear though whether this constitutes a dynamically separate component. We therefore considered both cases. For the single-component case, we simply multiplied the surface brightness profile with the derived $\Upsilon_{\star}^{3.6}$ values. For the double-component case, we decomposed the profile in two exponential profiles. The outer component is described by a central surface brightness $\mu_0^{3.6} = 16.9 \text{ mag arcsec}^{-2}$ and a scale length $h = 1.81 \text{ kpc}$. The inner component has $\mu_0^{3.6} = 16.7 \text{ mag arcsec}^{-2}$ and $h = 0.41 \text{ kpc}$. We used the fitted model as a description for the inner disk. For the outer disk, we used the observed surface brightness distribution, with the inner disk model subtracted. We extended the observed outer disk profile with the corresponding fit at large radii where the disk was no longer directly observable.

The $(J - K)$ color shows a slight increase in the inner parts. For the inner disk, we therefore assumed a constant value of $\Upsilon_{\star}^{3.6} = 0.6$, whereas for the outer, main disk we assumed the single-disk color distribution, the only difference being that we adopted a constant $\Upsilon_{\star}^{3.6} = 0.5$ for the innermost ($R < 40''$) parts.

Figures 25 and 26 present the fits for the single and multiple disk models, respectively. The NFW models (fixed and free) are of the same quality as the free ISO model. The fixed $\Upsilon_{\star}^{3.6}$ ISO models are of a somewhat lower quality. NGC 2403 in combination with the ISO model prefers higher $\Upsilon_{\star}^{3.6}$ values than predicted from the infrared color.

6.3. NGC 2841

The surface brightness profiles of NGC 2841 are shown in Figure 27. The 2MASS J , H , and K profiles can be traced out to

$\sim 290''$, and the IRAC $3.6 \mu\text{m}$ profile out to $\sim 375''$. All surface brightness profiles show an extended outer exponential disk, as well as a more compact central component. We decompose the profile using a double exponential disk. For the outer disk we find $\mu_0 = 15.7 \text{ mag arcsec}^{-2}$ and $h = 4.20 \text{ kpc}$. The inner disk has parameters $\mu_0 = 13.5 \text{ mag arcsec}^{-2}$ and $h = 0.72 \text{ kpc}$. In subsequent modeling we use the inner disk model for the central component. For the outer component we use the total observed surface brightness profile with the inner disk model subtracted, extrapolated at large radii using the outer exponential model parameters. The surface brightness profile shows some evidence for central emission in excess of the exponential model. However, the central parts of the velocity field cannot be modeled due to lack of H I emission.

NGC 2841 possesses a modest color gradient, which results in a $\Upsilon_{\star}^{3.6}$ trend from $\Upsilon_{\star}^{3.6} \simeq 0.8$ in the inner parts to $\Upsilon_{\star}^{3.6} \sim 0.5$ in the outer parts. For radii beyond which the 2MASS color could not be reliably determined, we assume a constant $\Upsilon_{\star}^{3.6} = 0.5$. The color profile shows a slight reddening in the innermost part, but this occurs at radii where no velocity information is available.

The mass models are presented in Figure 28. For the ISO model, the disk mass obtained through a free fit is very close to the mass derived from the population synthesis modeling assuming a diet Salpeter IMF. The resulting halo has the highest (well-determined) central density in the sample. The NFW model with fixed $\Upsilon_{\star}^{3.6}$ is of slightly lower quality; its main problem is the underprediction of the velocity at the smallest radii. An increase in $\Upsilon_{\star}^{3.6}$ of the inner component when $\Upsilon_{\star}^{3.6}$

Table 4
Mass Models with Fixed $\Upsilon_{\star}^{3.6}$ and Kroupa IMF

Name (1)	$\log M_{\star}^D$ (2)	$\langle \Upsilon_{\star,D}^{3.6} \rangle$ (3)	$\log M_{\star}^B$ (4)	$\langle \Upsilon_{\star,B}^{3.6} \rangle$ (5)	ISO Halo			NFW Halo		
					R_C (6)	ρ_0 (7)	χ_r^2 (8)	c (9)	V_{200} (10)	χ_r^2 (11)
NGC 925	9.86	0.47	9.67 ± 1.27	5.9 ± 0.5	1.14	<0.1	>500	2.17
NGC 2366	8.26	0.23	1.32 ± 0.07	37.3 ± 2.4	0.16	<0.1	>500	1.01
NGC 2403 (1 comp)	9.56	0.29	1.49 ± 0.05	152.8 ± 7.5	1.04	12.4 ± 0.2	101.7 ± 0.7	0.57
NGC 2403 (2 comp)	9.52	0.26	8.48	0.43	1.52 ± 0.04	145.8 ± 6.9	0.97	12.3 ± 0.2	102.2 ± 0.7	0.57
NGC 2841	10.88	0.53	10.25	0.60	0.63 ± 0.04	3215.3 ± 371.8	0.22	18.9 ± 0.4	181.4 ± 1.0	0.23
NGC 2903 (outer)	10.00	0.43	9.18	0.92	$<0.01 \pm 0.09$	>1000	1.14	35.5 ± 0.7	111.8 ± 0.6	0.41
NGC 2976	9.10	0.39	5.09 ± 2.54	35.5 ± 3.1	0.50	<0.1	>500	1.90
NGC 3031	10.69	0.57	9.96	0.71	0.78 ± 0.19	754.2 ± 323.6	3.88	26.4 ± 2.5	94.6 ± 3.9	3.61
NGC 3198 (1 comp)	10.25	0.57	2.72 ± 0.13	46.9 ± 4.0	0.80	8.7 ± 0.4	109.7 ± 1.7	1.30
NGC 3198 (2 comp)	10.30	0.57	9.31	0.52	2.82 ± 0.19	44.0 ± 5.1	1.41	8.5 ± 0.5	110.4 ± 2.2	2.06
IC 2574	8.87	0.31	6.18 ± 0.21	5.0 ± 0.1	0.17	<0.1	>500	1.73
NGC 3521	10.94	0.52	2.50 ± 0.66	73.0 ± 30.6	4.75	8.9 ± 2.0	128.4 ± 16.4	5.55
NGC 3621	10.14	0.42	2.77 ± 0.10	48.9 ± 2.8	1.09	7.8 ± 0.2	120.2 ± 1.4	0.55
NGC 4736	10.12	0.44	9.56^a	0.31^a	$<0.01 \pm 0.65$	>1000	1.73	63.5 ± 24.2	42.4 ± 1.7	1.41
DDO 154	7.27	0.23	1.32 ± 0.06	28.5 ± 1.7	0.44	4.5 ± 0.4	58.0 ± 4.1	0.83
NGC 5055	10.94	0.56	9.81^b	0.34^b	11.73 ± 0.71	4.8 ± 0.4	1.03	2.1 ± 0.4	217.8 ± 21.2	1.45
NGC 6946	10.62	0.45	9.43	0.71	3.62 ± 0.16	45.7 ± 3.0	0.98	6.2 ± 0.5	183.8 ± 11.1	1.03
NGC 7331 (const) ^c	11.07	0.50	10.09	0.71	5.40 ± 0.31	24.4 ± 2.1	0.31	4.9 ± 0.4	200.0 ± 10.7	0.24
NGC 7793	9.29	0.22	1.46 ± 0.10	126.0 ± 12.2	3.56	9.1 ± 1.1	114.1 ± 12.2	3.74
NGC 7793 (rising)	9.29	0.22	1.98 ± 0.22	95.7 ± 10.7	4.08	<0.1	>500	2.06

Notes. (2) Logarithm of the predicted stellar mass of the disk (M_{\odot}). (3) Average stellar mass-to-light ratio in the $3.6 \mu\text{m}$ band (M_{\odot}/L_{\odot}). (4) Logarithm of the predicted stellar mass of the bulge (M_{\odot}). (5) Average stellar mass-to-light ratio of the bulge component in the $3.6 \mu\text{m}$ band (M_{\odot}/L_{\odot}). (6) Core radius R_C and associated uncertainty (kpc). (7) Central density ρ_0 and associated uncertainty ($10^{-3} M_{\odot} \text{ pc}^{-3}$). (8) Reduced χ_r^2 . (9) NFW c parameter and associated uncertainty. (10) NFW parameter V_{200} and associated uncertainty (km s^{-1}). (11) Reduced χ_r^2 .

^a M_{bulge} is a free parameter. Predicted model values are $\Upsilon_{\star}^{3.6} = 0.6$ and $\log M_{\star}^B = 9.87$.

^b M_{bulge} is a free parameter. Predicted model values are $\Upsilon_{\star}^{3.6} = 0.8$ and $\log M_{\star}^B = 10.25$.

^c The model with the color gradient included severely overpredicts the data and is not listed here. Its parameters are $\Upsilon_{\star}^{3.6} = 0.61$ and $\log M_{\star}^D = 11.21$ for the main disk and $\Upsilon_{\star}^{3.6} = 0.69$ and $\log M_{\star}^B = 10.13$ for the inner disk.

is released compensates for this, and yields a model of equal quality as the ISO model. For the Kroupa fixed $\Upsilon_{\star}^{3.6}$ the ISO model results in an extremely compact halo, probably indicating that $\Upsilon_{\star}^{3.6}$ is underestimated.

6.4. NGC 2903

The surface brightness profiles of NGC 2903 are shown in Figure 29. The 2MASS J , H , and K profiles can be traced out to $\sim 240''$, and the IRAC $3.6 \mu\text{m}$ profile out to $\sim 400''$. The break in the profile around $230''$ is due to the sudden change in inclination at this radius. The profile can be decomposed into two components: the inner one is modeled using an exponential disk with $\mu_0 = 13.6 \text{ mag arcsec}^{-2}$ and $h = 0.17 \text{ kpc}$. For the outer disk, we used the observed profile with the inner disk profile subtracted. At radii larger than $400''$ we used an exponential extrapolation of the main disk.

NGC 2903 shows a well-defined color gradient. For the inner disk, we assumed $\Upsilon_{\star}^{3.6} = 1.3$, which is the average value of $\Upsilon_{\star}^{3.6}$ within $20''$. For the outer disk, we assumed $\Upsilon_{\star}^{3.6} = 0.75$ in the innermost parts and $\Upsilon_{\star}^{3.6} = 0.4$ in the outermost parts. Between $20''$ and $150''$ we adopted the observed $\Upsilon_{\star}^{3.6}$ profile.

The rotation curve models for NGC 2903 are shown in Figure 30. It is immediately obvious that the inner part of NGC 2903 is not well fitted by the models. The models with $\Upsilon_{\star}^{3.6}$ fixed severely overpredict the data independent of IMF. Models with $\Upsilon_{\star}^{3.6}$ as a free parameter can only approximately fit the data by setting $\Upsilon_{\star}^{3.6} = 0$ for the inner disk. This large discrepancy is most likely due to the bar. A harmonic decomposition of the velocity field shows significant noncircular motions in the inner

1 kpc (Trachternach et al. 2008). Because of the low quality of the fits, we do not list them in Tables 3–6. An additional source of uncertainty could be the presence of a very dense inner molecular disk, with significant amounts of associated star formation (Planesas et al. 1997).

We performed an extra set of fits to those parts of the rotation curve that are unaffected by the central noncircular motions (the flat part of the curve at $R > 3.3 \text{ kpc}$). These are shown in Figure 31. We find that with $\Upsilon_{\star}^{3.6}$ as a free parameter, the resulting disk is dynamically more significant than predicted by population synthesis models and $(J - K)$ colors. The ISO model prefers a dynamically insignificant central component, whereas the NFW model prefers a central $\Upsilon_{\star}^{3.6}$ value close to the predicted one. Here also, the main disk is found to be more massive than predicted by the colors. The NFW model fits better than the ISO model but due to the presence of the noncircular motions, it is not clear whether this can be generalized to the entire rotation curve. For fixed $\Upsilon_{\star}^{3.6}$, the ISO model demands an extremely small core radius R_C and a very large central density ρ_0 in order to produce the flat halo rotation curve shown in Figure 31.

6.5. NGC 2976

The surface brightness profiles of NGC 2976 are shown in Figure 32. The 2MASS J , H , and K profiles can be traced out to $\sim 210''$. The H I disk and rotation curve extend only out to $150''$ and no extrapolations using exponential disks were necessary. The galaxy shows a well-defined color gradient, leading to a $\Upsilon_{\star}^{3.6}$ variation from $\Upsilon_{\star}^{3.6} \simeq 0.75$ in the inner parts to $\Upsilon_{\star}^{3.6} \simeq 0.3$

Table 5
ISO Mass Models with Free $\Upsilon_{\star}^{3.6}$

Name (1)	M_{\star}^D (2)	$\langle \Upsilon_{\star,D}^{3.6} \rangle$ (3)	f^D (4)	M_{\star}^B (5)	$\langle \Upsilon_{\star,B}^{3.6} \rangle$ (6)	f^B (7)	R^C (8)	ρ_0 (9)	χ_r^2 (10)
NGC 925	9.46	0.18	0.28 ± 0.07	5.65 ± 0.56	12.8 ± 1.8	0.68
NGC 2366	...	0.00 ^a	0.00 ^a	1.16 ± 0.06	50.8 ± 3.2	0.18
NGC 2403 (1 comp)	9.91	0.65	1.58 ± 0.04	3.76 ± 0.15	28.6 ± 1.9	0.56
NGC 2403 (2 comp)	9.66	0.38	0.97 ± 0.18	8.93	1.18	1.98 ± 0.11	2.51 ± 0.32	59.1 ± 14.3	0.49
NGC 2841	10.96	0.61	0.83 ± 0.05	10.40	0.83	0.99 ± 0.36	1.36 ± 0.75	674.8 ± 736.4	0.18
NGC 2903 (outer)	10.50	1.36	2.23 ± 0.28	...	0.00 ^a	0.00 ^a	1.01 ± 0.45	541.1 ± 480.5	0.36
NGC 2976	9.12	0.40	0.73 ± 0.03	∞	30.7 ± 2.3	0.51
NGC 3031	10.93	0.99	1.24 ± 0.54	9.54	0.22	0.27 ± 0.56	4.13 ± 23.4	12.2 ± 124.6	3.26
NGC 3198 (1 comp)	10.34	0.70	0.88 ± 0.07	2.71 ± 0.33	47.5 ± 11.4	0.81
NGC 3198 (2 comp)	10.30	0.57	0.71 ± 0.03	8.36	0.06	0.08 ± 0.04	1.86 ± 0.12	97.1 ± 12.2	0.36
IC 2574	8.37	0.10	0.23 ± 0.18	4.99 ± 0.34	6.7 ± 0.7	0.16
NGC 3521	10.77	0.34	0.47 ± 0.13	1.32 ± 0.76	370.2 ± 451.1	4.04
NGC 3621	10.30	0.60	1.02 ± 0.02	5.88 ± 0.32	13.0 ± 1.1	0.61
NGC 4736	10.23	0.58	0.92 ± 0.06	9.56	0.32	0.35 ± 0.09	0.04 ± 1.23	>500	1.53
DDO 154	8.45	3.46	10.82 ± 1.05	2.69 ± 0.24	9.0 ± 1.1	0.28
NGC 5055	10.88	0.24	0.62 ± 0.02	9.69	0.40	0.31 ± 0.01	7.15 ± 1.12	11.1 ± 3.1	0.87
NGC 6946	10.58	0.41	0.64 ± 0.15	9.50	0.83	0.83 ± 0.06	3.32 ± 1.23	55.6 ± 42.3	0.96
NGC 7331 (grad)	10.88	0.39	0.33 ± 0.04	10.22	0.95	0.88 ± 0.08	3.88 ± 0.98	58.0 ± 27.8	0.26
NGC 7331 (const)	11.10	0.32	0.76 ± 0.03	10.14	0.79	0.79 ± 0.09	9.35 ± 1.43	10.1 ± 2.4	0.26
NGC 7793	9.53	0.38	1.22 ± 0.14	2.40 ± 0.48	53.3 ± 15.7	2.83
NGC 7793 (rising)	9.57	0.42	1.35 ± 0.04	∞	25.7 ± 1.0	1.01

Notes. (2) Logarithm of the predicted stellar mass of the disk (M_{\odot}). (3) Average stellar mass-to-light ratio in the 3.6 μm band (M_{\odot}/L_{\odot}). (4) Scaling factor f^D with respect to the predicted diet Salpeter $\Upsilon_{\star}^{3.6}$ value listed in Table 3. The factor with respect to the Kroupa $\Upsilon_{\star}^{3.6}$ value listed in Table 4 can be obtained by multiplying with a factor of 1.41. (5) Logarithm of the predicted stellar mass of the bulge (M_{\odot}). (6) Average stellar mass-to-light ratio in the 3.6 μm band (M_{\odot}/L_{\odot}). (7) Scaling factor f^B with respect to the predicted diet Salpeter $\Upsilon_{\star}^{3.6}$ value listed in Table 3. The factor with respect to the Kroupa $\Upsilon_{\star}^{3.6}$ value listed in Table 4 can be obtained by multiplying with a factor of 1.41. (8) Core radius R_C and associated uncertainty (kpc). (9) Central density ρ_0 and associated uncertainty ($10^{-3} M_{\odot} \text{ pc}^{-3}$). (10) Reduced χ_r^2 .

^aThe stellar mass-to-light ratio $\Upsilon_{\star}^{3.6}$ was fixed to $\Upsilon_{\star}^{3.6} = 0$.

Table 6
NFW Mass Models with Free $\Upsilon_{\star}^{3.6}$

Name (1)	M_{\star}^D (2)	$\langle \Upsilon_{\star,D}^{3.6} \rangle$ (3)	f^D (4)	M_{\star}^B (5)	$\langle \Upsilon_{\star,B}^{3.6} \rangle$ (6)	f^B (7)	c (8)	V_{200} (9)	χ_r^2 (10)
NGC 925	...	0.00 ^a	0.00 ^a	<0.1	>500	1.11
NGC 2366	...	0.00 ^a	0.00 ^a	<0.1	>500	1.44
NGC 2403 (1 comp)	9.69	0.39	0.96 ± 0.05	10.2 ± 0.5	108.3 ± 1.9	0.55
NGC 2403 (2 comp)	9.59	0.33	0.83 ± 0.08	8.62	0.60	0.99 ± 0.09	10.9 ± 0.6	106.1 ± 1.9	0.55
NGC 2841	11.02	0.89	0.96 ± 0.04	10.58	1.26	1.50 ± 0.05	13.7 ± 0.8	190.9 ± 2.2	0.19
NGC 2903 (outer)	10.45	1.23	2.01 ± 0.23	9.46	1.78	1.37 ± 0.85	18.7 ± 1.4	119.3 ± 1.4	0.25
NGC 2976	8.88	0.23	0.42 ± 0.11	<0.1	>500	1.65
NGC 3031	10.92	0.96	1.20 ± 0.65	9.47	0.23	0.23 ± 0.27	9.3 ± 60.4	77.1 ± 96.5	3.31
NGC 3198 (1 comp)	10.27	0.60	0.75 ± 0.14	10.1 ± 1.8	107.6 ± 2.8	1.30
NGC 3198 (2 comp)	10.29	0.55	0.69 ± 0.03	...	0.00 ^a	0.00 ^a	11.2 ± 0.43	104.0 ± 0.7	0.37
IC 2574	...	0.00 ^a	0.00 ^a	<0.1	>500	1.66
NGC 3521	10.87	0.43	0.59 ± 0.21	14.0 ± 12.6	122.5 ± 20.4	5.48
NGC 3621	10.18	0.47	0.80 ± 0.03	6.5 ± 0.4	128.0 ± 3.3	0.52
NGC 4736	10.09	0.42	0.67 ± 0.18	9.51	0.15	0.28 ± 0.08	72.3 ± 54.9	43.4 ± 4.6	1.44
DDO 154	8.00	1.21	3.79 ± 2.84	3.4 ± 1.3	68.0 ± 16.8	0.81
NGC 5055	...	0.00 ^a	0.00 ^a	9.60	0.21	0.16 ± 0.01	33.3 ± 0.6	121.6 ± 0.5	0.57
NGC 6946	10.68	0.52	0.82 ± 0.06	9.35	0.59	0.59 ± 0.05	3.2 ± 2.6	281.4 ± 183.2	1.01
NGC 7331 (grad)	10.90	0.34	0.35 ± 0.02	10.13	0.75	0.69 ± 0.07	9.3 ± 1.2	171.2 ± 8.1	0.27
NGC 7331 (const)	11.08	0.64	0.64 ± 0.03	10.10	0.90	0.90 ± 0.09	3.3 ± 1.1	257.3 ± 56.9	0.24
NGC 7793	8.22	0.02	0.06 ± 0.96	15.3 ± 9.6	89.5 ± 20.7	3.53
NGC 7793 (rising)	8.96	0.10	0.33 ± 0.34	<0.1	>500	1.30

Notes. (2) Logarithm of the predicted stellar mass of the disk (M_{\odot}). (3) Average stellar mass-to-light ratio in the 3.6 μm band (M_{\odot}/L_{\odot}). (4) Scaling factor f^D with respect to the predicted $\Upsilon_{\star}^{3.6}$ value listed in Table 3. The factor with respect to the Kroupa $\Upsilon_{\star}^{3.6}$ value listed in Table 4 can be obtained by multiplying with a factor of 1.41. (5) Logarithm of the predicted stellar mass of the bulge (M_{\odot}). (6) Average stellar mass-to-light ratio in the 3.6 μm band (M_{\odot}/L_{\odot}). (7) Scaling factor f^B with respect to the predicted $\Upsilon_{\star}^{3.6}$ value listed in Table 3. The factor with respect to the Kroupa $\Upsilon_{\star}^{3.6}$ value listed in Table 4 can be obtained by multiplying with a factor of 1.41. (8) NFW parameter c and associated uncertainty (kpc). (9) NFW parameter V_{200} and associated uncertainty (km s^{-1}). (10) Reduced χ_r^2 .

^aThe stellar mass-to-light ratio $\Upsilon_{\star}^{3.6}$ was fixed to $\Upsilon_{\star}^{3.6} = 0$.

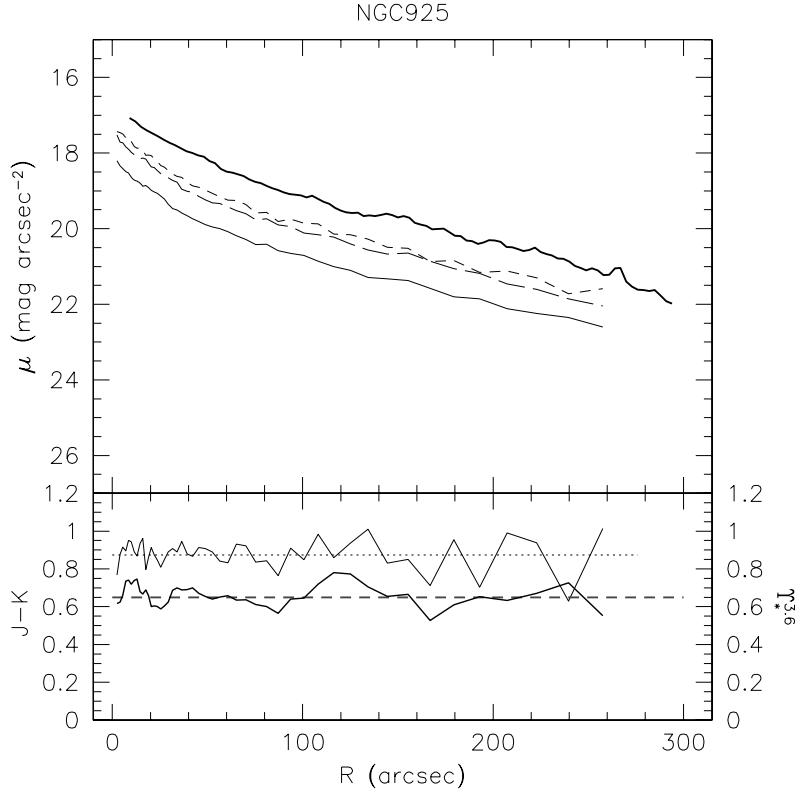


Figure 22. Surface brightness and $Y_*^{3.6}$ profiles for NGC 925. Top panel: The thin full line, long dashed curve, and short dashed curve show the 2MASS J , H and K surface brightness profiles, respectively. The thick full curve shows the Spitzer IRAC 3.6 μm surface brightness distribution. None are corrected for inclination. Bottom panel: The thin full curve shows the observed 2MASS $(J - K)$ distribution, with the thin dotted line indicating the average value. The thick full line shows the distribution of $Y_*^{3.6}$, derived from $(J - K)$ as described in the text. The thick dashed curve shows our assumed model for the $Y_*^{3.6}$ distribution of the disk.

in the outer parts. We adopted the $Y_*^{3.6}$ distribution as shown in Figure 32 without any further modifications.

The rotation curve fits are shown in Figure 33. The models with the fixed diet Salpeter $Y_*^{3.6}$ value slightly overpredict the observed rotation curve. The free- $Y_*^{3.6}$, ISO model also prefers a model very close to maximum disk, with a value for $Y_*^{3.6}$ close to the fixed $Y_*^{3.6}$ Kroupa value. The large value of R_C , seems to indicate NGC 2976 is located well within the core radius of its halo. The free- $Y_*^{3.6}$, NFW fit yields unphysical halo parameters trying to approximate a solid-body curve. It can only do this by choosing a large value of V_{200} and a small value of c . As mentioned before, c represents a collapse factor, and it is clear that a value $c < 1$ makes no physical sense. Similarly, it is unlikely that a fairly modest galaxy such as NGC 2976 is embedded in a halo with a typical velocity $V_{200} > 500 \text{ km s}^{-1}$.

6.6. NGC 3031

The surface brightness profiles of NGC 3031 are shown in Figure 34. The 2MASS J , H , and K profiles can be traced out to $\sim 750''$, and the 3.6 μm profile out to $\sim 850''$. The profiles show clear evidence for a central component. The outer disk shows a gradual flattening of the surface brightness profile toward larger radii. We modeled the central component using an exponential disk with parameters $\mu_0 = 12.2 \text{ mag arcsec}^{-2}$ and $h = 0.25 \text{ kpc}$. To describe the outer disk we simply subtracted the central exponential disk from the total light profile. The slight (~ 0.2 mag) residuals seen around $R \sim 100''$ do not impact on any subsequent modeling. The $(J - K)$ color profile shows

no significant color gradient, except for a central redder component. We assume a constant $Y_*^{3.6} = 0.8$ for the disk and $Y_*^{3.6} = 1.0$ for the central component.

The rotation curve mass models are shown in Figure 35. At first glance, it is already clear that the model fits deviate significantly from the observed rotation curve. Although the general trends in the curve are described well, smaller scale deviations clearly indicate the presence of significant noncircular motions. Given the presence of the prominent, grand-design spiral arms (causing the bump at $R \sim 7.5 \text{ kpc}$), and M81's location in an interacting system, this should not come as a surprise. The fit with fixed $Y_*^{3.6}$ yields χ_r^2 values that are only slightly inferior to the free $Y_*^{3.6}$ fits.

6.7. NGC 3198

The surface brightness profiles of NGC 3198 are shown in Figure 36. The 2MASS J , H , and K profiles can be traced out to $\sim 240''$, and the 3.6 μm profile out to $\sim 250''$. The profiles show a central component, as well as a “shoulder” in the surface brightness around $R \sim 50''$. We initially model the system using two components. For the innermost component we use an exponential disk with parameters $\mu_0 = 15.4 \text{ mag arcsec}^{-2}$ and $h = 0.56 \text{ kpc}$. The profile of the main disk is derived by subtracting the inner component model from the total luminosity profile and is extended beyond $R \sim 240''$ by an exponential disk model with $\mu_0 = 16.2 \text{ mag arcsec}^{-2}$ and $h = 3.06 \text{ kpc}$.

The most striking feature in the $(J - K)$ color distribution is the sudden reddening in the innermost couple of arcseconds. At face value, this would imply a steep increase in $Y_*^{3.6}$ in the inner-

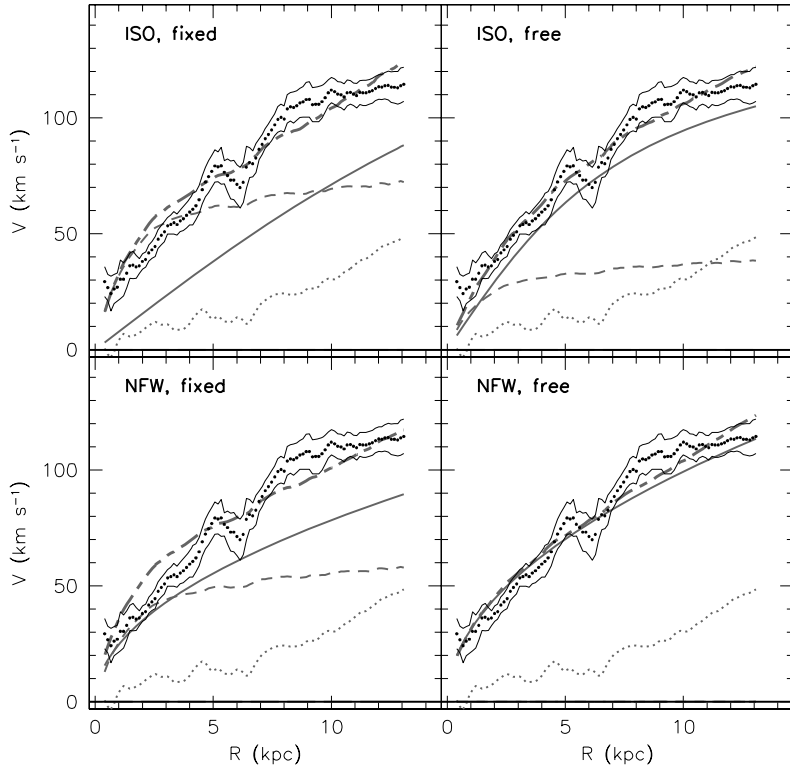


Figure 23. ISO and NFW rotation curve fits for NGC 925. The top row shows fits using the ISO halo. The bottom row shows fits assuming the NFW model. The left-hand column shows the fits assuming fixed (predicted) values of $\Upsilon_*^{3.6}$. The right-hand column shows the fits produced with a free $\Upsilon_*^{3.6}$. In all panels the dots represent the observed curve and the thin full lines represent the uncertainties. The gray dotted curve shows the rotation curve of the gas and the thin dashed gray curve shows the rotation curve of the stellar disk. The thick, gray full curve shows the resulting rotation curve of the halo. The thick long-short dashed curve the resulting best-fit model rotation curve.

most parts. This might indicate an additional (third) compact, central component. Alternatively, it could indicate the presence of a centrally-concentrated pronounced dust component. Whatever the cause, the steep increase in color only affects the very innermost point of the rotation curve and we will not model it. Adding a third component would increase the number of possible parameter combinations, but without obvious benefit. We therefore adopt the $\Upsilon_*^{3.6}$ profile as observed, but assume a constant $\Upsilon_*^{3.6} = 0.8$ for $R > 125''$, as well as a constant $\Upsilon_*^{3.6} = 0.7$ for $R < 10''$, as indicated in Figure 36.

The rotation curve fits are shown in Figure 37. In the case of fixed $\Upsilon_*^{3.6}$, the inner component clearly overestimates the rotation velocity, indicating that it is likely to be dynamically less important than suggested by the models (assuming the rotation curve is not affected; see below). With $\Upsilon_*^{3.6}$ as a free parameter, the outer disk ends up being less massive than predicted for both models. The central component is also fitted with a much smaller $\Upsilon_*^{3.6}$. For the ISO model, we find an inner component ~ 10 times lighter than predicted, whereas the NFW model results in a negative, hence unphysical, value for $\Upsilon_*^{3.6}$. We therefore fixed its value to $\Upsilon_*^{3.6} = 0$, with little impact on the results for the outer disk. We checked whether modeling the inner component as a spherical bulge instead of an exponential disk changed the results, but found this had a negligible effect on the outcome. Because of the apparent insignificance of the inner component, we also investigated if a single-disk model could explain the data. The results are also given in Figure 38. It is clear that independent of the choice for halo model, the inner radii cannot be well fitted.

The small value of $\Upsilon_*^{3.6}$ for the inner disk makes the free $\Upsilon_*^{3.6}$ fits less satisfactory. The low $\Upsilon_*^{3.6}$ values in the inner parts seems to contradict the sudden reddening in the inner $10''$, suggesting a *higher* $\Upsilon_*^{3.6}$ value. A close inspection of the IRAC 3.6 μm image indicates the presence of a short bar at a small angle with the minor axis, which could mean that the rotation velocities are affected by noncircular motions, thus giving incorrect values for $\Upsilon_*^{3.6}$. However, a harmonic decomposition of the velocity field shows only small noncircular motions (of order a few km s^{-1}) in the inner parts of the disk; see Trachternach et al. (2008).

In an independent analysis, Bottema et al. (2002) also note the presence of a possible bar in a K' image of NGC 3198. They argue that having a bar roughly parallel to the minor axis would *increase* the apparent rotation velocities in the inner region (Teuben & Sanders 1985). If this is indeed what is happening in NGC 3198, then the true rotation velocity in the inner parts must be even lower than we now observe, thus making the inner disk even less massive. Clearly there is scope here for a more extensive study of the dynamics in the inner part of NGC 3198.

6.8. NGC 3521

The surface brightness profiles of NGC 3521 are shown in Figure 39. The 2MASS J , H , and K profiles can be traced out to $\sim 250''$, and the 3.6 μm profile out to the edge of the H₁ disk. The photometric analysis is made difficult by the faint stellar halo surrounding the main disk. It is significantly extended along the minor axis, which, through the ellipse integration used, results in a flattening of the surface brightness

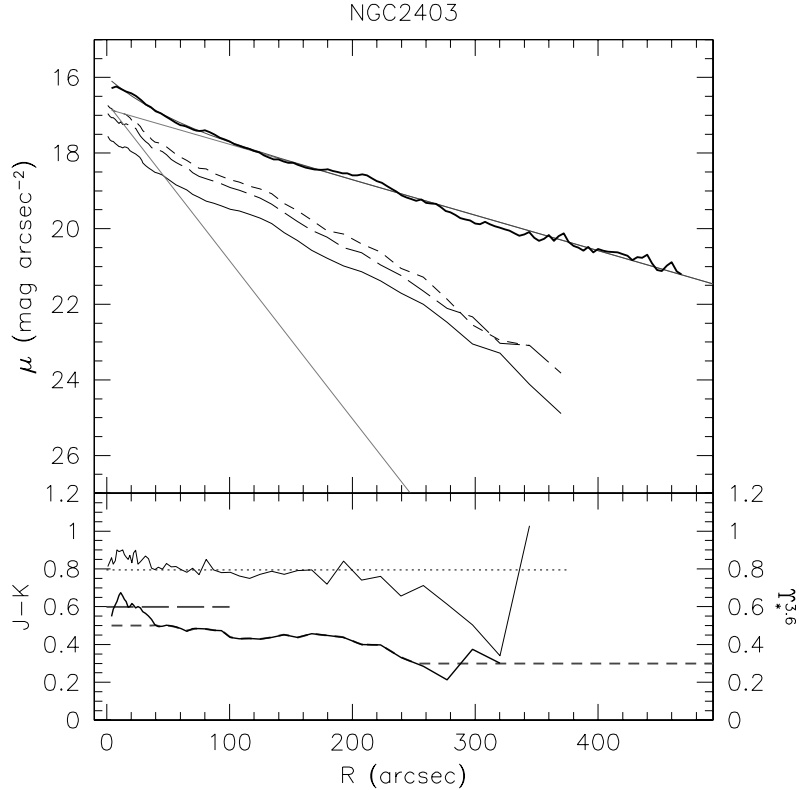


Figure 24. Surface brightness and $Y_*^{3.6}$ profiles for NGC 2403. Lines and symbols are as in Figure 22. In addition, the thin gray lines in the top panel show the decomposition of the profile in multiple exponential disk models. The long-dashed gray line in the bottom panel shows the assumed value of $Y_*^{3.6}$ for the inner disk.

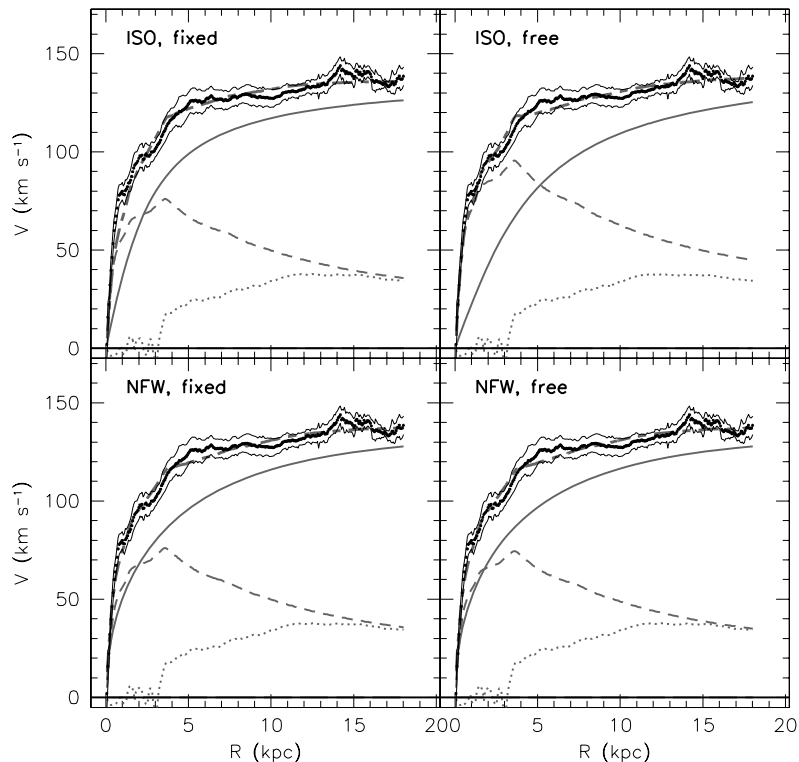


Figure 25. ISO and NFW rotation curve fits for the single-disk model of NGC 2403. Symbols and lines are as in Figure 23.

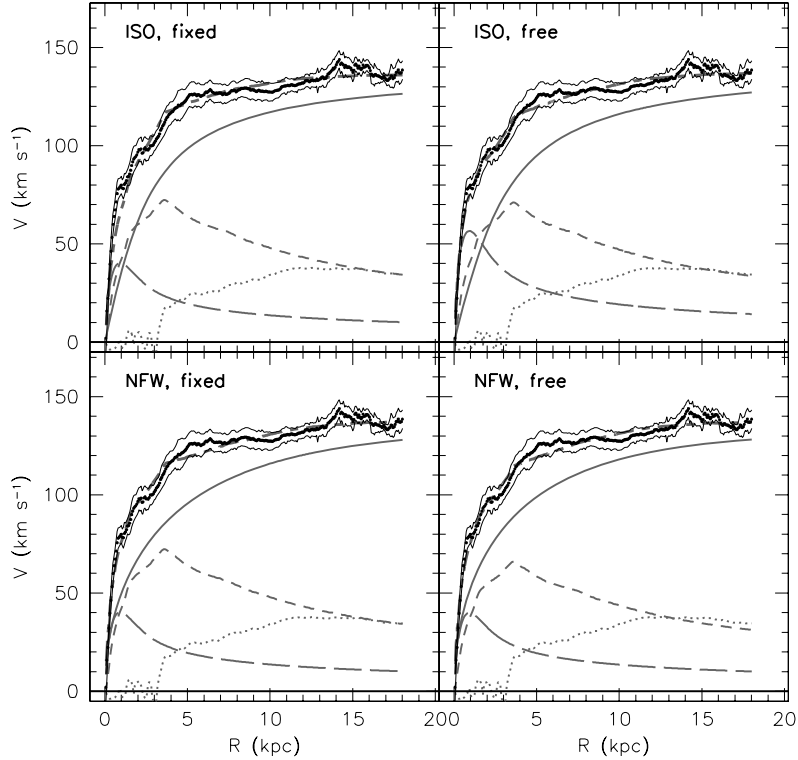


Figure 26. ISO and NFW rotation curve fits for the multiple-disk model of NGC 2403. Symbols and lines are as in Figure 23. In addition, the long-dashed gray curve represents the rotation curve of the inner disk.

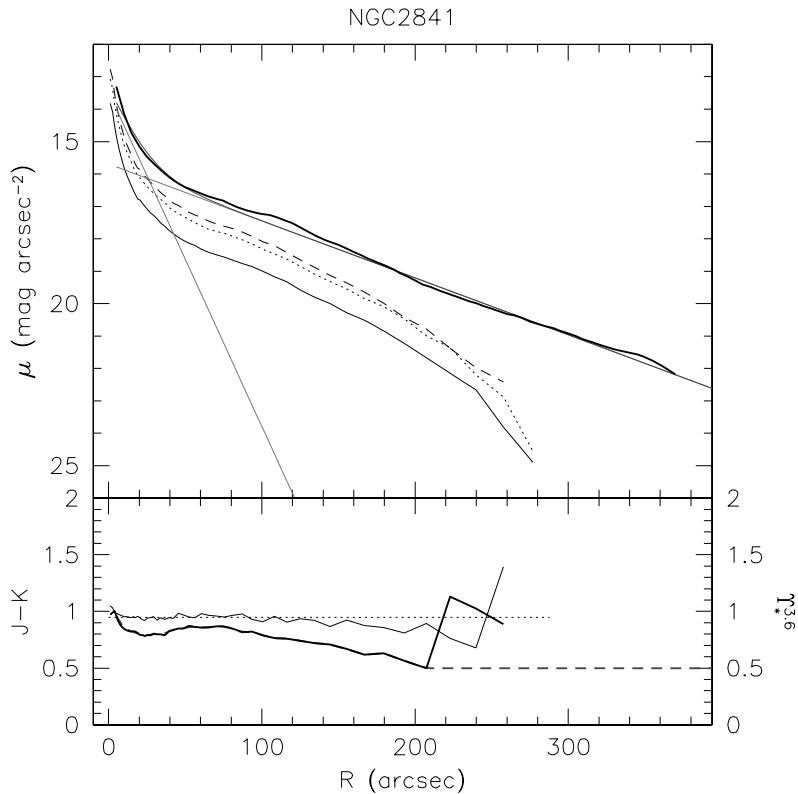


Figure 27. Surface brightness and $Y_{4^3 \cdot 6}^{3.6}$ profiles for NGC 2841. Lines and symbols are as in Figure 24.

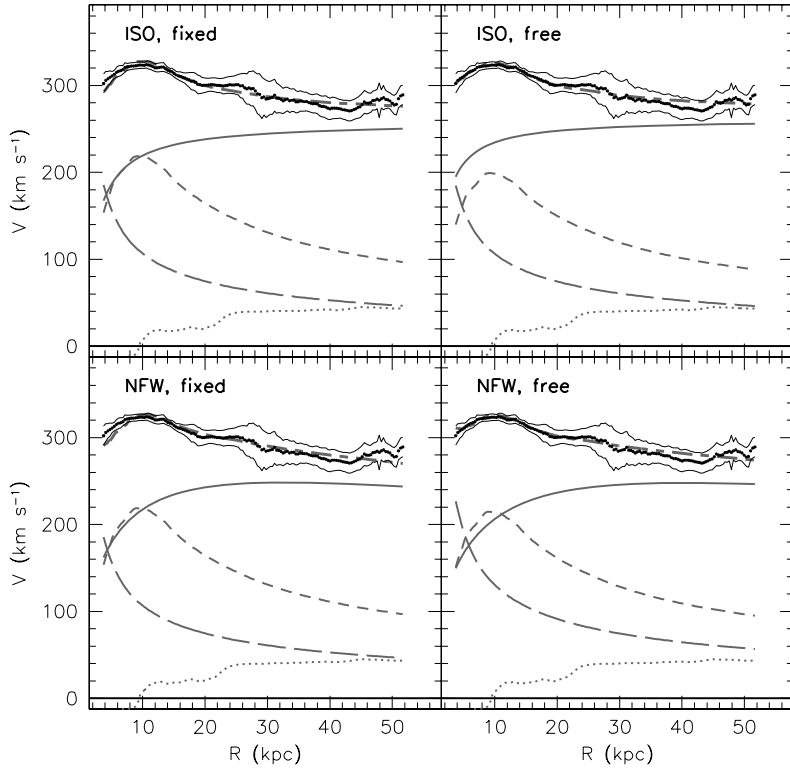


Figure 28. ISO and NFW rotation curve fits for NGC 2841. Lines and symbols are as in Figure 26.

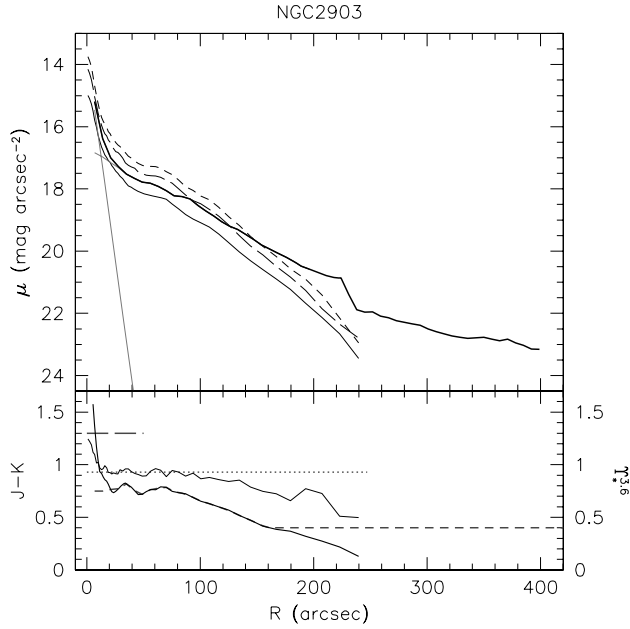


Figure 29. Surface brightness and $\Gamma_{\star}^{3.6}$ profiles for NGC 2903. Lines and symbols are as in Figure 24.

profile at larger radii. For this reason, results from the stellar decomposition are more uncertain than for other galaxies in the current sample.

We treat the stellar disk as a single component. A clear color gradient is present. The value for $\Gamma_{\star}^{3.6}$ changes from ~ 1 in the center to ~ 0.6 in the outer parts. Beyond the last reliable

2MASS radius, we assume a constant $\Gamma_{\star}^{3.6} = 0.6$. The rotation curve models are presented in Figure 40. Neither model fits perfectly, but both give reasonable $\Gamma_{\star}^{3.6}$ ratios. Assuming the fixed $\Gamma_{\star}^{3.6}$ values, it follows that the dynamics of NGC 3521 are dominated by its stars.

6.9. NGC 3621

The surface brightness profiles of NGC 3621 are shown in Figure 41. The 2MASS J , H , and K profiles can be traced out to $\sim 320''$, and the $3.6 \mu\text{m}$ profile out to $\sim 400''$. The latter profile shows slight evidence for a change in scale length around $R \sim 200''$. However, neither the lack of a clear break in the color gradient, nor the morphology, nor the (small) deviation from a single exponential disk is enough justification for a two-disk model. We extended the disk to larger radii using an exponential fit to radii $200'' < R < 400''$ and with parameters $\mu_0 = 16.6 \text{ mag arcsec}^{-2}$ and $h = 2.61 \text{ kpc}$. A small color gradient is visible in the 2MASS data which results in a gradient in $\Gamma_{\star}^{3.6}$ from $\Gamma_{\star}^{3.6} \simeq 0.8$ in the inner parts to $\Gamma_{\star}^{3.6} \simeq 0.4$ in the outer parts. Due to the increased uncertainty in the 2MASS color measurement in the outermost parts, we assumed $\Gamma_{\star}^{3.6} = 0.45$ for $R > 150''$, as indicated in Figure 41.

The rotation curve fits are presented in Figure 42. It is interesting how well the best (free) fit and the fixed diet Salpeter fit for the ISO halo agree with each other. Similarly, the free NFW fit yields a value of $\Gamma_{\star}^{3.6}$ very close to the Kroupa fixed $\Gamma_{\star}^{3.6}$ value, a clear illustration of how the NFW model prefers lighter disks in order to accommodate its steeper halo mass-density profile. The free ISO and NFW fits are of identical quality, and on the basis of these data it is difficult to single out a favorite model for NGC 3621.

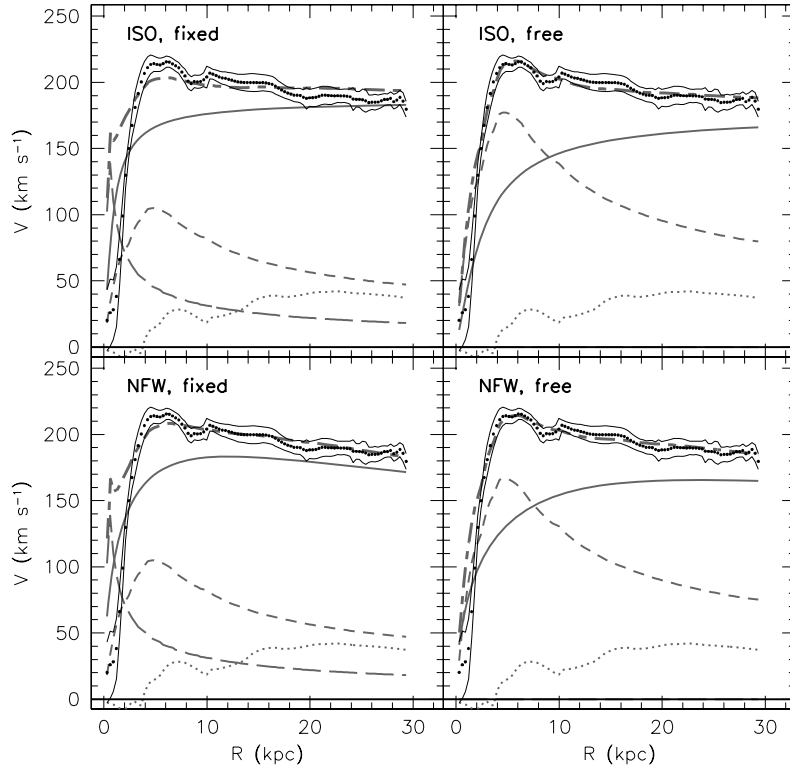


Figure 30. ISO and NFW rotation curve fits for NGC 2903 for the entire radial range. Lines and symbols are as in Figure 26.

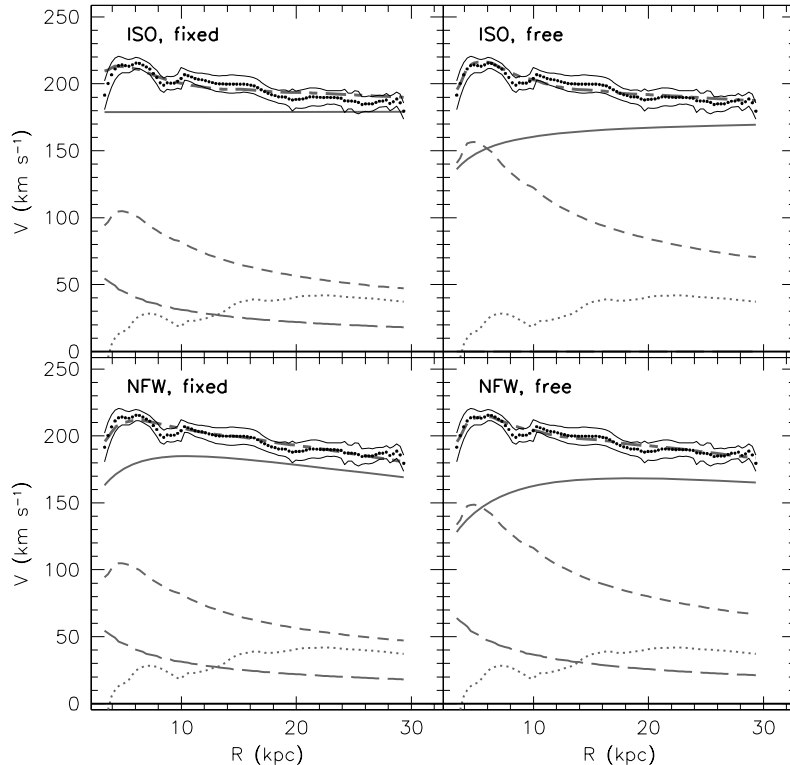


Figure 31. ISO and NFW rotation curve fits for NGC 2903. Only radii $R > 3.3$ kpc are considered here. Lines and symbols are as in Figure 26. The horizontal line in the top-left panel represents the degenerate halo rotation curve; see the text for a description.

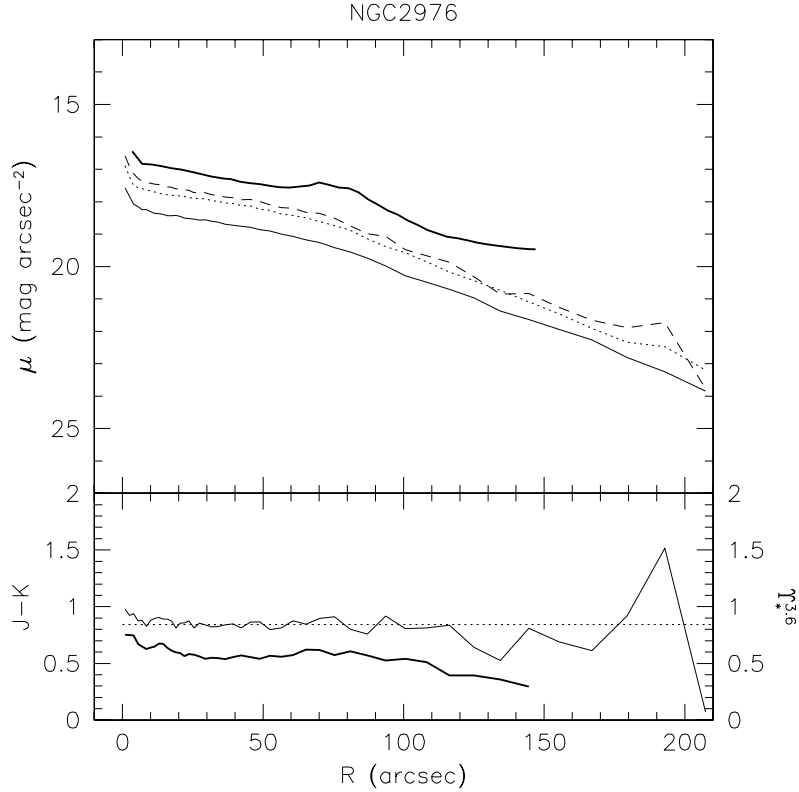


Figure 32. Surface brightness and $\gamma_{3.6}^{3.6}$ profiles for NGC 2976. Lines and symbols are as in Figure 24.

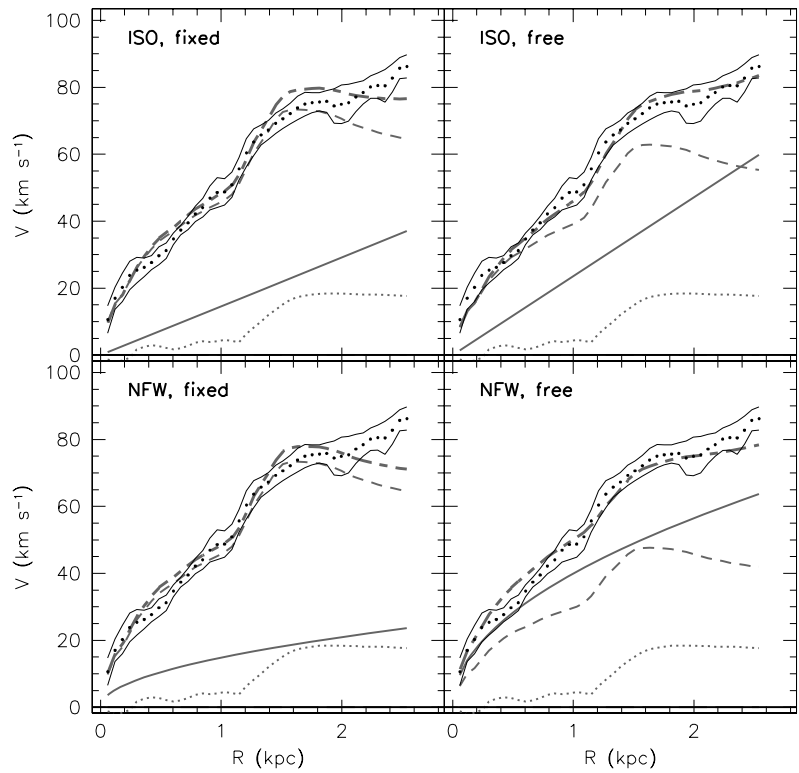


Figure 33. ISO and NFW rotation curve fits for NGC 2976. Lines and symbols are as in Figure 25.

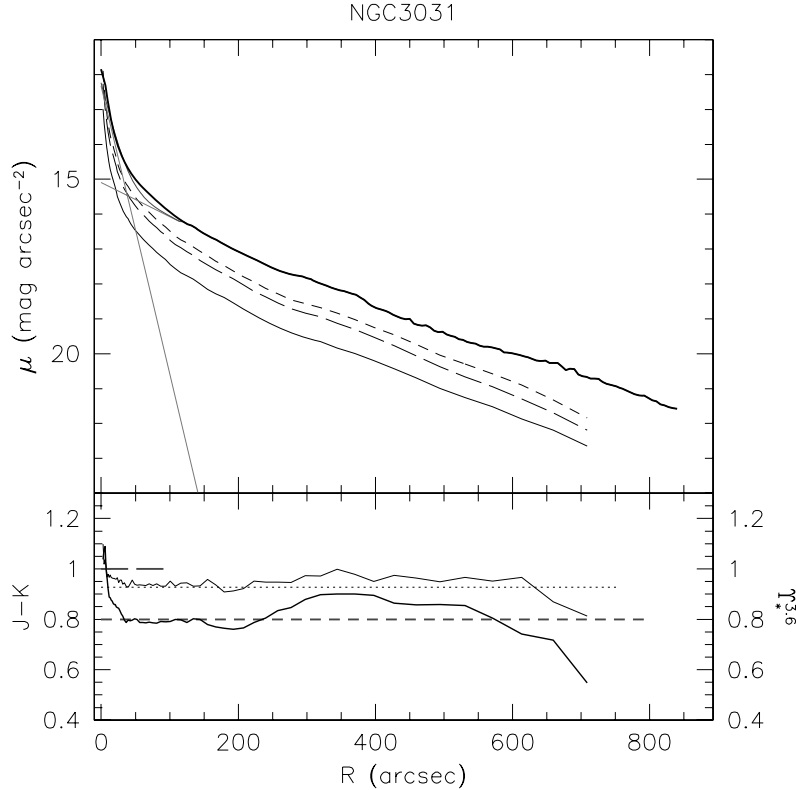


Figure 34. Surface brightness and $\gamma_*^{3.6}$ profiles for NGC 3031. Lines and symbols are as in Figure 24.

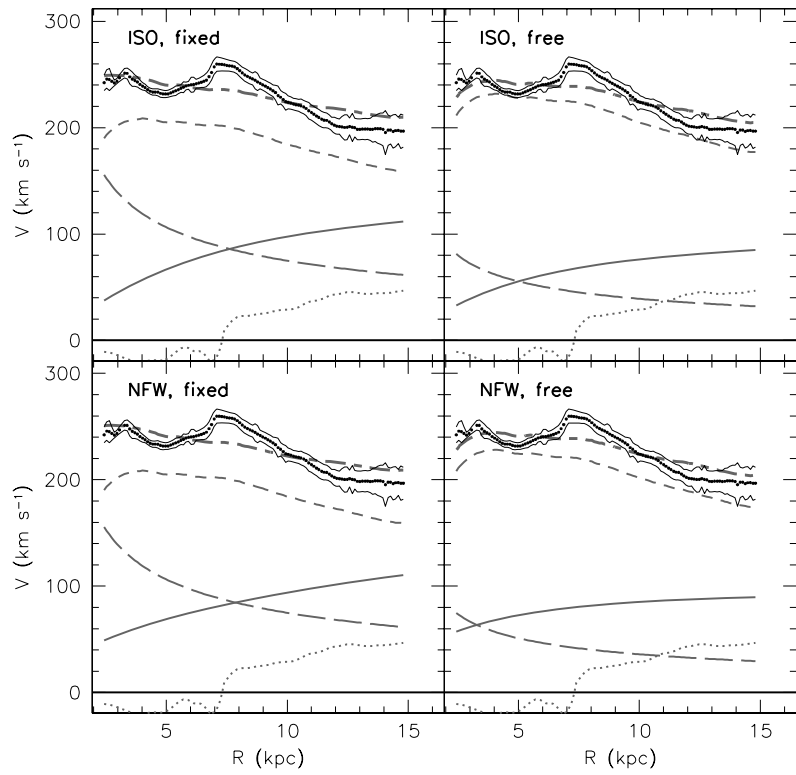


Figure 35. ISO and NFW rotation curve fits for NGC 3031. Lines and symbols are as in Figure 26.

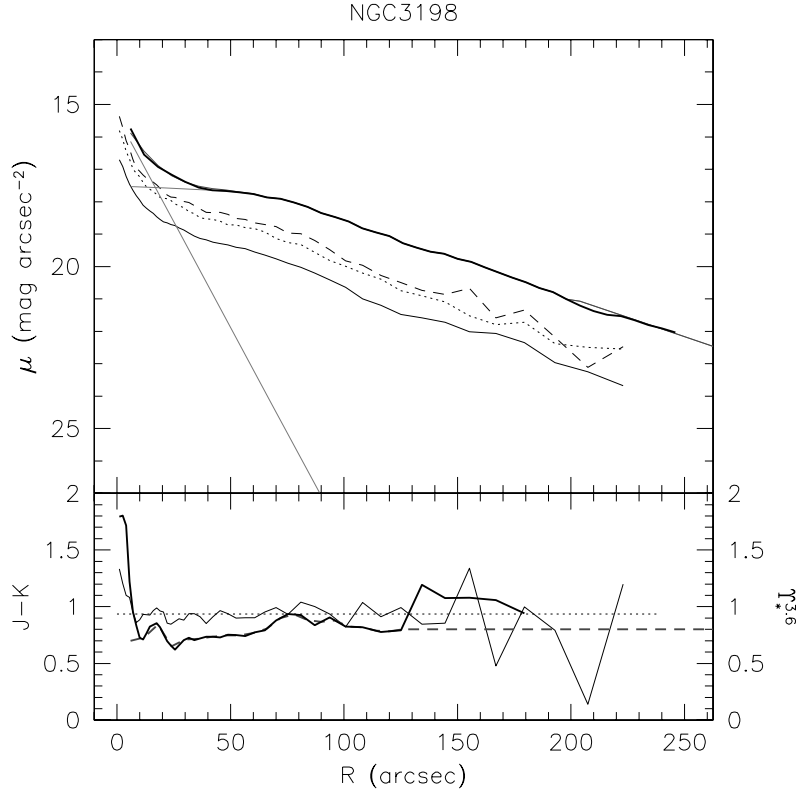


Figure 36. Surface brightness and $\gamma_*^{3.6}$ profiles for NGC 3198. Lines and symbols are as in Figure 24.

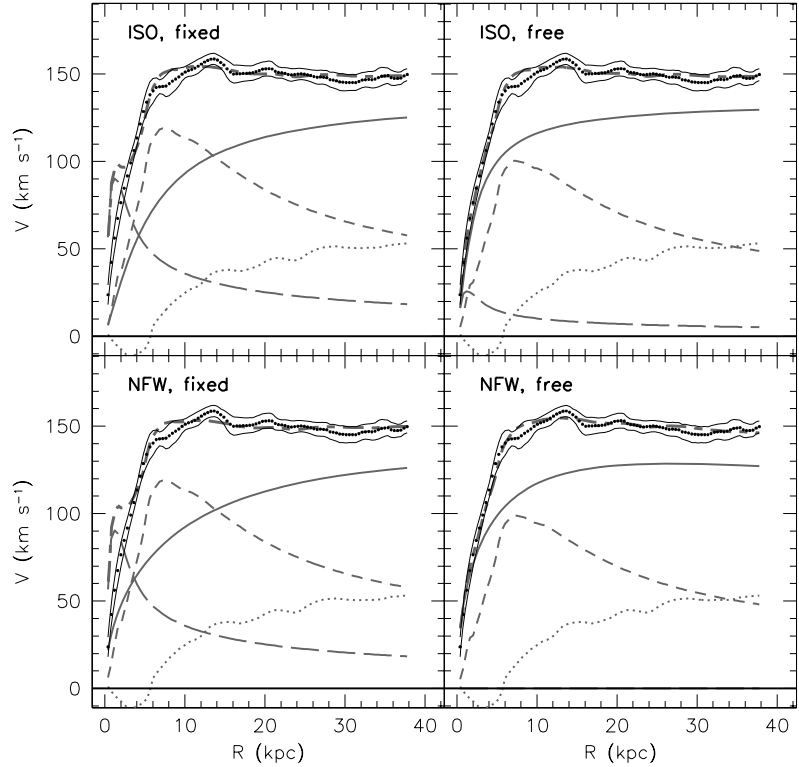


Figure 37. ISO and NFW rotation curve fits for the multiple-disk model of NGC 3198. Lines and symbols are as in Figure 26.

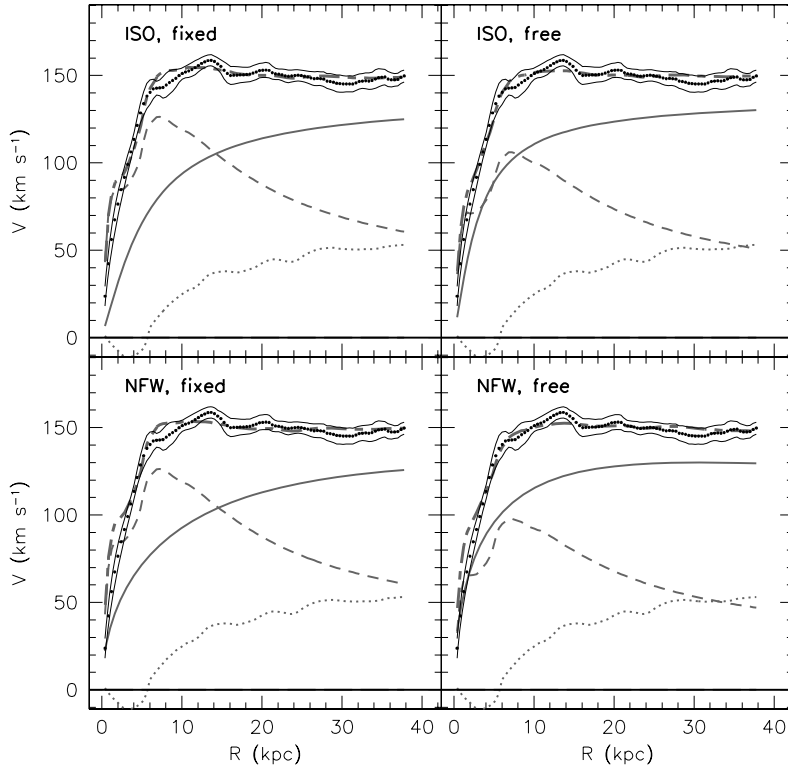


Figure 38. ISO and NFW rotation curve fits for the single-disk model of NGC 3198. Lines and symbols are as in Figure 25.

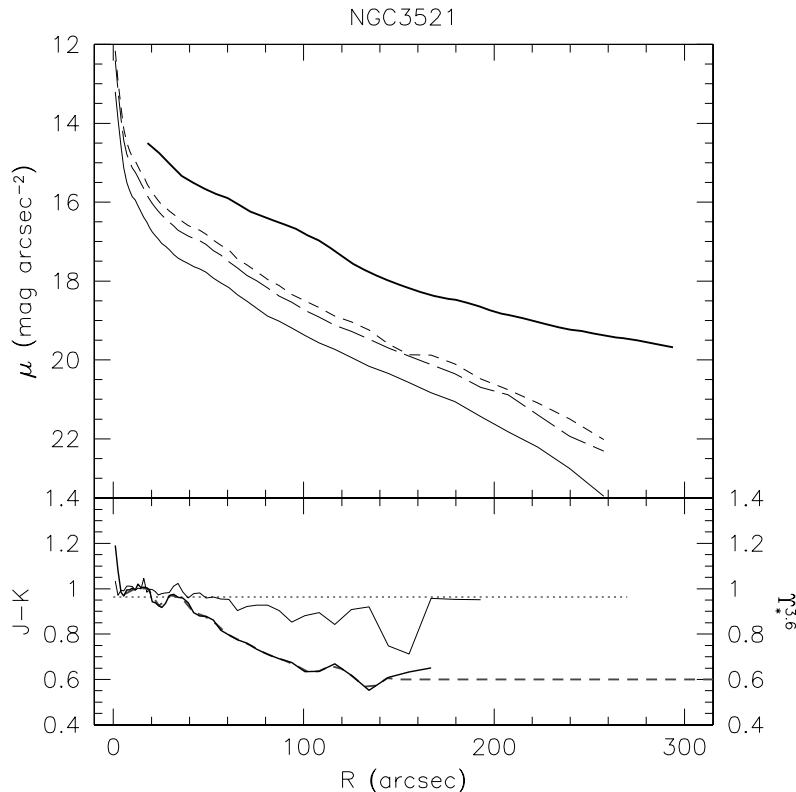


Figure 39. Surface brightness and $M^3.6$ profiles for NGC 3521. Lines and symbols are as in Figure 24.

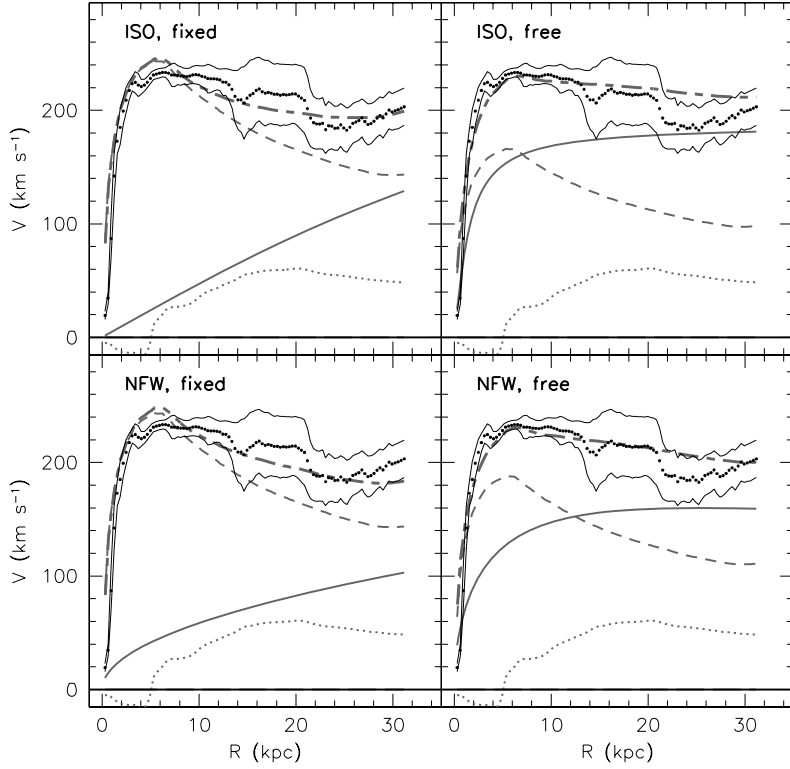


Figure 40. ISO and NFW rotation curve fits for NGC 3521. Lines and symbols are as in Figure 25.

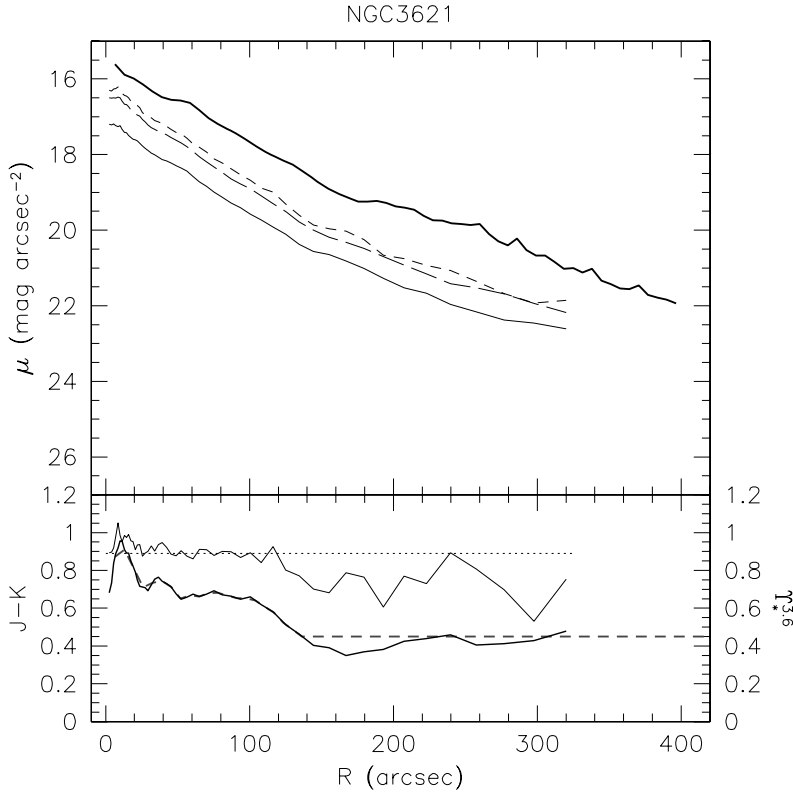


Figure 41. Surface brightness and $Y_{\star}^{3,6}$ profiles for NGC 3621. Lines and symbols are as in Figure 24.

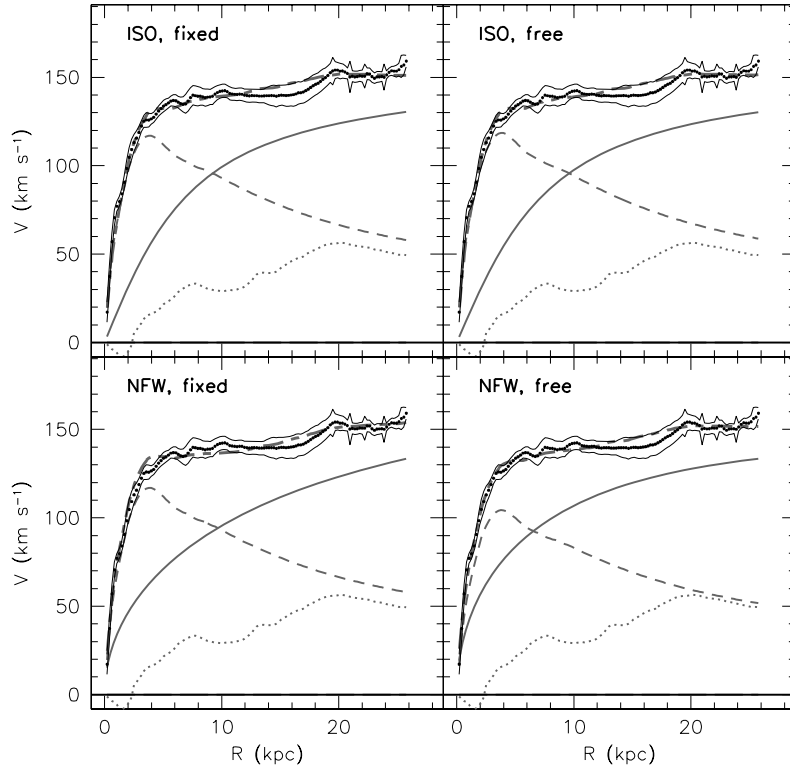


Figure 42. ISO and NFW rotation curve fits for NGC 3621. Lines and symbols are as in Figure 25.

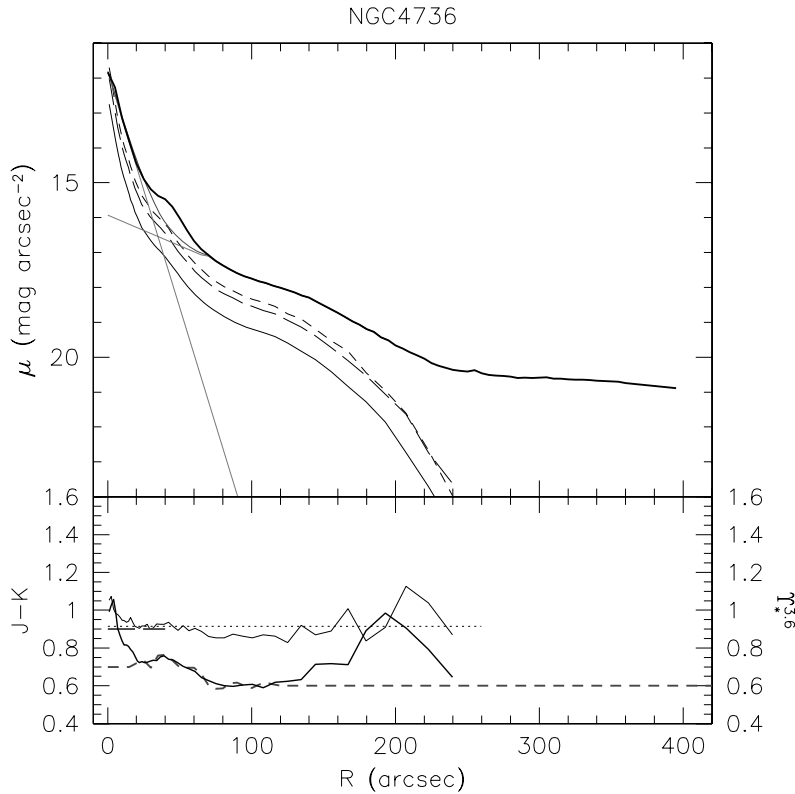


Figure 43. Surface brightness and $Y_r^{3.6}$ profiles for NGC 4736. Lines and symbols are as in Figure 24.

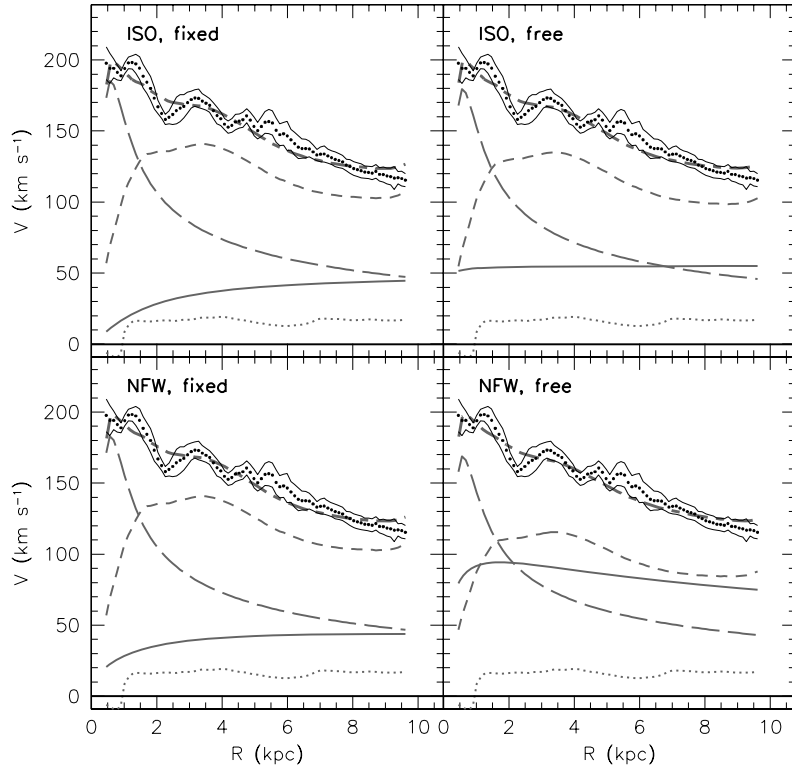


Figure 44. ISO and NFW rotation curve fits for NGC 4736. Lines and symbols are as in Figure 26.

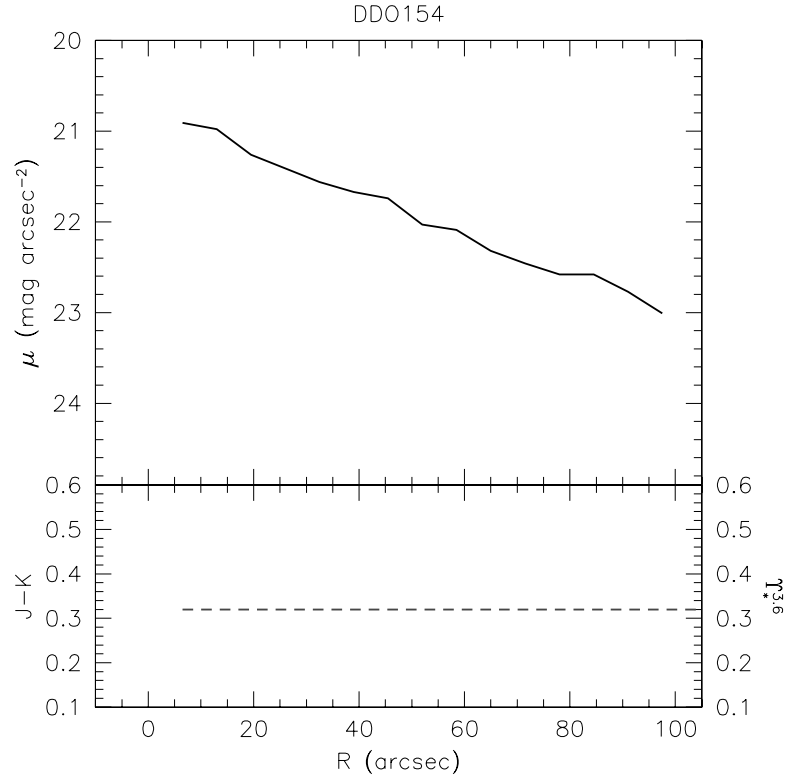


Figure 45. Surface brightness and $\Upsilon_*^{3.6}$ profiles for DDO 154. Lines and symbols are as in Figure 24.

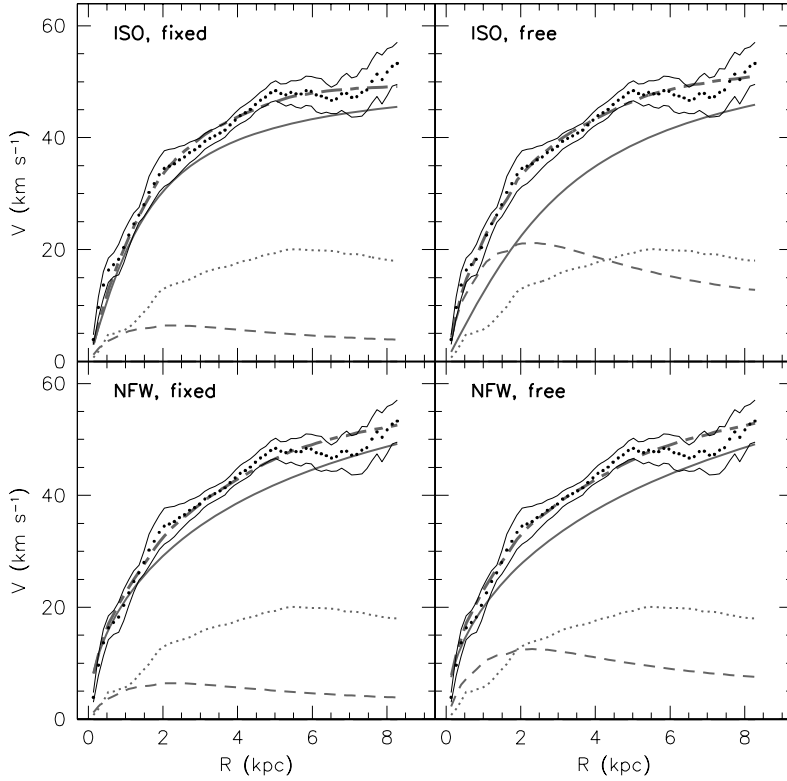


Figure 46. ISO and NFW rotation curve fits for DDO 154. Lines and symbols are as in Figure 25.

6.10. NGC 4736

The surface brightness profiles of NGC 4736 are shown in Figure 43. The 2MASS J , H , and K profiles can be traced out to $\sim 250''$, whereas the $3.6 \mu\text{m}$ profile can be traced out to the edge of the H α disk at $\sim 400''$.

The stellar component of NGC 4736 has a complex structure. A prominent stellar ring can be seen in various wavelengths at a radius $R \sim 40''$. The ring, visible in the $3.6 \mu\text{m}$ image, is also prominently visible in the 20 cm radio continuum. The presence of this fairly strong continuum suggests active star formation and may mean that at this particular radius the assumption that the $3.6 \mu\text{m}$ emission is proportional to the stellar mass is not valid. For this reason, we will not take this feature into account in our subsequent analysis of the surface brightness profile. The IRAC $3.6 \mu\text{m}$ profile flattens out at $250'' \lesssim R \lesssim 400''$, caused by the faint stellar ring surrounding the main body of NGC 4736. At larger radii (beyond the edge of the H α disk) the profile starts decreasing again. Also visible is a significant steepening in the inner parts. We will treat this as evidence for a separate central component with parameters $\mu_0 = 11.8 \text{ mag arcsec}^{-2}$ and $h = 0.26 \text{ kpc}$. To model the outer disk, we fitted an exponential disk to the radial range $80'' < R < 240''$ and found parameters $\mu_0 = 15.9 \text{ mag arcsec}^{-2}$ and $h = 1.99 \text{ kpc}$. We used the extrapolated fit for radii $R < 80''$ and the observed radial surface brightness for $R > 80''$.

NGC 4736 exhibits a small color gradient in the outer parts with a steeper inner reddening. We have adopted a constant value of $\Upsilon_*^{3.6} = 0.6$ for the outer disk beyond the last reliable 2MASS ($J - K$) value, and have additionally assumed a constant $\Upsilon_*^{3.6} = 0.7$ for the innermost $20''$. For the central disk, we assume a constant $\Upsilon_*^{3.6} = 0.9$ which is the average value for $R > 20''$.

The rotation curves are shown in Figure 44. It is immediately obvious that NGC 4736 must be close to maximum disk. The predicted $\Upsilon_*^{3.6}$ value for the inner disk yields a curve that overestimates the rotation velocity (not shown here). We therefore left $\Upsilon_*^{3.6}$ of the inner disk as a free parameter after fixing the $\Upsilon_*^{3.6}$ value of the main disk. This resulted in an inner disk mass of about a factor of ~ 2 less than predicted (and is the model shown in Figure 44). While the discrepancies are slightly less for the Kroupa $\Upsilon_*^{3.6}$ values, the resulting models still over-predict the rotation velocity. Because of these uncertainties and because of the large noncircular motions in this galaxy (Trachternach et al. 2008), it is virtually impossible to say anything definite about the distribution of dark matter in this galaxy based purely on rotation curve arguments.

6.11. DDO 154

DDO 154 is barely detected in the 2MASS images and we cannot therefore use the same ($J - K$) color method as with the other galaxies. We therefore use the ($B - V$) and ($B - R$) colors as proxies, as described in Oh et al. (2008). For the color, we use the values given in Carignan & Beaulieu (1989): $(B - V) = 0.37 \pm 0.06$ and $(B - R) = 0.64 \pm 0.07$. No significant color gradient is detected, and we therefore assume a constant color as a function of radius in our models. Using the equations from Oh et al. (2008), we find values $\Upsilon_*^{3.6} = 0.34 \pm 0.04$ using the ($B - V$) colors and $\Upsilon_*^{3.6} = 0.31 \pm 0.02$ using the ($B - R$) colors. We adopt the weighted average $\Upsilon_*^{3.6} = 0.32$ as our best estimate. The IRAC $3.6 \mu\text{m}$ profile can be described by a single exponential disk with $\mu_0 = 20.8 \text{ mag arcsec}^{-2}$ and $h = 0.72 \text{ kpc}$.

The rotation curves are shown in Figure 46. The ISO model consistently fits better than the NFW model. The latter

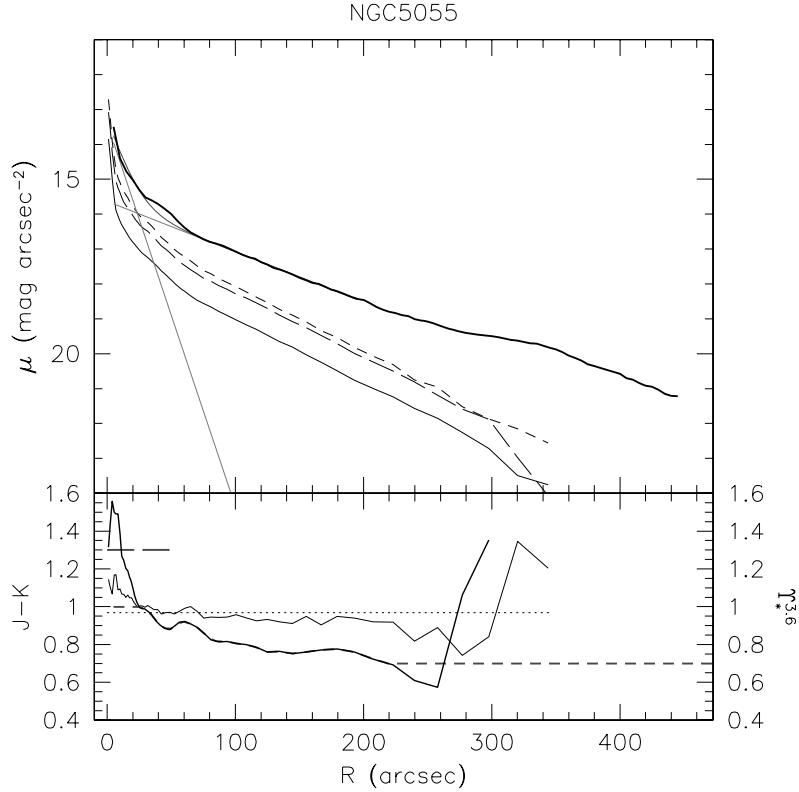


Figure 47. Surface brightness and $\gamma_{\star}^{3.6}$ profiles for NGC 5055. Lines and symbols are as in Figure 24.

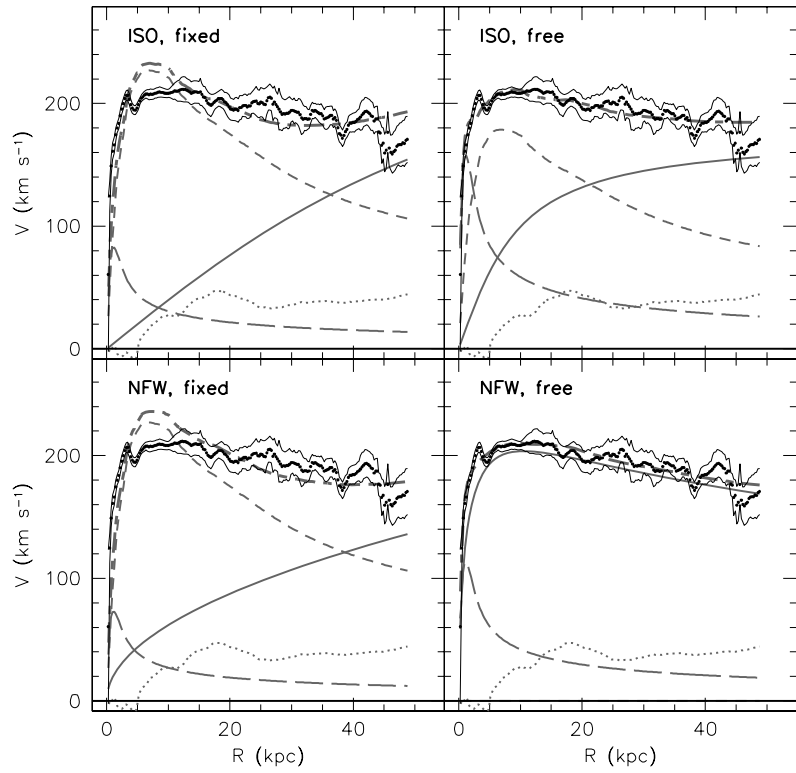


Figure 48. ISO and NFW rotation curve fits for NGC 5055. Lines and symbols are as in Figure 26.

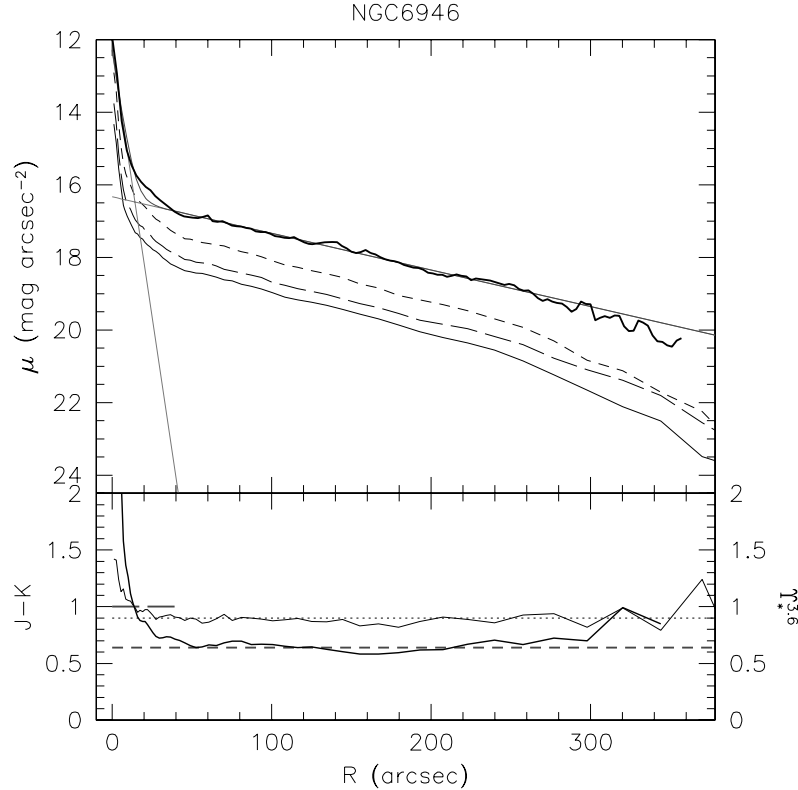


Figure 49. Surface brightness and $\Upsilon_\star^{3.6}$ profiles for NGC 6946. Lines and symbols are as in Figure 24.

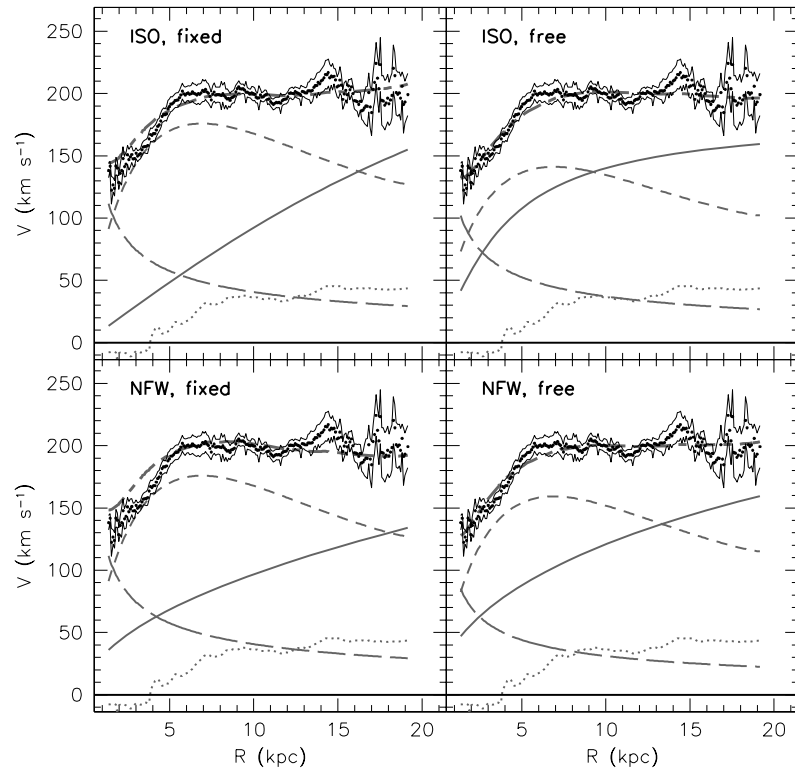


Figure 50. ISO and NFW rotation curve fits for NGC 6946. Lines and symbols are as in Figure 26.

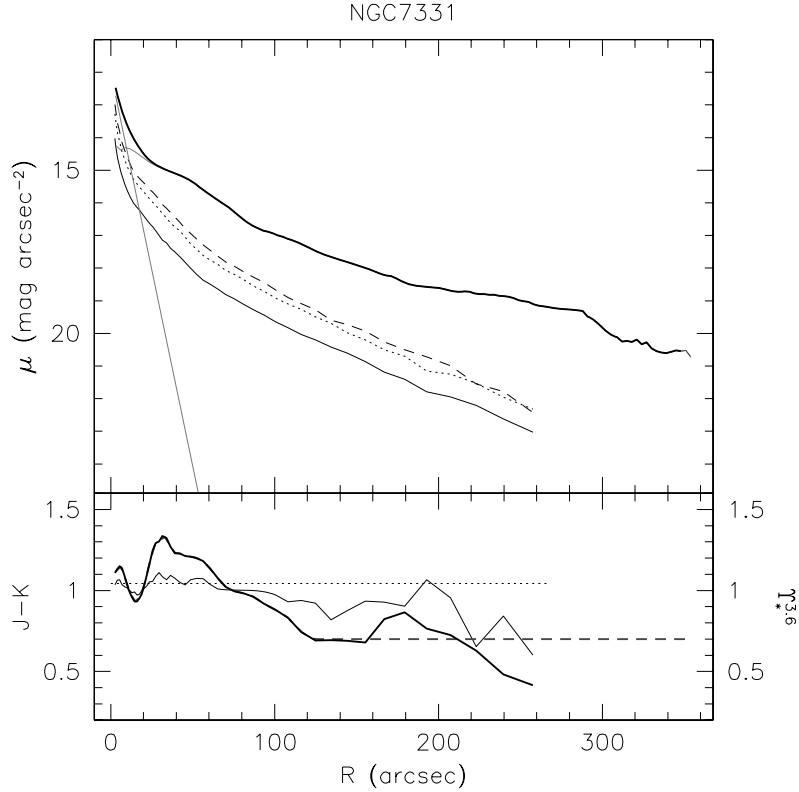


Figure 51. Surface brightness and $\gamma_*^{3.6}$ profiles for NGC 7331. Lines and symbols are as in Figure 24.

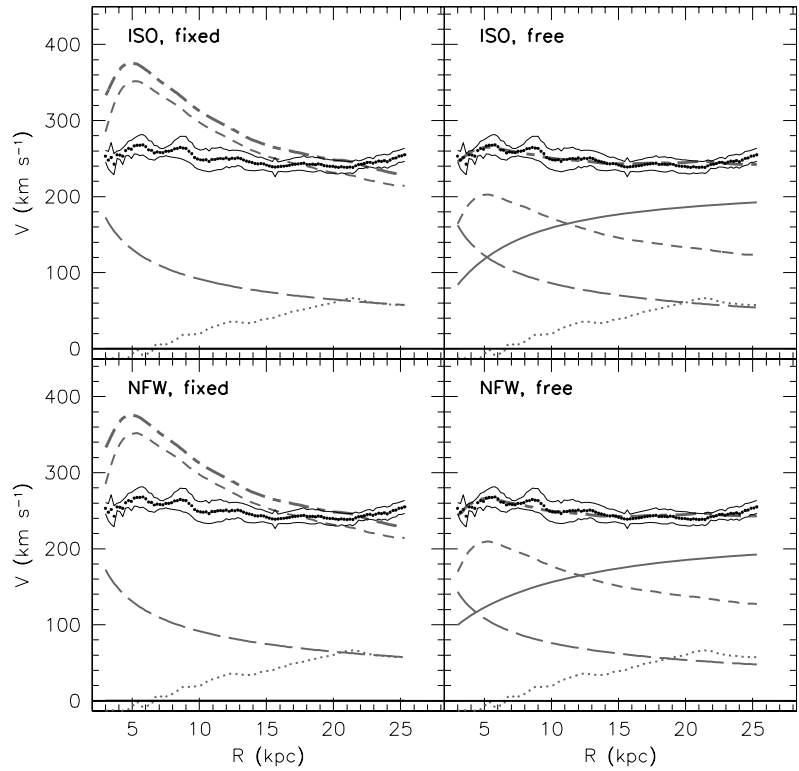


Figure 52. ISO and NFW rotation curve fits for the color-gradient model of NGC 7331. Lines and symbols are as in Figure 26.

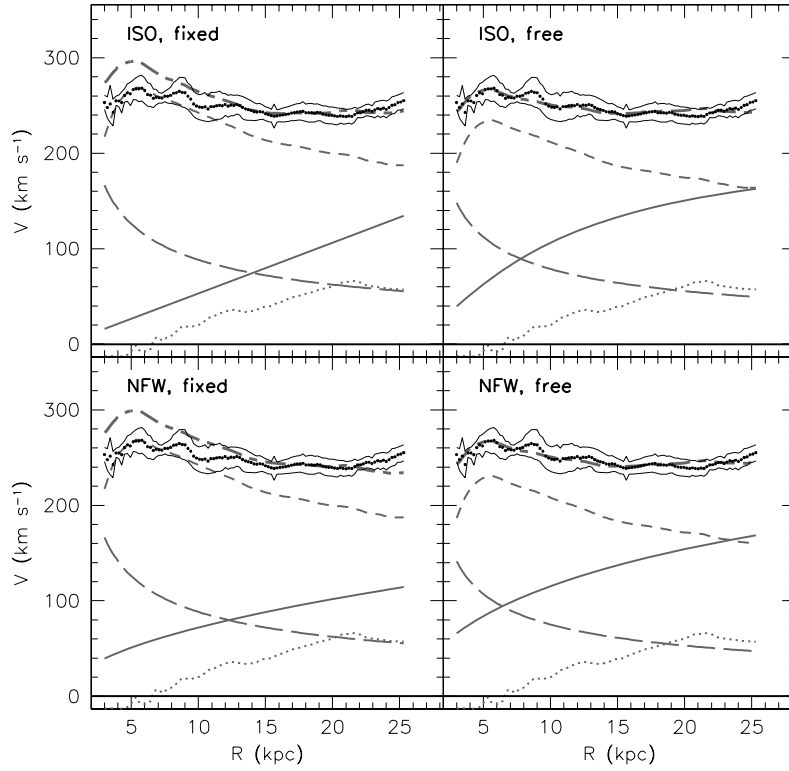


Figure 53. ISO and NFW rotation curve fits for the constant $\Upsilon_*^{3.6}$ model of NGC 7331. Lines and symbols are as in Figure 26.

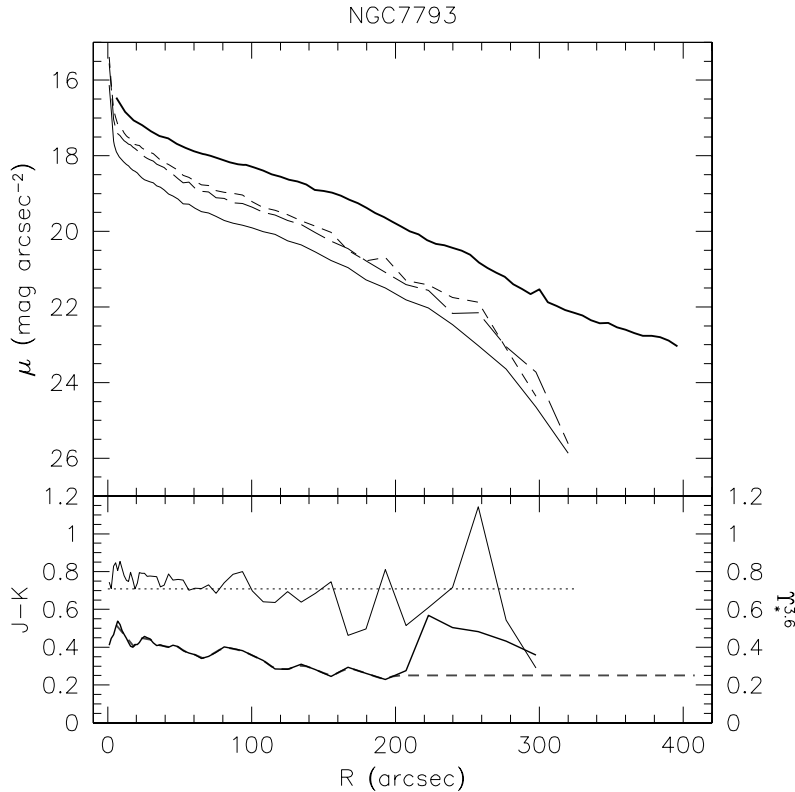


Figure 54. Surface brightness and $\Upsilon_*^{3.6}$ profiles for NGC 7793. Lines and symbols are as in Figure 24.

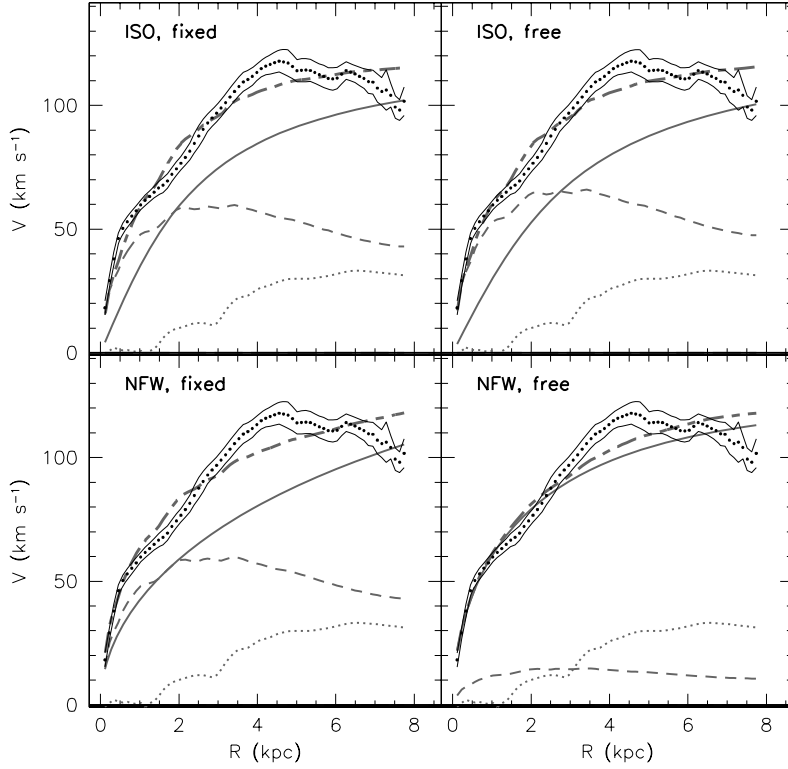


Figure 55. ISO and NFW rotation curve fits for NGC 7793 using the entire observed extent. Lines and symbols are as in Figure 25.

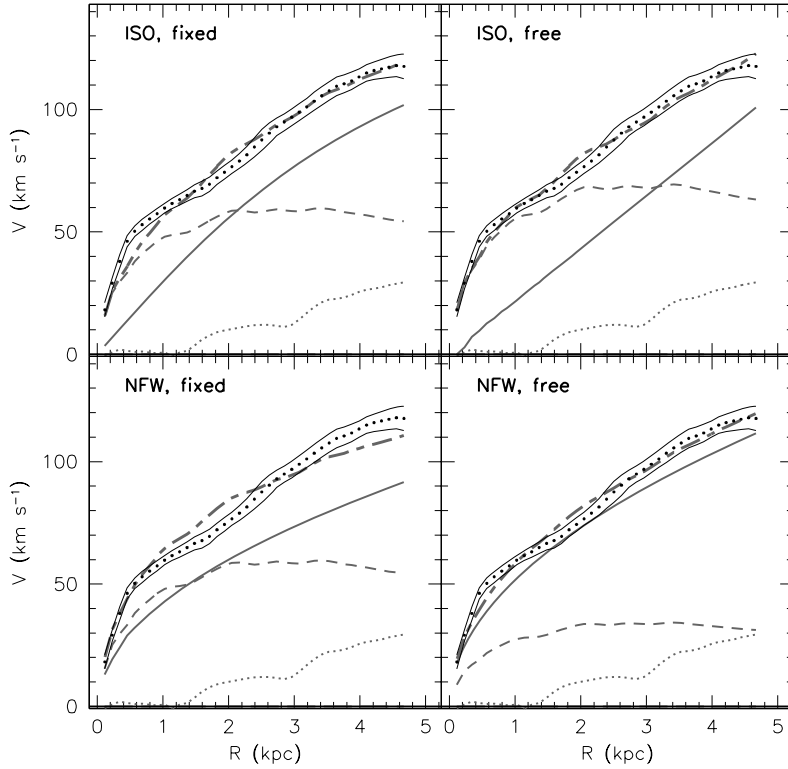


Figure 56. ISO and NFW rotation curve fits for NGC 7793 using only radii $R < 4.7$ kpc. Lines and symbols are as in Figure 25.

overpredicts the velocity in the inner parts. Note the very large values for $\Upsilon_{\star}^{3.6}$ when it is left as a free parameter. These will be discussed in more detail in Section 7. Because of the dark matter dominance in DDO 154, the derived halo parameters are virtually independent from the assumed IMF.

6.12. NGC 5055

The surface brightness profiles of NGC 5055 are shown in Figure 47. The 2MASS J , H , and K profiles can be traced out to $\sim 350''$, and the $3.6 \mu\text{m}$ profile out to $450''$. There is clear evidence for a compact central component which we model as an exponential disk with parameters $\mu_0 = 13.4 \text{ mag arcsec}^{-2}$ and $h = 0.35 \text{ kpc}$. For the outer disk, we simply used the observed profile with the inner component subtracted, as indicated in Figure 47. Small residuals are present, notably around $R \sim 50''$, but these are of minor importance. An exponential disk fit to radii $350'' < R < 450''$ was used to extend the outer disk profile. NGC 5055 has a significantly redder center, with a well-defined color gradient at larger radii. For the central component we assume a constant $\Upsilon_{\star}^{3.6} = 1.3$, whereas for the outer disk we find values from an inner $\Upsilon_{\star}^{3.6} \simeq 1$ to an outer $\Upsilon_{\star}^{3.6} \sim 0.5$. Beyond the radii where the 2MASS colors could be reliably determined, we assume a constant value of $\Upsilon_{\star}^{3.6} = 0.5$. In the very inner parts, we assumed an extrapolated $\Upsilon_{\star}^{3.6} = 1.0$ for the outer disk.

The rotation curve fits are presented in Figure 48. In the case of fixed $\Upsilon_{\star}^{3.6}$ the inner disk overpredicts the curve by a large factor (not shown here), and we kept it as a free parameter, yielding values of $\Upsilon_{\star}^{3.6} \sim 0.2$ for the inner disk. The NFW model seems to have particular difficulties fitting this galaxy. With $\Upsilon_{\star}^{3.6}$ as a free parameter, the fit demands a negative value for the outer disk. In the fits presented here, we have therefore set $\Upsilon_{\star}^{3.6} = 0$ for this component.

6.13. NGC 6946

The surface brightness profiles of NGC 6946 are shown in Figure 49. The 2MASS J , H , and K profiles as well as the $3.6 \mu\text{m}$ profile can all be traced out to $\sim 360''$. The profiles show clear evidence for a compact central component. We modeled this component as an exponential disk with parameters $\mu_0 = 12.8 \text{ mag arcsec}^{-2}$ and $h = 0.15 \text{ kpc}$. For the outer disk we used the observed profile with the inner component subtracted. For larger radii we extended the profile with an exponential fit with parameters $\mu_0 = 16.3 \text{ mag arcsec}^{-2}$ and $h = 2.97 \text{ kpc}$. There is evidence for a slight excess of light in the “shoulder” of the profile at $R \sim 50''$. This small excess does, however, have negligible effect on the results of the rotation curve fit, and we therefore use a two-component model for the stellar disk.

The outer disk of NGC 6946 shows no strong evidence for a $(J - K)$ color gradient and we use a constant $\Upsilon_{\star}^{3.6} = 0.64$. Within $R \sim 30''$, the change in color is, however, very pronounced, resulting in very red central components [$(J - K) > 1.4$ at the innermost point]. Taking these colors at face value would imply $\Upsilon_{\star}^{3.6} > 2.0$. Such colors are only found for extreme star formation histories (see Oh et al. 2008), and it is therefore likely that other effects contribute to this extreme color. For the purposes of the rotation curve analysis we therefore assume $\Upsilon_{\star}^{3.6} = 1.0$ for the inner disk (which is also the value one gets when averaging over the entire radial extent of the stellar component).

The halo model fits are presented in Figure 50. They show that the inner disk component prefers a value for $\Upsilon_{\star}^{3.6}$ that is

lower than the $(J - K)$ color would suggest. The values derived for the outer disk are reasonably close to the predicted values. The NFW and ISO models all produce very similar quality fits.

6.14. NGC 7331

The surface brightness profiles of NGC 7331 are shown in Figure 51. The 2MASS J , H , and K profiles can be traced out to $\sim 265''$; the $3.6 \mu\text{m}$ profile can be traced out to $350''$, or the entire extent of the H α disk. The profiles show clear evidence for a compact central component. We modeled this component as an exponential disk with parameters $\mu_0 = 12.0 \text{ mag arcsec}^{-2}$ and $h = 0.32 \text{ kpc}$. For the outer disk we simply used the observed profile with the inner component subtracted, as indicated in Figure 51. NGC 7331 has a well-defined color gradient, and shows some of the largest $\Upsilon_{\star}^{3.6}$ values, as well as one of the steepest $\Upsilon_{\star}^{3.6}$ gradients in the entire sample. Beyond the radii where the 2MASS colors could be reliably determined, we assume a constant value of $\Upsilon_{\star}^{3.6} = 0.7$.

These high $\Upsilon_{\star}^{3.6}$ values lead to incompatible mass models: using the predicted $\Upsilon_{\star}^{3.6}$ values results in disks that are too massive. This is shown in Figure 52, clearly suggesting that for this galaxy, the color-based values are not correct (for that reason we do not list the model parameters in Tables 3–6). Leaving $\Upsilon_{\star}^{3.6}$ free in the fit, the data clearly prefer lower values. A possible explanation could be the presence of a strong dust ring in the inner disk of NGC 7331 (Regan et al. 2004). The radius at which this ring is found corresponds to the radius where the highest $\Upsilon_{\star}^{3.6}$ values are found. This would suggest that the very inner $\Upsilon_{\star}^{3.6}$ maximum and steep drop are associated with the central component, whereas the subsequent steep rise and gradual drop are associated with the dust ring, and therefore do not reflect stellar population changes.

We therefore also investigate a model where the two components each have a radially constant $\Upsilon_{\star}^{3.6}$. Using Figure 51, we find that $\Upsilon_{\star}^{3.6} = 1.0$ and $\Upsilon_{\star}^{3.6} = 0.7$ are good estimates for the inner and outer disks, respectively. These fits are presented in Figure 53. We then find that both ISO and NFW models result in better fits. NGC 7331 is therefore the one galaxy in our sample where the $(J - K)$ - $\Upsilon_{\star}^{3.6}$ relation clearly fails. Note that for the fixed $\Upsilon_{\star}^{3.6}$ case, the Kroupa models yield much better fits than the diet Salpeter ones.

6.15. NGC 7793

The surface brightness profiles of NGC 7793 are shown in Figure 54. The 2MASS J , H , and K profiles can be traced out to $\sim 325''$; the $3.6 \mu\text{m}$ profile can be traced out to $400''$ —the entire extent of the H α disk. The 2MASS profiles show a clear and sudden increase in surface brightness in the very inner part. This is the signature of the nuclear star cluster in NGC 7793 (Böker et al. 2002). Its photometric and dynamical importance has already become negligible at the radius of the innermost point of the rotation curve. The extent of the IRAC $3.6 \mu\text{m}$ profile equals that of the H α data, and no exponential extrapolations were necessary. The $(J - K)$ profile shows a small but consistent color gradient, translating in a gradient in $\Upsilon_{\star}^{3.6}$ from ~ 0.5 in the inner parts, to ~ 0.25 at the outermost radius where the 2MASS colors were deemed reliable. Beyond this radius, we assume a constant $\Upsilon_{\star}^{3.6} = 0.25$ as indicated in Figure 54.

The rotation curve mass models are presented in Figure 55. For the fixed $\Upsilon_{\star}^{3.6}$ model both ISO and NFW models give roughly equal results: neither is fully able to describe the observed

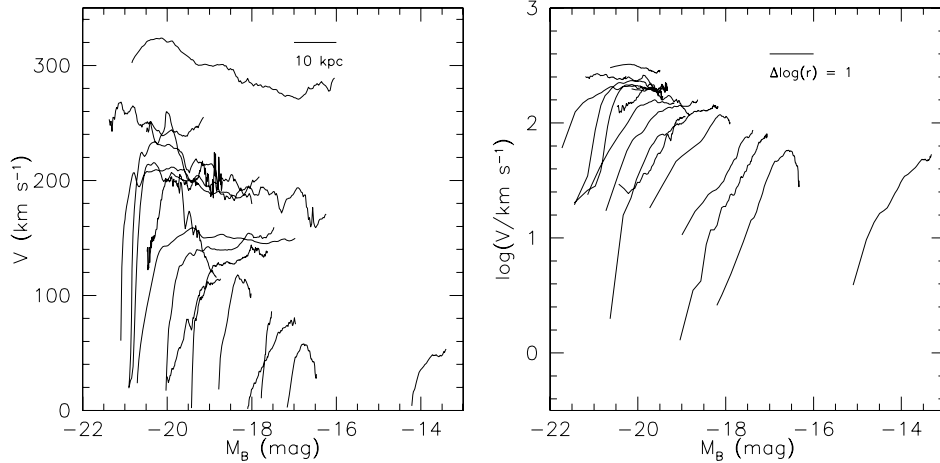


Figure 57. All THINGS rotation curves plotted in linear units in the left panel and in logarithmic units in the right panel. The origin of the rotation curves has been shifted according to their absolute luminosity as indicated on the horizontal axis. The bar in the respective panels indicates the radial scale.

rotation curve (independent of IMF). The “bump” in the rotation curve within $R = 2$ kpc and its resemblance with the shape of the stellar disk rotation curve suggest that the inner part of NGC 7793 could be close to a maximum disk. The ISO model with $\Upsilon_*^{3.6}$ as a free parameter does indeed prefer $\Upsilon_*^{3.6}$ values that are slightly higher than the fixed $\Upsilon_*^{3.6}$ diet Salpeter value. For the NFW model, releasing $\Upsilon_*^{3.6}$ has forced its value down to unrealistic values in order to accommodate the more concentrated dark halo.

As remarked earlier (in Section 4.17), the possible observed decline in the outer rotation curve is uncertain. We tested whether this decline could cause the low quality of the fits by repeating the analysis with radii $R > 4.7$ kpc excluded. This analysis is shown in Figure 56. For the fixed $\Upsilon_*^{3.6}$ case the situation does not change much. The biggest improvement is achieved for the ISO model with a free $\Upsilon_*^{3.6}$. The preferred value is close to a maximum disk, with a significantly better overall fit.

7. DISCUSSION

We now put the results derived for individual galaxies in a broader context by looking at the sample as a whole. Section 7.1 deals with some of the general properties of the rotation curves and looks at correlations with luminosity as well as the mass fractions within the galaxies. Section 7.2 deals with the values for $\Upsilon_*^{3.6}$ and compares them with other measures for the stellar mass-to-light ratio. Sections 7.3 and 7.4 deal with the halo properties. In Section 7.3 we discuss the halo rotation curves, and in Section 7.4 the parameters of the halo models are compared with predictions based on cosmological models.

7.1. General Properties

THINGS contains galaxies spanning a large range of luminosities and Hubble types. Consequently, there is a large range in shape, amplitude, and extent of the rotation curves within our sample. To illustrate this diversity, in Figure 57 we plot all derived rotation curves on the same physical scale, with the position of the origin of the rotation curve offset using the absolute magnitude M_B of the galaxy. The well-known change in properties of the rotation curves with luminosity (cf., Broeils 1992) is readily apparent. Luminous galaxies have rotation curves that rise steeply, followed by a decline and

an asymptotic approach to the flat outer part of the curve; low-luminosity galaxies show a more gradual increase, never quite reaching the flat part of the curve over the extent of their H I disks.

This is shown more clearly in the right-hand panel in Figure 57 where we plot the logarithmic rotation curves, $\log(V)$ versus $\log(R)$. Once again the starting point of the rotation curve is determined by the absolute luminosity. The change in slope as a function of luminosity can readily be made out.

Another well-known relation for disk galaxies, is that low-luminosity galaxies (late-type disk and dwarf galaxies) are more dominated by dark matter than luminous galaxies (early-type disk galaxies; e.g., Roberts & Haynes 1994). The flat rotation curves of spiral galaxies are additionally an indication that dark matter should become more and more dominant toward larger radii. We can explicitly evaluate these relations by deriving the ratio of the mass of the baryons and the mass of the dark matter halo at each radius as

$$\frac{M_{\text{baryons}}}{M_{\text{tot}}} = \frac{V_{\text{gas}}^2 + \Upsilon_* V_*^2}{V_{\text{obs}}^2}, \quad (11)$$

where $M_{\text{baryons}}/M_{\text{tot}}$ is an indication for the degree of dark matter dominance, V_{obs} is the observed rotation curve, V_{gas} the rotation curve of the gas component as described in Section 5.1, and $\sqrt{\Upsilon_*} V_*$ is the rotation velocity of the stellar component (taken to be the quadratic sum of multiple stellar components if present).

Note that for some of the galaxies discussed in Section 6, we derived multiple mass models with, e.g., single or multiple stellar components. In the rest of the paper, we will restrict ourselves to one model per galaxy so as not to needlessly confuse the discussion. For NGC 2403 and NGC 3198 we use the two-component model, for NGC 7793 we use the model that uses the entire rotation curve, and for NGC 7331 we use the model without the color gradient. These particular choices do not affect any of our conclusions.

The top panel of Figure 58 shows the radial dependence of $M_{\text{baryons}}/M_{\text{tot}}$ for our sample galaxies, assuming values for $\Upsilon_*^{3.6}$ as predicted from the photometry. These distributions are for all practical purposes independent of the choice of IMF. The largest variation in $M_{\text{baryons}}/M_{\text{tot}}$ is about 0.1 dex (a factor of 1.3)

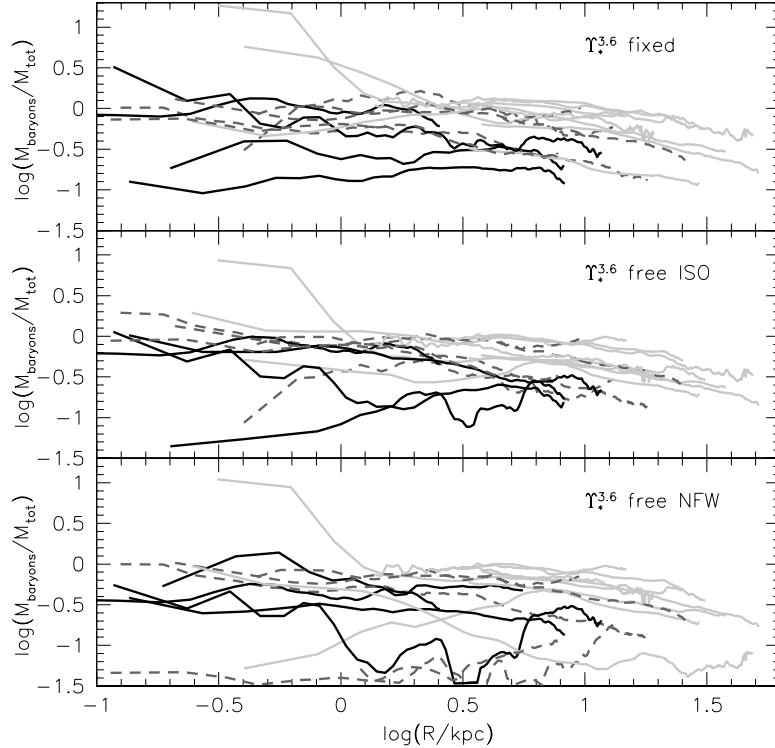


Figure 58. The radial distribution of $M_{\text{baryons}}/M_{\text{tot}}$ in the THINGS galaxies for several assumptions on $\gamma_*^{3.6}$. The top panel shows the distribution assuming the fixed, predicted diet Salpeter $\gamma_*^{3.6}$ values. The center and bottom panels show the distributions assuming the best-fitting $\gamma_*^{3.6}$ values determined by using the ISO and NFW models. Light-gray full curves represent galaxies brighter than $M_B = -20.5$. Dashed dark-gray curves show galaxies with $-20.5 \leq M_B < -18.5$. Black curves show galaxies fainter than $M_B = -18.5$.

in the very inner parts of the luminous galaxies and quickly becomes totally negligible toward lower luminosities and large radii.

There are a few things to note in Figure 58. First, galaxies with the highest absolute luminosity are, in general, the least dominated by dark matter. This is true not only globally but also locally: even at the outermost radii, the baryons in these luminous galaxies are more dominant than in the least luminous galaxies. Second, while the most luminous galaxies show a clear gradient in $M_{\text{baryons}}/M_{\text{tot}}$ with radius (with the outer radii becoming progressively more dark-matter-dominated), this trend is less pronounced in the low-luminosity galaxies. The latter indeed are dominated by dark matter at all radii. These results are robust against any particular choice of dark matter model, but only depend on the values of $\gamma_*^{3.6}$.

It is also interesting to explore the distribution of $M_{\text{baryons}}/M_{\text{tot}}$ for the case of $\gamma_*^{3.6}$ as a free parameter (i.e., as determined by the dynamics, rather than the photometry). In these cases the results are not entirely independent of the halo model assumed, as the choice of model plays a role in determining $\gamma_*^{3.6}$ during the fitting. The middle and bottom panels of Figure 58 show $M_{\text{baryons}}/M_{\text{tot}}$ for the best-fitting ISO and NFW $\gamma_*^{3.6}$ values, respectively. The trends discussed above are still present in the fixed $\gamma_*^{3.6}$ ISO case, but they become confused for the NFW model. The latter is most likely a reflection of the NFW model being an inappropriate fitting function for at least some of the galaxies.

7.2. Stellar Mass-to-Light Ratio Trends

An overview of the derived $\gamma_*^{3.6}$ values of the main disk components of our sample galaxies is given in Figure 59. Here

we plot the photometric (fixed) and dynamical (free) values for $\gamma_*^{3.6}$ against the colors and luminosities of the galaxies. The left-hand panels show the fixed and free $\gamma_*^{3.6}$ values of the disks for both the ISO and NFW model plotted against $(J - K)$ color. We also distinguish between our two choices for the IMF. Also shown is the predicted relation between $\gamma_*^{3.6}$ and color (Equations (4) and (5)), again for both the diet Salpeter and the Kroupa IMFs. By definition, the photometric $\gamma_*^{3.6}$ values follow their respective relations. The small scatter is caused by the color gradients present in these galaxies which make the photometric $\gamma_*^{3.6}$ differ slightly from those with a constant $\gamma_*^{3.6}$ as a function of radius.

In general, we see that the diet Salpeter curve defines an approximate upper limit to the distribution of the majority of the best fit values (apart from a few obviously discrepant cases). Accepting the best fit (free) $\gamma_*^{3.6}$ values at face value, this would suggest that a diet Salpeter $\gamma_*^{3.6}$ analysis overestimates the disk masses slightly. Indeed, the Kroupa fixed $\gamma_*^{3.6}$ values seem to be a better match to the free $\gamma_*^{3.6}$ values. Alternative explanations could be effects of star formation history, or unexpectedly large contamination by PAHs, AGBs or hot dust in the $3.6 \mu\text{m}$ maps, though it is likely that the IMF plays the dominant role. Future rigorous population synthesis modeling should shed light on some of these issues. The NFW $\gamma_*^{3.6}$ values tend to be lower than the ISO values, which is to be expected due to the intrinsically steeper mass distribution of the NFW halo.

We compare the distributions of the $\gamma_*^{3.6}$ values in Figure 60. The diet Salpeter fixed $\gamma_*^{3.6}$ values are offset toward somewhat higher values compared with the ISO free $\gamma_*^{3.6}$ distribution. The Kroupa fixed $\gamma_*^{3.6}$ values are a much better match, as already

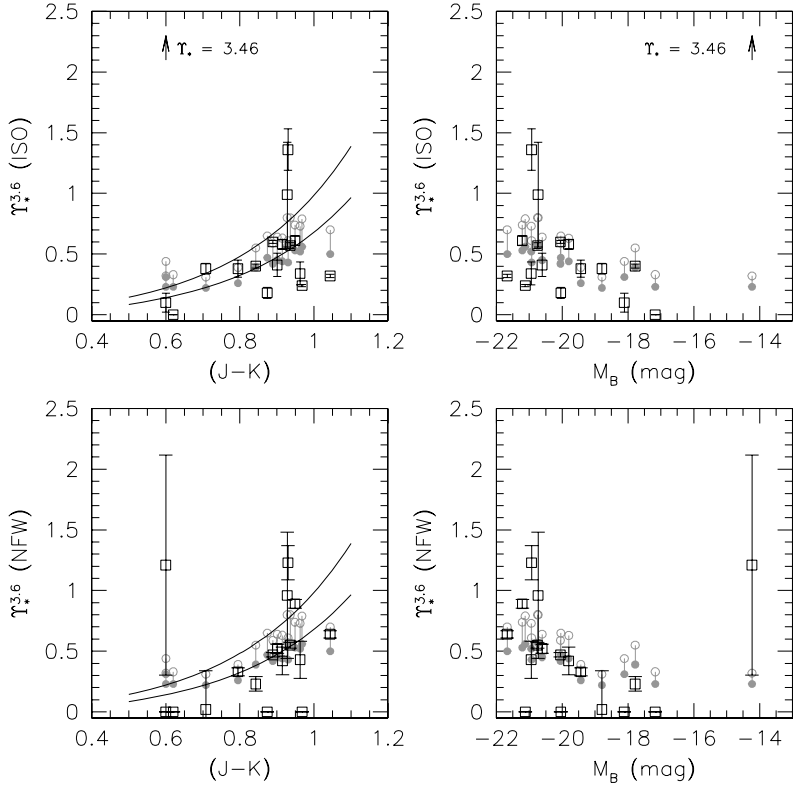


Figure 59. $\Upsilon_*^{3.6}$ plotted against color and luminosity. Results are shown as a function of color ($J - K$) in the left-hand column, as a function of absolute magnitude M_B in the right-hand column. The top row shows results derived for the ISO halo, the bottom row those for the NFW halo. Open squares indicate the results derived for the free (dynamical) $\Upsilon_*^{3.6}$ fits, the connected gray symbols show the fixed (photometric) $\Upsilon_*^{3.6}$ values. The upper symbols (open gray circles) indicate the results for a diet Salpeter IMF, the lower symbols (filled gray circles) indicate the results for a Kroupa IMF. In the left-hand panels the curves show the theoretical color- $\Upsilon_*^{3.6}$ relations as derived from Equations (4) and (5). The upper curve assumes a diet Salpeter IMF and the lower curve assumes a Kroupa IMF. In the top row the arrows indicate the high free $\Upsilon_*^{3.6}$ value derived for DDO 154.

suggested by Figure 59. The distribution for the NFW model is less well-defined, and has a larger number of galaxies at very low $\Upsilon_*^{3.6}$ values. These are the cases where $\Upsilon_*^{3.6}$ had to be set to zero manually, due to the preferred negative $\Upsilon_*^{3.6}$ values. The smaller spread of the $\Upsilon_*^{3.6}$ values for the ISO case, and the somewhat better agreement with the predicted values, especially for the Kroupa IMF results, could be taken as tentative supporting evidence that the ISO model is superior in describing the properties of real galaxies.

In general, it is remarkable that despite our empirical and, from the point of view of a population synthesis expert, undoubtedly rudimentary modeling of the stellar mass-to-light ratios, the best-fit dynamical $\Upsilon_*^{3.6}$ values lie so close to the photometric $\Upsilon_*^{3.6}$ values. The photometric $\Upsilon_*^{3.6}$ values “do not know” anything about dynamics, and the best-fitting dynamical values, whereas the best-fitting $\Upsilon_*^{3.6}$ ratios have no a priori reason to stay close to the predicted photometric stellar population values. It is therefore gratifying to see that the calculated $\Upsilon_*^{3.6}$ agree with the fitted $\Upsilon_*^{3.6}$ to such a good degree.

Plotting $\Upsilon_*^{3.6}$ against luminosity (the right-hand panels in Figure 59) we see that the brightest galaxies have the highest $\Upsilon_*^{3.6}$ ratios. These large values are not found for the lower-luminosity galaxies.

The one galaxy that shows a different behavior is DDO 154. Its predicted population-synthesis $\Upsilon_*^{3.6}$ value is low, but the $\Upsilon_*^{3.6}$ values derived from the mass-modeling do not agree and are

much higher. This discrepancy can be due to neither the data quality (THINGS observed galaxies at identical resolution and sensitivity) nor large noncircular motions, because DDO 154 has a well-behaved, “quiescent” velocity field (Trachternach et al. 2008).

One can interpret this result at face value, and assume that DDO 154 does have a massive disk. This would, however, put it out of odds with the rest of the sample, and imply a substantial change in the nature of galaxy disks toward low luminosities. An alternative explanation could be that for galaxies like DDO 154 the disk is not massive enough to have a noticeable effect on the total rotation curve. There would then be no small deviations induced by, e.g., spiral arms, and the dynamics are everywhere dominated by the dark matter. The fitting program is then unable to derive a sensible value for $\Upsilon_*^{3.6}$. Obviously, a larger sample of high-resolution observations of galaxies fainter than $M_B \sim -17$ should then show the same trend. A similar, but slightly more prosaic, explanation is related to the fact that DDO 154 has the lowest surface brightness disk in 3.6 μm in our sample. The surface brightness profile is measured out to only $\sim 100''$ (~ 2 kpc), while the rotation curve extends out to $\sim 400''$ (~ 8 kpc). This means that most of the disk rotation curve is based on a smooth exponential extrapolation of the observed surface brightness profile. If the underlying (undetected) disk does indeed induce small wiggles in the observed rotation curve, then these will not be matched by the disk rotation curve (as derived from the exponential extrapolation), and this will throw

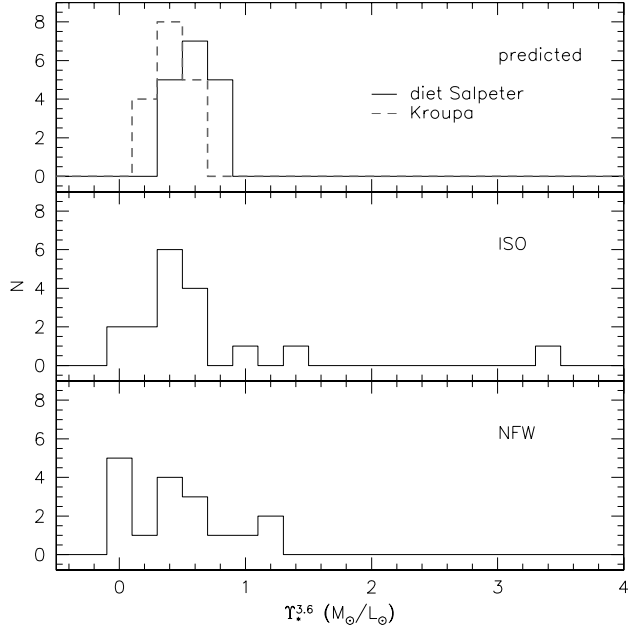


Figure 60. Histograms of the various $\Upsilon_{\star}^{3.6}$ values. Top: predicted values: full histogram assumes a diet Salpeter IMF; dashed histogram assumes a Kroupa IMF. Center: best-fit values assuming the ISO halo model. Bottom: best-fit values assuming the NFW model.

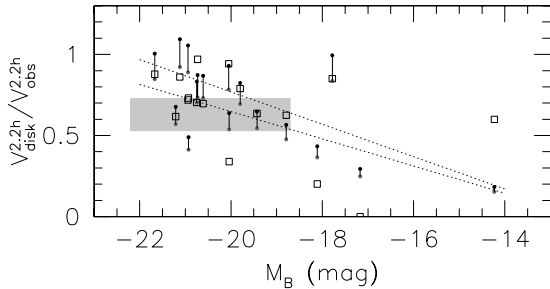


Figure 61. Ratio of the inferred maximum rotation velocity of the disk and the total rotation velocity occurring at that radius, plotted against absolute luminosity. Open squares show the ratios assuming the free (dynamical) $\Upsilon_{\star}^{3.6}$ values. The connected symbols show those derived for the fixed (photometric) $\Upsilon_{\star}^{3.6}$ values. The upper symbols (filled black circles) show the results for a diet Salpeter IMF, the lower (filled gray circles) show those for a Kroupa IMF. The gray box indicates the range in luminosity and velocity ratios derived by Bottema (1997) on the basis of stellar velocity dispersion measurements. The dotted line represents a least-squares fit assuming the predicted $\Upsilon_{\star}^{3.6}$ values. The upper line is derived for the diet Salpeter IMF and decreases as $\sim 0.25 \log L_B$. The lower line assumes a Kroupa IMF and decreases as $\sim 0.20 \log L_B$. These slopes are, however, to a large extent determined by the DDO 154 result at $M_B \sim -14$.

the fitting program off track. Tests of replacing the observed disk rotation curves of a few of the other THINGS galaxies with their smooth exponential disk equivalents indicate that this does indeed affect the derived $\Upsilon_{\star}^{3.6}$ values, but the effects are not unambiguous enough to conclusively show that this is the single cause of what is happening in the DDO 154 mass modeling. Deeper observations of the stellar disk should help pinpoint the exact cause of the $\Upsilon_{\star}^{3.6}$ discrepancy.

Finally, in Figure 61 we show the dynamical importance of the stellar disk as a function of luminosity. We plot the ratio of the maximum rotation velocity of the disk (assuming the photometric $\Upsilon_{\star}^{3.6}$ ratios and using both IMF assumptions) and the total rotation velocity at the radius where the maximum

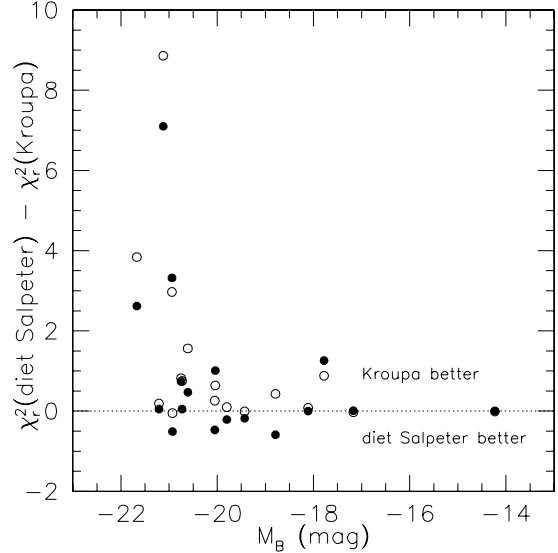


Figure 62. Comparison of the quality of the models under various assumptions for IMF and dark matter halo models. The open circles show the difference in goodness-of-fit between a diet Salpeter $\Upsilon_{\star}^{3.6}$ model and a Kroupa $\Upsilon_{\star}^{3.6}$ model assuming an NFW halo. The filled circles show the same for the ISO model.

disk velocity occurs ($2.2h$ for an exponential disk). It is clear that disks become dynamically less and less important with decreasing luminosity. Note that a similar plot of the importance of the disk versus luminosity for the case of free $\Upsilon_{\star}^{3.6}$ (also shown in Figure 61) does not show such a trend as clearly, but here the result may be diluted by the effects just described.

In a previous analysis, Bottema (1997) used measurements of stellar velocity dispersions in a number of early-type disk galaxies to estimate the dynamical contribution of the disk. He found for the magnitude range he investigated ($-22 \lesssim M_B \lesssim -19$) that the ratio of maximum rotation velocity of the stellar disk and total rotation velocity at the corresponding radius (generally $2.2h$) is $V_{\text{disk}}^{2.2h} / V_{\text{obs}}^{2.2h} = 0.63 \pm 0.10$. These results are also indicated in Figure 61.

Over the same range in magnitude we find that $V_{\text{disk}}^{2.2h} / V_{\text{obs}}^{2.2h} = 0.81 \pm 0.19$ for the fixed diet Salpeter $\Upsilon_{\star}^{3.6}$ case and $V_{\text{disk}}^{2.2h} / V_{\text{obs}}^{2.2h} = 0.68 \pm 0.16$ for the Kroupa IMF fits. The latter is in reasonable agreement with the Bottema (1997) values. The free $\Upsilon_{\star}^{3.6}$ results yield $V_{\text{disk}}^{2.2h} / V_{\text{obs}}^{2.2h} = 0.73 \pm 0.17$.

In order to gauge whether our data show a preference for one particular IMF, in Figure 62 we compare the goodness-of-fit values for the fixed $\Upsilon_{\star}^{3.6}$ models (for both the diet Salpeter and Kroupa IMFs) and the ISO and NFW halos as a function of luminosity. Several conclusions can be drawn from this comparison. First, the choice of IMF does not influence the goodness of fit for low-luminosity galaxies. This is, of course, to be expected as the dynamics of these galaxies are dominated by the dark matter component. Second, for the intermediate luminosity galaxies, the ISO models prefer a diet Salpeter IMF, while the NFW models prefer a Kroupa IMF. This is also easily understood, as the NFW halo has a steeper mass-density profile (a steeper inner rotation curve) which leaves less room for the luminous component and results in lower optimal $\Upsilon_{\star}^{3.6}$ values. Third, for the high-luminosity galaxies, the Kroupa IMF is much preferred over the diet Salpeter fits. This reflects the fact that the diet Salpeter fits result in disks that are close to the maximum allowed by the dynamics. A small change in the $\Upsilon_{\star}^{3.6}$

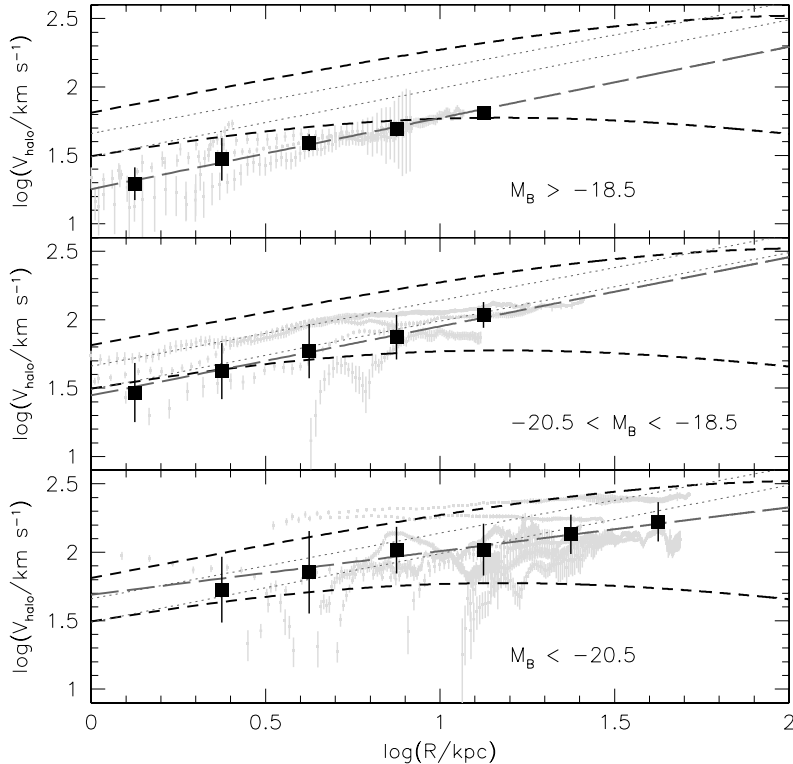


Figure 63. Halo rotation curves of the THINGS galaxies. The galaxies are binned according to their luminosities, as indicated in the figure. Individual halo rotation curve points derived assuming fixed $\Upsilon_*^{3.6}$ values are shown as the small light gray points. The average velocity values binned every 0.25 dex in radius are shown as the large black squares. The thick long-dashed dark gray line shows the best power-law fit to those points. The thick black dashed curves indicate the minimum and maximum rotation velocities one expects to find for NFW halos at each radius. The lower curve has parameters $(c, V_{200}) = (9.5, 50 \text{ km s}^{-1})$. The upper curve has $(c, V_{200}) = (6.7, 300 \text{ km s}^{-1})$. All realistic and CDM-consistent NFW halos are expected to fall between these two curves. The lower of the two thin dotted lines indicates the best power-law fit to the empirical halo rotation curves derived in McGaugh et al. (2007). The upper one shows their best power-law fit to a comparable sample of NFW halos. These curves assume a diet Salpeter IMF; results for the Kroupa IMF are very similar; see the text for a more extensive description.

value can then result in a large difference in the quality of the fit. The Kroupa IMF with its lower $\Upsilon_*^{3.6}$ values is more stable against these effects, as it still allows a dark matter component in the inner parts which can compensate for any small $\Upsilon_*^{3.6}$ uncertainties.

The photometrically determined, fixed $\Upsilon_*^{3.6}$ values therefore do not allow us to choose a particular IMF, without making additional assumptions on the distribution of the dark matter. It would thus be interesting to independently confirm the Υ_* values of the disks with measurements of the stellar velocity dispersions within the THINGS disks, and thus calibrate our Υ_* measurements.

7.3. Halo Rotation Curves

In Section 7.1 we used the derived $\Upsilon_*^{3.6}$ values in combination with our rotation curves to derive the ratio of baryonic total mass as a function of radius. In a similar way, we can derive the rotation curves of the dark matter halos:

$$V_{\text{halo}}^2 = V_{\text{obs}}^2 - V_{\text{gas}}^2 - \Upsilon_* V_*^2, \quad (12)$$

where again we are, strictly speaking, dealing with the circular rotation velocities of test particles in the plane of the galaxy. The velocities of the gas and stars have been calculated using the three-dimensional mass distributions as described in Section 5.1 and 5.2. We again assume spherical halos.

McGaugh et al. (2007) show that these empirical halo rotation curves, for a realistic range of Υ_* values, yield halo dark

matter densities about $\sim 50\%$ lower than expected from Λ CDM simulations. One interesting aspect of their conclusions is that they are based on the outer ($R > 1$ kpc) parts of the rotation curves, i.e., those regions where the usual concerns about resolution or slope of the curve are not relevant.

Here we repeat the analysis of McGaugh et al. (2007) for our current sample. We derive the halo rotation curves for our galaxies assuming the photometric (fixed) $\Upsilon_*^{3.6}$ values for both IMF assumptions. The resulting diet Salpeter IMF logarithmic halo rotation curves are shown in Figure 63, where we have divided the galaxies into three bins according to their luminosity. The Kroupa IMF halo rotation curves are very similar and we will not show them here, though we do discuss their implications below.

For each luminosity bin, we show the original data as well as the observed average halo rotation velocity binned in steps of 0.25 dex in radius. Following McGaugh et al. (2007), we only consider radii $R > 1$ kpc, so as not to confuse the issue with potential systematic effects in the determination of the very inner slope. Over the radial range observed, the average velocities behave very nearly like a power-law. Also shown in Figure 63 are two NFW model rotation curves with V_{200} velocity values chosen so they encompass the observed data set. The lowest velocity model has $V_{200} = 50 \text{ km s}^{-1}$, and is representative of the dwarf galaxies in our sample. On the high-luminosity end of the range, we show a model with $V_{200} = 300 \text{ km s}^{-1}$. Galaxies with intermediate luminosities or masses will have curves lying between these two extremes. The corresponding c -parameters

of these curves have been chosen to be consistent with current Λ CDM cosmological models (see Sections 5.3.1 and 7.4.2).

In Figure 63 we also show the fit to the halo rotation velocities derived for the ~ 60 galaxies in the McGaugh et al. (2007) sample, assuming their photometrically derived Υ_* ratios. They find that over the radial range observed, the halo rotation velocity can best be described by $\log V = 0.50 \log R + 1.49$. To compare this with CDM predictions, McGaugh et al. (2007) subjected a large number of NFW halo models to observational selection effects and found that the average halo rotation velocity in a Λ CDM universe is best described as $\log V = 0.48 \log R + 1.66$ (also shown in Figure 63). From this, they conclude that the empirically determined densities of dark matter halos are $\sim 50\%$ lower than those predicted by CDM simulations.

We first consider the lowest luminosity bin with $M_B > -18.5$. Over the observed radial range the average diet Salpeter halo velocities can be described by a power-law $\log V = 0.52 \log R + 1.25$ (Kroupa: $\log V = 0.41 \log R + 1.35$). The normalization is thus 0.24 (0.15) dex (a factor 1.7 to 1.4) lower than the empirical one derived by McGaugh et al. (2007) and 0.41 (0.31; a factor of 2.5–2.0) dex lower than the average velocity for CDM halos as derived in that paper. The latter value was, however, derived for a much larger range in mass than considered in this low-luminosity subsample. Nevertheless, even if we compare this with the value found at 1 kpc for a $V_{200} = 50 \text{ km s}^{-1}$ halo (which should be more typical for the galaxies considered here; see Figure 63), we still find a velocity that is 0.25 (0.15) dex lower than predicted. Only at $R \sim 10$ kpc do we begin to find some agreement between the empirical and simulated velocities.

The situation is similar for the intermediate luminosity galaxies with $-20.5 < M_B < -18.5$. The average diet-Salpeter-derived halo velocity can be described as $\log V = 0.50 \log R + 1.45$ (Kroupa: $\log V = 0.47 \log R + 1.50$), virtually indistinguishable from the McGaugh et al. (2007) fit. The same conclusions thus hold here: the velocity normalization is about 0.21 (0.16) dex (a factor 1.6 to 1.4) too low compared with average CDM halos, or about 0.25 (0.20) dex (a factor 1.8 to 1.6) lower than that of a $V_{200} = 150 \text{ km s}^{-1}$ halo (which has a value $\log V \sim 1.7$ at $R = 1$ kpc). This difference in normalization is illustrated by the fact that in Figure 63 the inner three observed average data points overlap with those of the $V_{200} = 50 \text{ km s}^{-1}$ halo, even though the average maximum rotation velocity of the galaxies in this subsample is $\sim 130 \text{ km s}^{-1}$.

At the high-luminosity end of the sample, $M_B < -20.5$, all observed average data points are now within the range described by NFW halos, but there is still a normalization discrepancy for the diet Salpeter case. The data extend further out in radius and are best described by a power-law fit $\log V = 0.32 \log R + 1.69$ (Kroupa: $\log V = 0.27 \log R + 1.83$). The slope is thus more shallow than in the other luminosity bins, perhaps indicating we are starting to see the velocity turnover or flattening expected in the ISO and NFW models. If we look at halos with V_{200} values between 200 and 300 km s^{-1} , we find intercept values at $R = 1$ kpc between $\log V = 1.75$ and 1.80. This discrepancy is, therefore, less pronounced than for the lower-luminosity bins, but still amounts to ~ 0.1 dex, or a factor 1.3 difference, for the diet Salpeter case. For the Kroupa case, the intercepts agree, but note that the slope of the average halo rotation curve is much more shallow than the NFW model curves. The real rotation curves flatten much faster than NFW models with comparable mass.

For completeness, we note that the halo velocities of the entire THINGS rotation curve sample (assuming a diet Salpeter IMF) are best described as $\log V = 0.46 \log R + 1.49$, in good agreement with the McGaugh et al. (2007) result. For the Kroupa case we find $\log V = 0.45 \log R + 1.58$. The best-fit dynamical, free $\Upsilon_*^{3.6}$ values (as derived for the ISO model) give a fit $\log V = 0.50 \log R + 1.50$, indistinguishable from the fixed $\Upsilon_*^{3.6}$ diet Salpeter IMF result.

In summary, the empirically derived rotation velocities associated with dark matter halos of galaxies fainter than $M_B \sim -19$ are about 0.2 dex or ~ 1.6 times lower than predicted by CDM simulations, independent of IMF, with the largest discrepancies found in the lowest luminosity galaxies. The agreement with simulated CDM halos improves toward higher luminosities, but the degree of improvement strongly depends on the assumed IMF.

If we translate the 0.2 dex in difference in velocity to density differences, we find an average density that is ~ 40 –60% of the predicted values. These numbers do depend on the precise density distribution, but they suggest that dark matter halos of late-type galaxies have densities that are about half of those predicted by CDM. This may also hold true of the luminous galaxies in our sample, but here the results depend on the assumed IMF.

7.4. Mass Models and Model Parameters

7.4.1. Treatment of Uncertainties

In the preceding discussion we have analyzed the importance of dark matter in the THINGS galaxies without any strong assumptions on its actual distribution. However, rotation curves are most often used to test particular dark matter models, and, as described in Section 1, the debate in recent years has focused on the apparent inability of cosmological CDM simulations to describe the distribution of dark matter on the scale of galaxies. With the high resolution and excellent sensitivity of the THINGS velocity fields and rotation curves, we are now in a position to revisit some of the outstanding questions, and compare the applicability of both the observationally motivated ISO model and the cosmologically motivated NFW model (see Section 5.3).

Comparison of the fits derived here can tell us which of the dark matter models, if any, is preferred. Note that with the sampling of our velocity fields of two points per beam, the individual rotation curve data points are not entirely independent. This obviously affects the absolute χ^2 values, but with the non-Gaussian distribution of the uncertainties in the rotation curve data points, we will not dwell on an interpretation of the absolute χ^2 values. More importantly, our conservative estimates of the uncertainties, taking into account the dispersion of velocity values found along tilted rings, as well as the differences between approaching and receding sides (Section 3.6) will also affect the absolute χ^2 values. More relevant for our discussion are therefore the *differences* between the *reduced* χ^2 values, which tell us the relative merits of any particular model. In this respect, the χ^2 statistic should not be confused with the χ^2 test. The statistic simply quantifies the sum of the absolute differences between the observed velocities and the best-fitting model velocities, expressed in terms of the measurement uncertainties and normalized using the effective number of data points. This reduced χ^2 is here used only as a proxy for the average excess velocity per data point.

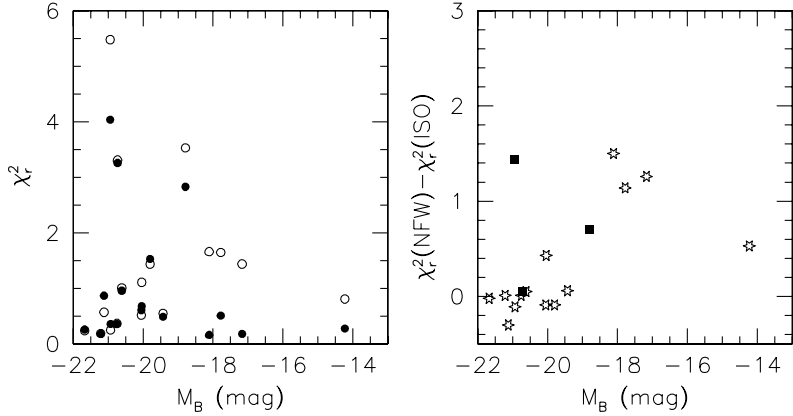


Figure 64. Left: Distribution of χ^2_r as a function of luminosity with $\Upsilon_*^{3.6}$ as a free parameter. Filled circles are ISO fits. Open circles are NFW fits. Right: difference in ISO and NFW χ^2 values. Stars represent good fits with $\chi^2_R(\text{ISO}) < 2$ and $\chi^2_R(\text{NFW}) < 2$. Filled squares represent fits with $\chi^2_R(\text{ISO}) > 2$ or $\chi^2_R(\text{NFW}) > 2$.

Table 7
Uncertainties in Model Parameters

Name (1)	Type (2)	Δ (3)	ISO Halo			NFW Halo		
			R_C (4)	ρ_0 (5)	χ^2_r (6)	c (7)	V_{200} (8)	χ^2_r (9)
NGC 2403	total	4.64 ± 1.09	2.14 ± 0.05	77.9 ± 3.3	0.79	9.8 ± 0.2	110.2 ± 1.0	0.56
	disp	4.22 ± 1.21	2.16 ± 0.05	77.1 ± 3.3	0.94	9.9 ± 0.2	109.5 ± 0.9	0.70
	fit	0.21 ± 0.15	2.07 ± 0.05	80.2 ± 3.0	399.24	10.5 ± 0.2	105.2 ± 1.2	403.93
DDO 154	total	2.40 ± 0.91	1.34 ± 0.06	27.6 ± 1.6	0.44	4.4 ± 0.4	58.7 ± 4.3	0.82
	disp	2.25 ± 0.90	1.31 ± 0.05	28.4 ± 1.7	0.51	4.4 ± 0.4	59.0 ± 4.2	0.87
	fit	0.13 ± 0.07	1.44 ± 0.06	24.7 ± 1.5	141.15	5.6 ± 0.3	49.5 ± 2.0	168.37

Notes. (1) Name of galaxy; (2) definition of uncertainties; total is the definition adopted in this paper; disp is the dispersion in velocities along tilted rings; fit is the formal fit error in rotation velocity; (3) average value and dispersion of uncertainties; (4)–(9) halo fit parameters, definitions as in Tables 3–6.

In determining the halo parameters and the corresponding uncertainties, the GIPSY ROTMAS software uses a simple least-squares procedure. The uncertainties in the rotation velocity should therefore be reflected in the uncertainties in the halo parameters, and our definition of the rotation velocity uncertainties could thus potentially have an impact on the values we derive. We evaluated the effect of adopting a different definition for the uncertainties (as discussed in Section 3.6) on the fit parameters, and found the resulting differences to be small, and certainly negligible when compared with the differences introduced by small variations in $\Upsilon_*^{3.6}$. We illustrate this for two typical galaxies in Table 7, where we list the fitted parameters for the ISO and NFW halos, assuming fixed $\Upsilon_*^{3.6}$ values, and adopting respectively, (1) our original definition for the uncertainties, (2) the dispersion of velocities along the rings, and (3) the formal fit error in the rotation velocity.

The extreme values for χ^2_r as found when adopting the formal fit error from ROTCUR immediately show that these severely underestimate the true uncertainties, as already discussed in Section 3.6. It is clear that for the other two definitions of the errors, small differences in the resulting halo parameters exist, but it is also clear that different (reasonable) definitions of the uncertainties do not dominate the error budget: the largest uncertainty is introduced by the stellar mass-to-light-ratio Υ_* (compare the results in Table 7 with those in Tables 3–6). In summary, our definition and treatment of the uncertainties in the rotation velocities does not dominate the final uncertainties in the halo parameters.

7.4.2. Halo Parameters

We now consider the decompositions with $\Upsilon_*^{3.6}$ as a free parameter (Tables 5 and 6). The corresponding χ^2_r values are compared in Figure 64. The left panel compares the values of χ^2_r for both models, plotted against absolute luminosity. Three galaxies ($\chi^2_r > 2$) are obviously not well described with either model. Concentrating on the other galaxies, we see a systematic difference between high- and low-luminosity galaxies. The luminous galaxies show comparable χ^2_r values for either model; the low-luminosity galaxies with $M_B \gtrsim -19$ are clearly better described using the ISO model. This is shown more clearly in the right-hand panel of Figure 64, where we show the difference between the χ^2 values for both models as a function of luminosity.

NFW and ISO models thus fit equally well for high-luminosity galaxies, with reasonable $\Upsilon_*^{3.6}$ values. The extent to which this is determined by subtle trade-offs between, e.g., dynamical contributions of bulge, disk, and halo still needs to be determined, but such an analysis is likely limited by the accuracy with which stellar mass-to-light ratios can be determined from photometric data and models. Alternative methods (via, e.g., dispersion measurements) will be needed to constrain the importance of the disk further.

Regarding the low-luminosity galaxies, Trachternach et al. (2008) show, from harmonic decompositions of the velocity fields, that noncircular motions are lowest in these galaxies. The increasing incompatibility of the NFW model toward lower luminosities is, therefore, difficult to explain purely in terms

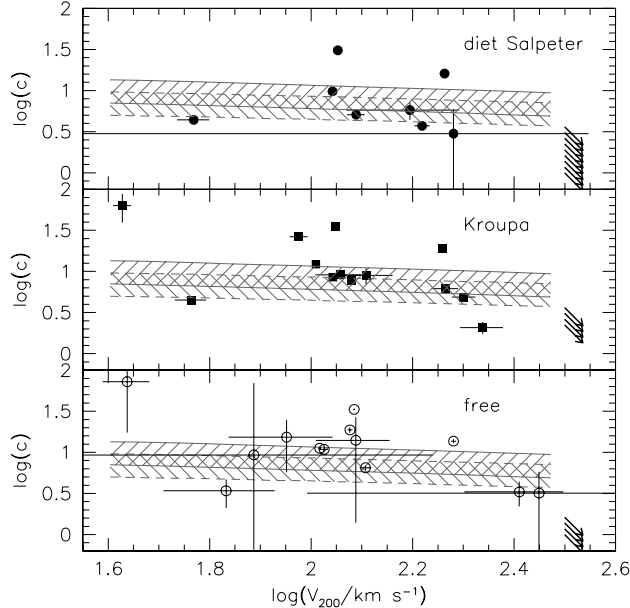


Figure 65. Left: distribution of c as a function of V_{200} for the various assumptions on $\Upsilon_*^{3.6}$. The upper panel shows the results assuming the fixed (photometric) $\Upsilon_*^{3.6}$ values with a diet Salpeter IMF. The center panel shows the same but for a Kroupa IMF. The bottom panels uses the free $\Upsilon_*^{3.6}$ values. Arrows in the bottom-right corners indicate the fits with $c < 1$. The hatched area bordered by the full curves indicates the predicted $c - V_{200}$ relation based on the “vanilla” Λ CDM cosmology presented in Tegmark et al. (2004). The counter-hatched area bordered by the dashed curves shows the relation that can be derived from the three-year WMAP results (Spergel et al. 2007). The widths of the distributions correspond to the $\pm 1\sigma$ scatter in c as derived from CDM simulations (Bullock et al. 2001).

of these noncircular motions. Note also that the current sample has been observed at identical and homogeneous sensitivity and resolution and has been analyzed in a consistent manner. The differences found here can therefore not be attributed to different data qualities or analysis methods.

Last, we investigate the model parameters. To start with the NFW model, as described before, the fit parameters c and V_{200} are related and their values are determined by the assumed cosmology (Section 5.3.1). McGaugh et al. (2007) show the relation between c and V_{200} for the “vanilla Λ CDM” model presented in Tegmark et al. (2004), and the three-year WMAP results of Spergel et al. (2007). Both show a fairly flat distribution of c as a function of V_{200} , but with a different offset (due to a different power spectrum normalization). Both distributions are shown in Figure 65 along with the 1σ spread expected from simulations (Bullock et al. 2001). It is clear that for rotation curves that are consistent with CDM, we expect to find concentration values between $c \sim 4$ and $c \sim 10$, fairly independent of V_{200} . In Figure 65 we also plot the values for c and V_{200} derived from our rotation curve fits, both for photometrical (diet Salpeter and Kroupa IMF) and dynamical $\Upsilon_*^{3.6}$ values. Also indicated are the galaxies for which no sensible fitting parameters could be derived. It is immediately clear that the distribution of c values we find shows much more scatter than the CDM relations. At first glance, one could conclude that we have found c values that are on average higher than predicted, but it is not clear to what extent our distribution is affected by the absence of galaxies for which sensible NFW parameters could not be derived.

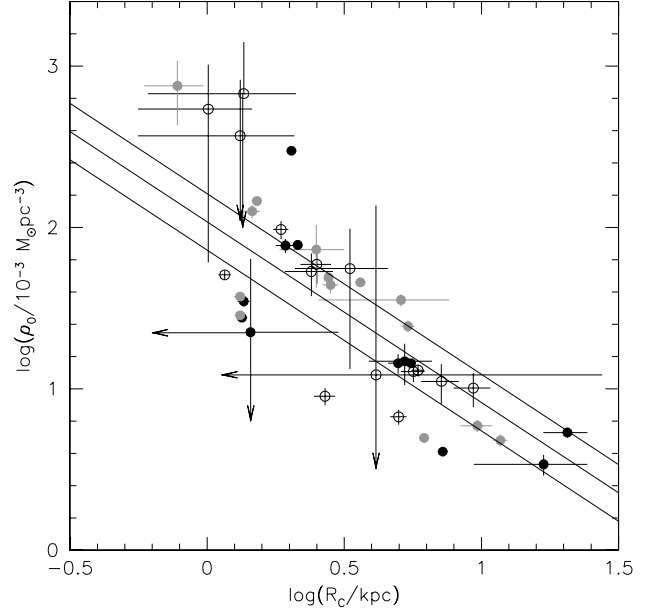


Figure 66. Left: distribution of core density ρ_0 of the ISO halo against core radius R_C . Filled circles show the results derived assuming fixed $\Upsilon_*^{3.6}$ values, with black symbols assuming a diet Salpeter IMF and gray circles assuming a Kroupa IMF. Open circles show the results derived using free $\Upsilon_*^{3.6}$ values. The full lines show the relation derived in Kormendy & Freeman (2004) along with the 1σ scatter.

As the ISO halo has no basis in current cosmology, there are no a priori expectations for its model parameters. One can, however, still derive them and check for possible trends with other fundamental galaxy parameters, as Kormendy & Freeman (2004) have done. Figure 66 shows the distribution of the central density ρ_0 against the core radius R_C . The distribution is consistent with the Kormendy & Freeman (2004) relation (their Equation 20), but with slightly larger scatter.

Similar relations with the absolute luminosity (shown in Figure 67) are less well-defined. The most noteworthy aspect is that most galaxies have a core radius $R_C > 1$ kpc, independent of the adopted value for $\Upsilon_*^{3.6}$, showing that the effects of the “soft” core are already clearly noticeable well outside the central regions. In other words, while scales smaller than ~ 1 kpc are needed for a clear distinction between cusp and core, “symptoms” of the core should already be visible at scales larger than that.

8. SUMMARY

We present a uniquely high-resolution analysis of the kinematics of 19 galaxies. The galaxies form part of THINGS, and have therefore been observed and analyzed in a homogeneous and consistent manner. The high spatial and velocity resolution, as well as the exquisite sensitivity, enable us to derive the tilted-ring parameters based solely on the H α data. There is, therefore, no dependence on, e.g., optical inclinations or axis ratios, which generally carry their own systematic effects with them. We summarize our results below.

1. We determine the 3.6 μ m stellar mass-to-light ratio $\Upsilon_*^{3.6}$ in two fully independent ways: one is based on population synthesis modeling (Oh et al. 2008) and the other is a purely “dynamical” $\Upsilon_*^{3.6}$, determined solely by the best fit $\Upsilon_*^{3.6}$ value in the rotation curve mass model. For the population

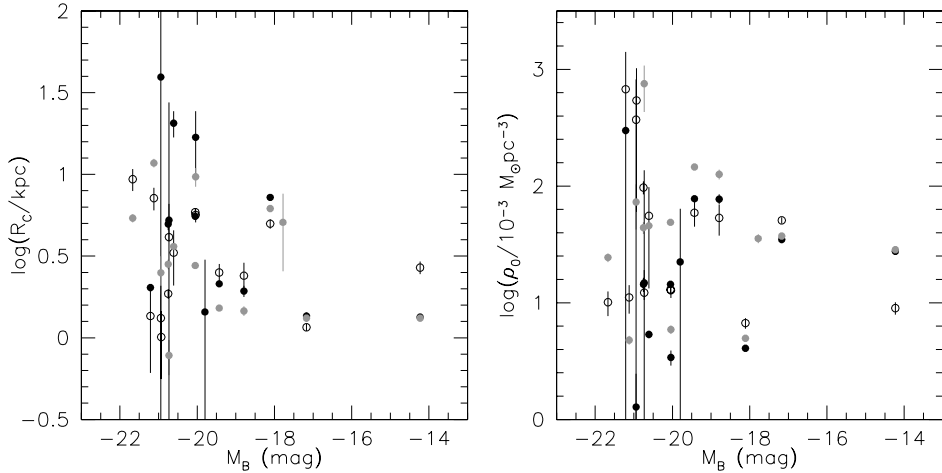


Figure 67. Left: distribution of ISO halo core radius R_C (left panel) and core density ρ_0 (right panel), plotted against absolute luminosity M_B . Filled symbols indicate the fixed $\gamma_*^{3.6}$ results, with black circles representing the diet Salpeter fits and gray circles the Kroupa fits. The open circles show the free $\gamma_*^{3.6}$ outcomes.

synthesis $\gamma_*^{3.6}$ values, we consider two assumptions for the IMF: the diet Salpeter IMF (Bell & de Jong 2001), designed to fit maximum disk models, and the Kroupa (2001) IMF, which yields disks that are $\sim 40\%$ lighter. We find good agreement between the photometric and dynamical $\gamma_*^{3.6}$ values, especially for the Kroupa IMF. The close match between the dynamical and population synthesis results indicates the stellar disks of the galaxies in the THINGS sample do not contain large amounts of dark matter associated with the disks themselves. The dark matter content of the THINGS galaxies is associated with the halo, not the disk. Our analysis also obviates the need for so-called minimum or maximum disk approaches.

2. We do not find any steeply declining rotation curves out to the last measured point. Specifically, previous observations seemed to indicate declining rotation curves for NGC 3521, NGC 7793, NGC 2366, and DDO 154. With the increased resolution of the data we can now better trace the inclination and P.A. trends. Any gentle decreases in the velocity that we still find can now be attributed to uncertainties in the rotation velocity or inclination. There is, therefore, no evidence from THINGS that we have probed the “edge” of a dark matter halo.
3. We fit NFW and ISO models to our rotation curves using our best estimates for $\gamma_*^{3.6}$. We find that for galaxies $M_B < -19$ both models statistically fit equally well. Note, however, that for the 11 galaxies in this high-luminosity bin, the fixed $\gamma_*^{3.6}$ diet Salpeter NFW fits result in four galaxies with nonphysical (severely inconsistent with CDM) halo parameters. These unphysical cases disappear when a Kroupa IMF is assumed. However, the resulting halo parameters still show a scatter much larger than the simulation predict.
4. For galaxies with $M_B > -19$ the core-dominated ISO model fits significantly better than the NFW model (and the fixed $\gamma_*^{3.6}$ NFW fits yield four out of five galaxies with nonphysical halo parameters independent of IMF assumption). The success of the ISO halo for these galaxies is remarkable, given the conclusion by Trachternach et al. (2008) that the THINGS low-luminosity galaxies have the smallest noncircular motions: the observed dynamics most likely reflect that of the dark matter halo.

5. We find that the low-luminosity galaxies in our sample are dark matter-dominated throughout, based on both the population synthesis $\gamma_*^{3.6}$ values, as well as the “dynamical” $\gamma_*^{3.6}$ results. As noted above, the agreement between these two sets of values indicates the dark matter is not associated with the stellar disk. The dark matter rotation curves of these galaxies are about 0.2 dex (a factor 1.6) lower than predicted by CDM over their entire disks. This implies that the density of dark matter in real late-type galaxies is $\sim 50\%$ of what is predicted by CDM simulations.

We thank the anonymous referee for carefully reviewing this paper. It is a pleasure to thank Adam Leroy for the many IMF discussions, Nicolas Bonne for his initial work on the NGC 2841 rotation curve, and Karen Lewis for her work on NGC 3621. The work of WJGdB is based upon research supported by the South African Research Chairs Initiative of the Department of Science and Technology and National Research Foundation. E.B. gratefully acknowledges financial support through an EU Marie Curie International Reintegration Grant (Contract No. MIRG-CT-6-2005-013556). The work of C.T. is supported by the German Ministry for Education and Science (BMBF) through grant 05 AV5PDA/3. This research has made use of the NASA/IPAC Extragalactic Database (NED), which is operated by the Jet Propulsion Laboratory, California Institute of Technology, under contract with the National Aeronautics and Space Administration. This publication makes use of data products from the 2MASS, which is a joint project of the University of Massachusetts and the Infrared Processing and Analysis Center/California Institute of Technology, funded by the National Aeronautics and Space Administration and the National Science Foundation. We acknowledge the usage of the HyperLeda database (<http://leda.univ-lyon1.fr>).

APPENDIX

DATA AND ROTATION CURVE DERIVATION

We present detailed descriptions of the derivations of the tilted ring models and rotation curves of the individual galaxies. For each galaxy we show the Hermite velocity field, the resulting tilted-ring model velocity field, and the difference (residual) velocity field. Additionally, we show overlays of the derived

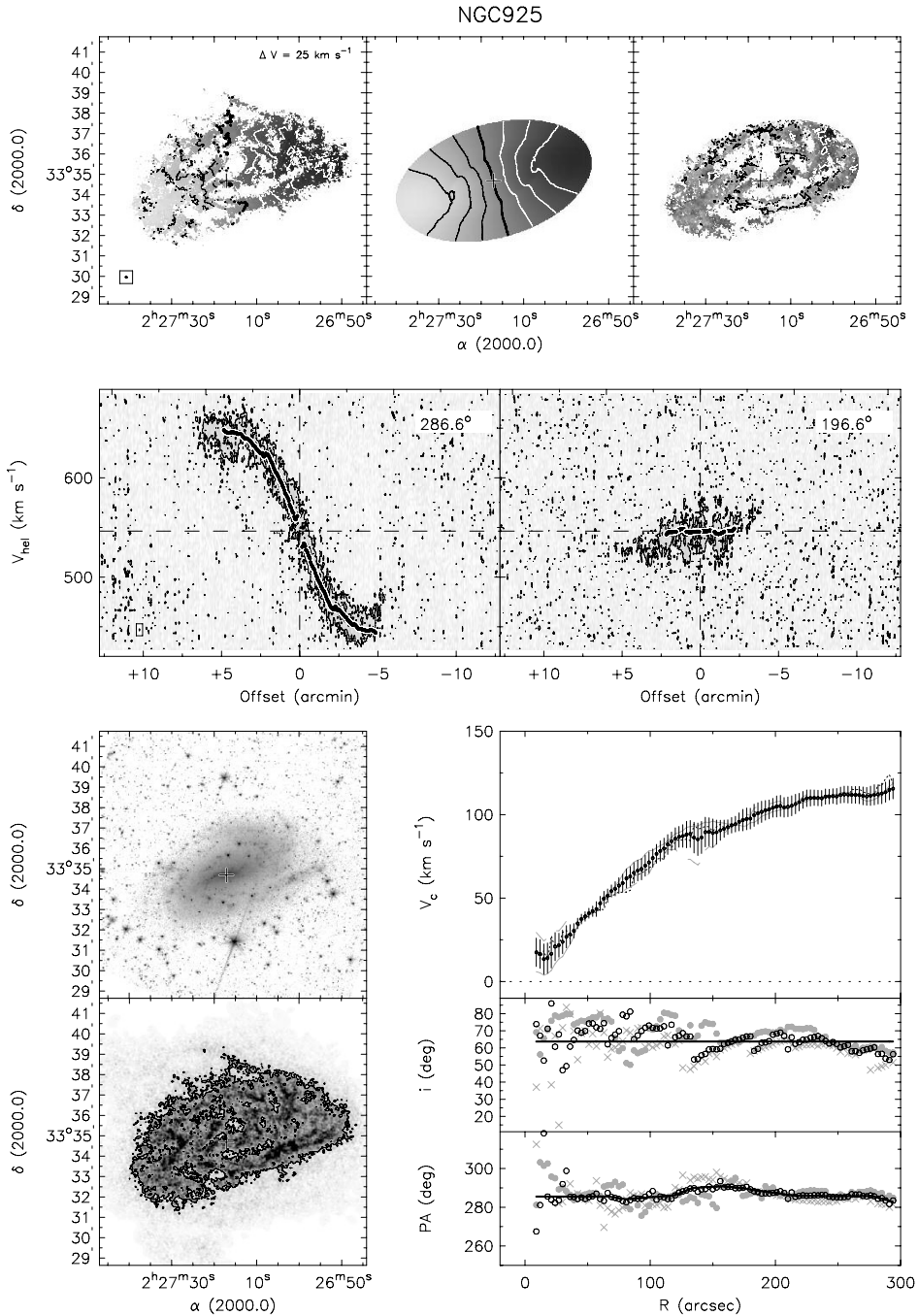


Figure 68. Summary panel for NGC 925. See the Appendix for more information.

rotation curves on minor- and major-axis position–velocity (pV) diagrams, the rotation curves themselves, the radial distributions of P.A. and i , and the positions of the dynamical center in comparison with the integrated H I maps and the SINGS 3.6 μm images.¹⁴ We also briefly discuss the derivation of the various tilted ring parameters for each galaxy.

The rotation curves, velocity fields and other supplementary information are shown in Figures 68–86. The following is a general description of the contents of these figures.

Top row. Left: velocity field derived from fitting Hermite polynomials to the natural-weighted data cube. See Section 3.1 for a description. The systemic velocity is indicated by the thick contour. The spacing ΔV between velocity contours is indicated in the figure. The approaching side can be identified by the light gray scales and the dark contours. The receding side can be identified by the dark gray scales and the white contours. The adopted dynamical center is indicated with a cross. The beam size is indicated by the ellipse enclosed by the rectangle in the bottom-left corner. Center: model velocity field derived from the tilted-ring model. Gray scales and contour levels are identical to those in the observed velocity field in the left panel.

¹⁴ Note that NGC 2366, NGC 2903 and DDO 154 are not part of the SINGS sample. For these galaxies we have retrieved data from the *Spitzer* archive.

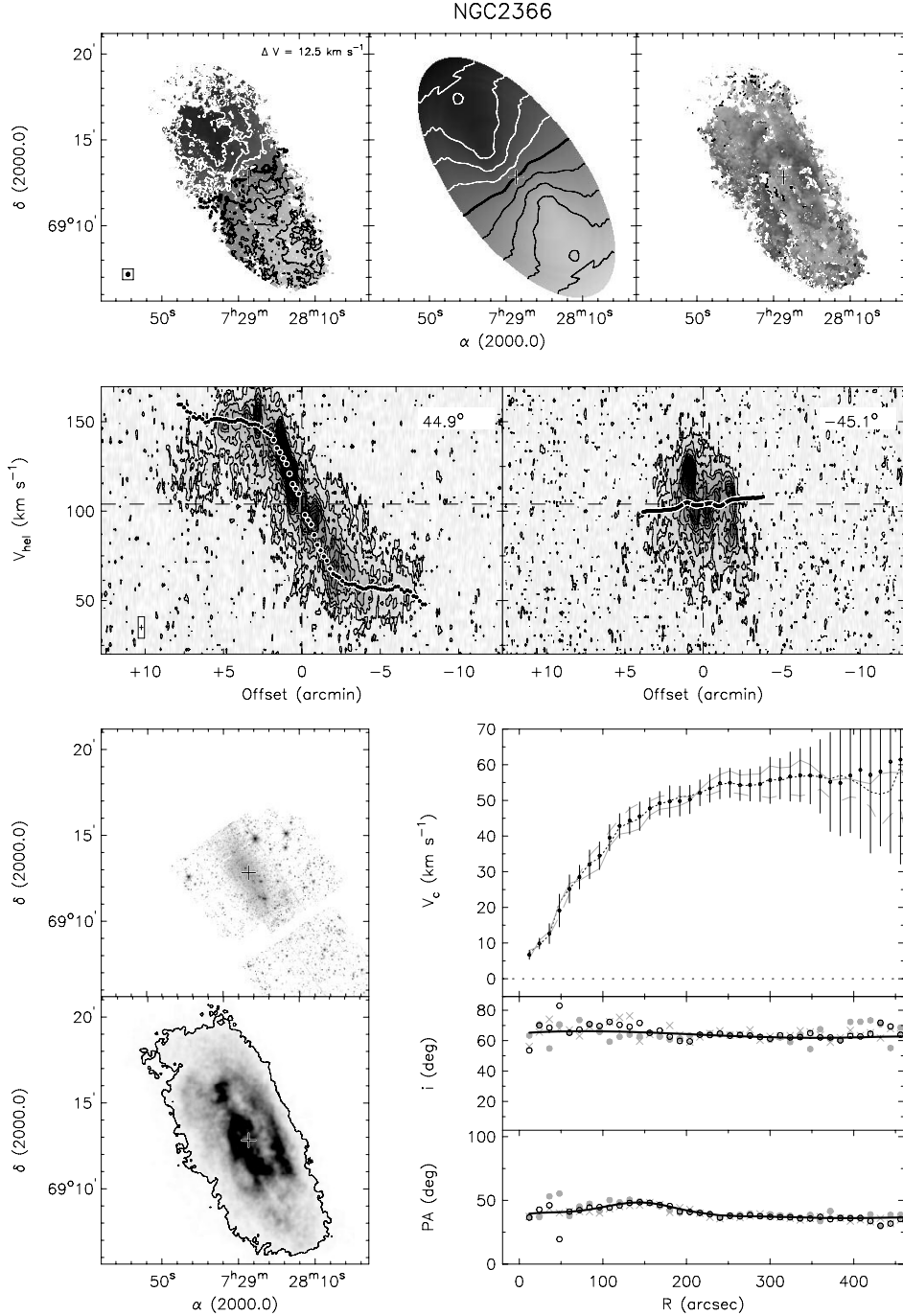


Figure 69. Summary panel for NGC 2366. See the [Appendix](#) for more information.

Right: residual velocity field defined as the observed velocity field minus the model velocity field. The gray scale range runs from -20 km s^{-1} (white) to $+20 \text{ km s}^{-1}$ (black). Contour levels are $-10, -20, -30, \dots \text{ km s}^{-1}$ (black) and $+10, +20, +30, \dots \text{ km s}^{-1}$ (white).

Centre row. Left: position–velocity diagram taken along the average P.A. of the major axis as listed in Table 2. This P.A. is also indicated in the top-left of the panel. The thickness of the slice equals one pixel (typically $1''.5$; see Walter et al. 2008) in the corresponding cube. Contours start at $+2\sigma$ in steps of 4σ (full contours), and -2σ in steps of -4σ (dotted contours). The

systemic velocity and position of the center are indicated by dashed lines. Overplotted is the rotation curve projected onto the average major axis using the derived radial variations of P.A. and i . The spatial and velocity resolutions are indicated by the cross enclosed by the rectangle in the bottom-left corner. Right: position–velocity diagram taken along the average minor axis. Contours and symbols are as in the major axis diagram. Overplotted is the rotation curve but projected onto the average minor axis using the derived radial variations of P.A. and i .

Bottom-left panel. Top: the $3.6 \mu\text{m}$ IRAC *Spitzer* image. For all galaxies, the same logarithmic intensity scale was

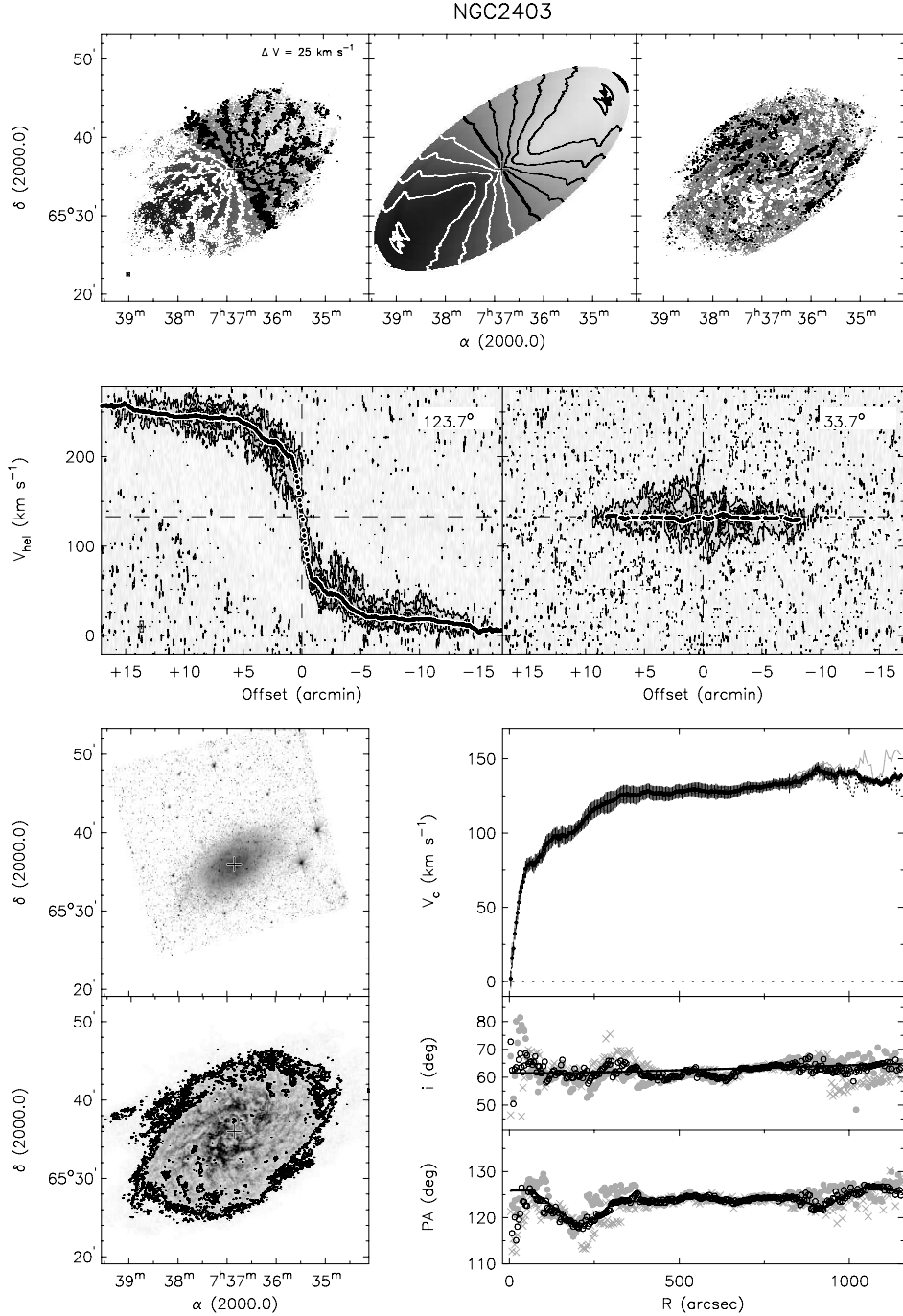


Figure 70. Summary panel for NGC 2403. See the [Appendix](#) for more information.

used, running from $\log(I/\text{(MJy ster}^{-1}) = -2$ (white) to $\log(I/\text{(MJy ster}^{-1}) = +1$ (black). The dynamical center is indicated by a cross. Bottom: integrated H₁ map. The dynamical center is indicated by a cross. The maximum column density level displayed (black) is $2 \times 10^{21} \text{ cm}^{-2}$. The contour indicates the 3σ level. This level was computed as follows: for the standard THINGS cubes $\sigma_{\text{tot}} = \sqrt{N}\sigma_{\text{chan}}$, where σ_{tot} is the noise in the integrated H₁ map, σ_{chan} the noise in one channel, and N the number of channels contributing to a pixel.

Bottom-right panel. Top: the rotation curve corresponding to the tilted-ring model is represented by the black filled circles. The error-bars correspond to the dispersion of the velocity values found along the corresponding ring. This rotation curve was derived with all parameters fixed to their final values (as indicated by the thick black curves in the P.A. and inclination panels below). The full drawn gray line shows the corresponding rotation curve of the approaching side derived using these adopted distributions of inclination and P.A. The

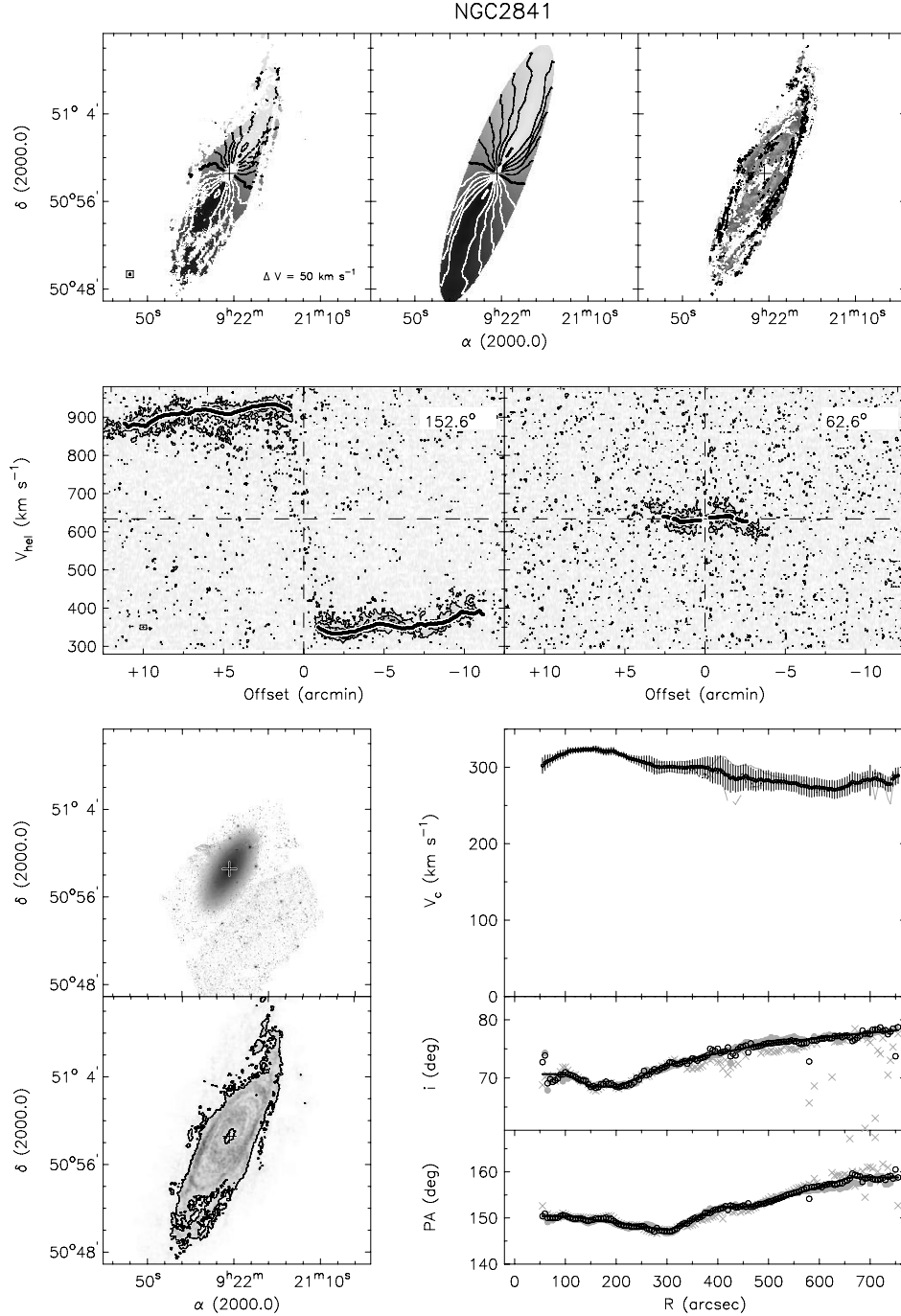


Figure 71. Summary panel for NGC 2841. See the [Appendix](#) for more information.

dashed gray line shows the equivalent rotation curve of the receding side. The dotted black curve indicates the rotation curve of the entire disk derived with P.A. and inclination as free parameters. The uncertainties in the rotation velocity are defined as the quadratic addition of the dispersion in velocities found along each ring and one quarter of the difference between the approaching and receding sides velocity values. See Section 3.5 for a full discussion. Center and bottom: inclination and P.A. values used in the tilted-ring models. The open circles show the distribution of inclination and P.A. when left as free

parameters. These values result in the dotted black rotation curve described above. The crosses show same for the approaching side, the gray filled circles for the receding side. The thick black lines indicate the distributions for P.A. and inclination that were ultimately adopted to derive the rotation curves in the panel above.

We now discuss details of the derivation of tilted-ring models of individual galaxies.

NGC 925. The results for NGC 925 are shown in Figure 68. NGC 925 is classified as a late-type barred spiral. A small

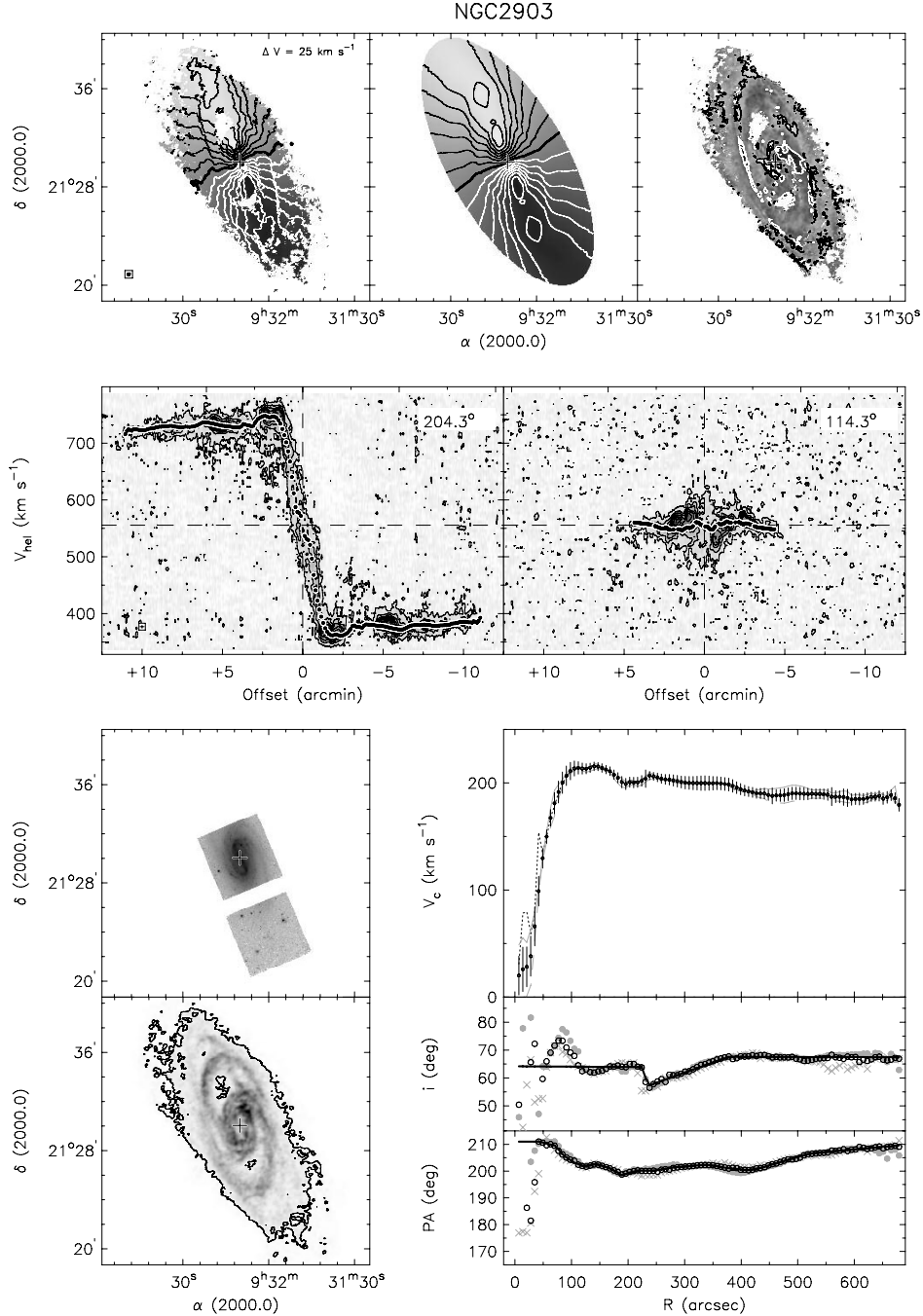


Figure 72. Summary panel for NGC 2903. See the [Appendix](#) for more information.

weak central bar-shaped component is indeed visible in the IRAC 3.6 μm image. The outer parts are dominated by a two-armed spiral, with the southern arm also prominently visible in H α . With the dynamical center fixed, we find that V_{sys} varies from $\sim 555 \text{ km s}^{-1}$ in the center to $\sim 545 \text{ km s}^{-1}$ at $R \sim 120''$. At larger radii, V_{sys} settles at a constant value of $546.6 \pm 0.6 \text{ km s}^{-1}$. This value is very close to the average value determined over the entire radial range ($546.3 \pm 3.9 \text{ km s}^{-1}$), and we adopt the latter value as the systemic velocity. This value is slightly lower than the central value of the global profile of 552.5 (551.5) km s^{-1} as measured at the 20 (50)% level. The P.A. distribution is continuous and well defined.

The inclination shows some scatter, but a global trend from $i \sim 75^\circ$ in the inner parts to $i \sim 60^\circ$ in the outer parts is clearly visible, indicating a slight warp in NGC 925. The rotation curve derived using the P.A. and inclination models is almost identical to the one with P.A. and i as free parameters. Despite the asymmetric appearance of the H α disk, the approaching and receding sides are fairly symmetric in terms of their rotation velocity.

NGC 2366. The data and analysis of NGC 2366 are given in Oh et al. (2008). For completeness, we summarize the data and analysis in Figure 69, but refer to their paper for a complete discussion.

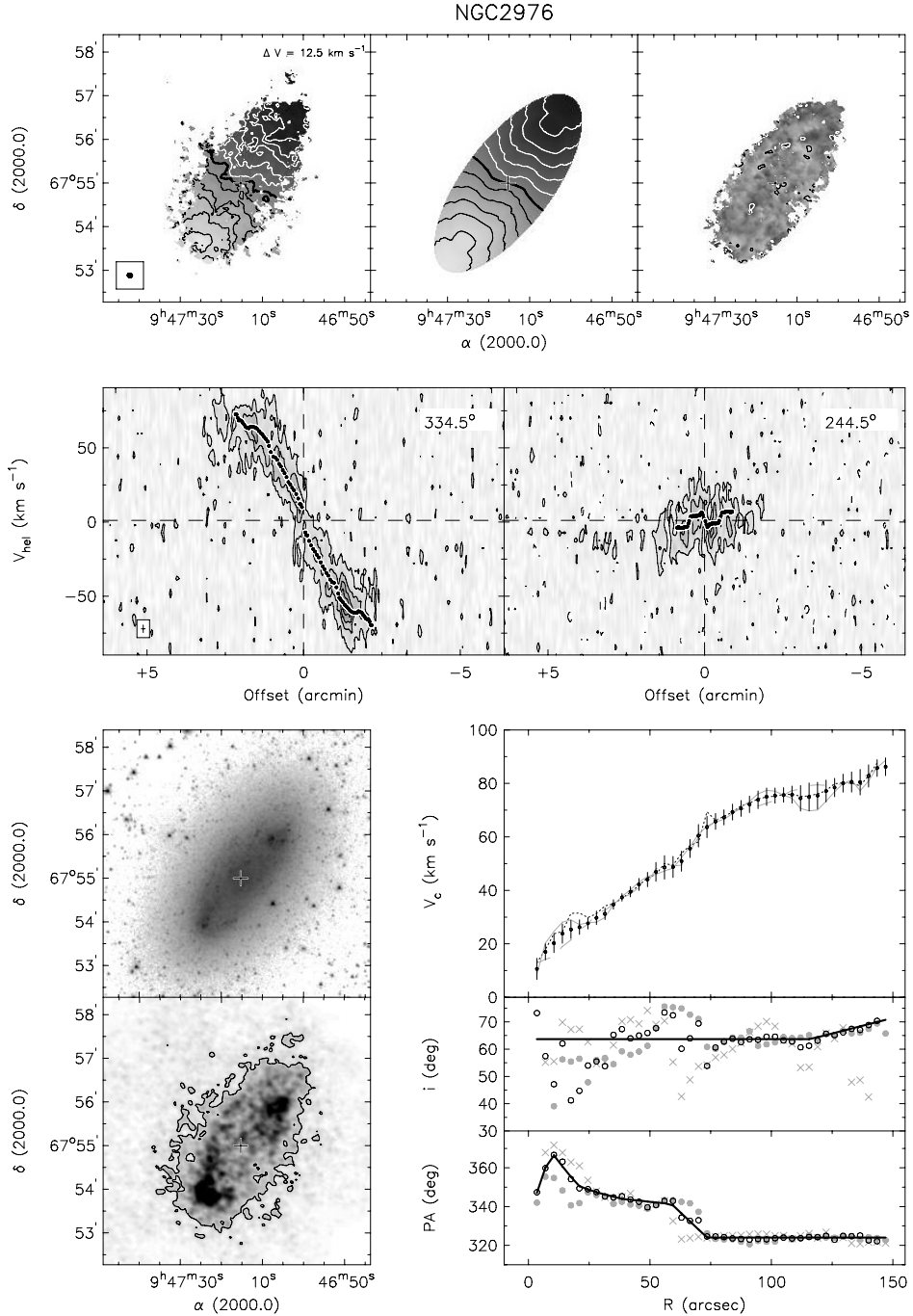


Figure 73. Summary panel for NGC 2976. See the [Appendix](#) for more information.

NGC 2403. NGC 2403 is a late-type Sc spiral and member of the M81 group. We present the data in Figure 70. The IRAC 3.6 μm image shows multiple spiral arms, some of which are also evident in the integrated H α map. The velocity field of NGC 2403 is very regular as shown by the perpendicular major and minor axes and the close agreement between approaching and receding sides. The small wiggles in the inclination distribution are caused by streaming motions induced by the spiral arms, also visible as residuals in the residual velocity field. After fixing the position of the dynamical center, we find the systemic

velocity to be well-behaved, showing no large-scale trend with radius. The average value is $V_{\text{sys}} = 132.8 \pm 1.6 \text{ km s}^{-1}$, which is the value we adopt here. This value is close to the central velocity of 133.1 (134.8) km s^{-1} derived from the global profile at the 20 (50)% level. The inclination and P.A. are well-behaved. A comparison of the curve with P.A. and i as free parameters with the curve which has these parameters fixed using the model distributions shows no appreciable differences. Note the remarkable symmetry between approaching and receding sides in rotation velocity, inclination, and P.A. between $450'' \lesssim R \lesssim 850''$.

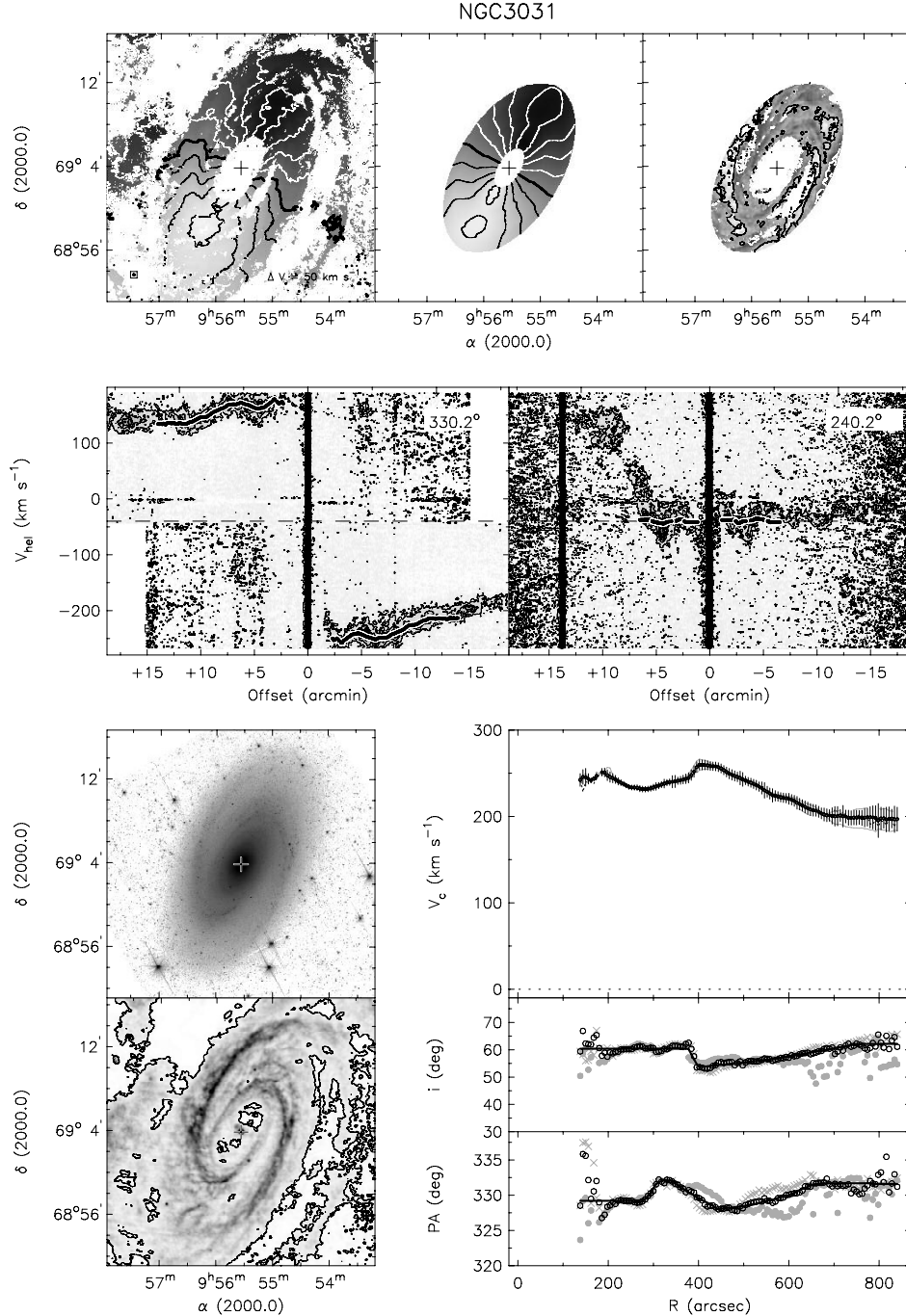


Figure 74. Summary panel for NGC 3031. See the [Appendix](#) for more information.

NGC 2841. NGC 2841 is an early-type (Sb) spiral which is dominated by a prominent central bulge, as well as a central hole in the H_I distribution, as shown in Figure 71. The tightly-wound spiral structure is also visible in the inner part of the H_I distribution; in the outer parts the disk is dominated by two arms which seem to bend away out of the plane of the inner disk. The velocity field is regular in the inner parts but in the outer regions shows clear evidence for the presence of a warp. The major-axis slice shows that at the outer edge of the central H_I hole the rotation has already almost reached its maximum value. After

fixing the central position, we find a systemic velocity that is constant within $R < 350''$, but starts to deviate at larger radii. Due to the obvious presence of the warp at these larger radii, we adopt the average value within $R = 350''$ as our best value: $V_{\text{sys}} = 633.7 \pm 1.8 \text{ km s}^{-1}$. This agrees well with the central velocity derived from the global profile at the 20 (50)% level of 635.2 (636.2) km s^{-1} . With the systemic velocity and dynamical center fixed, we find well-defined distributions of P.A. and i with radius. Despite the warp, NGC 2841 is very symmetrical with no obvious differences in P.A. and i for the approaching and

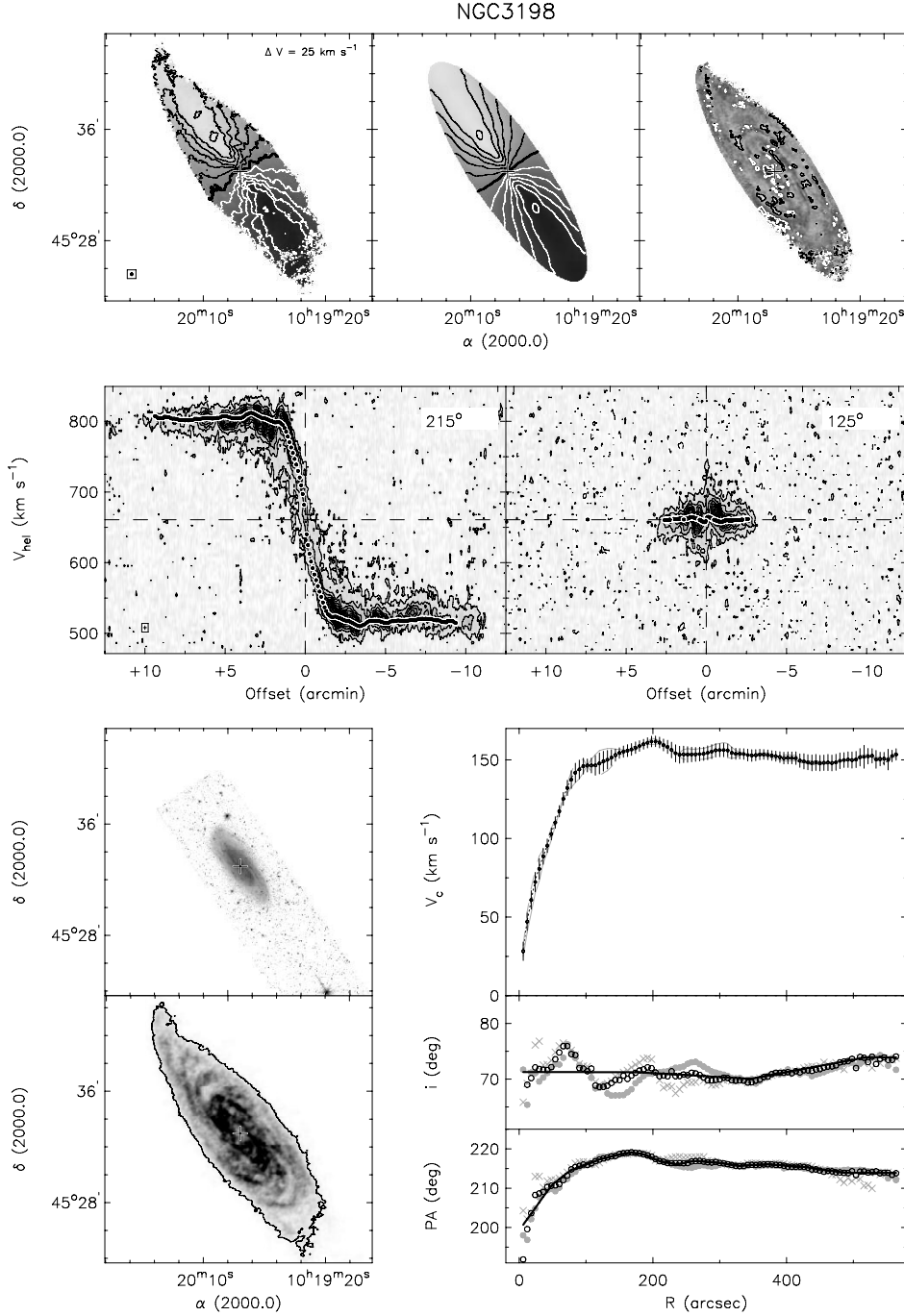


Figure 75. Summary panel for NGC 3198. See the [Appendix](#) for more information.

receding sides. Our best model for the inclination shows an approximately constant value of $i \sim 70^\circ$ for $R \lesssim 200''$, with a gradual but systematic increase to $i \sim 78^\circ$ in the outer parts. The rotation curve with P.A. and i as free parameter is identical (within the uncertainties) to the one derived with P.A. and i fixed.

NGC 2903. As can be seen in Figure 72, the appearance of NGC 2903 is dominated by tightly-wound spiral arms and a bar as visible in the $3.6\ \mu\text{m}$ image. The velocity field and integrated H α map can be divided into two distinct regions: in the inner parts

we find an H α ring, corresponding to the bar and inner spiral arms as seen in the IRAC image. At the outer radii, we see a lower surface density disk which is dominated by two broad H α spiral arms. These two regions are clearly separated around $R \sim 240''$ by minima in the H α column density. The kinks in the velocity contours near the outer spiral arms clearly indicate the presence of noncircular motions there. The very inner parts of the disk also show a strong twist in the P.A. of the kinematic major axis, very likely due to the effect of the bar and associated streaming motions. Their presence is also implied by the motions that

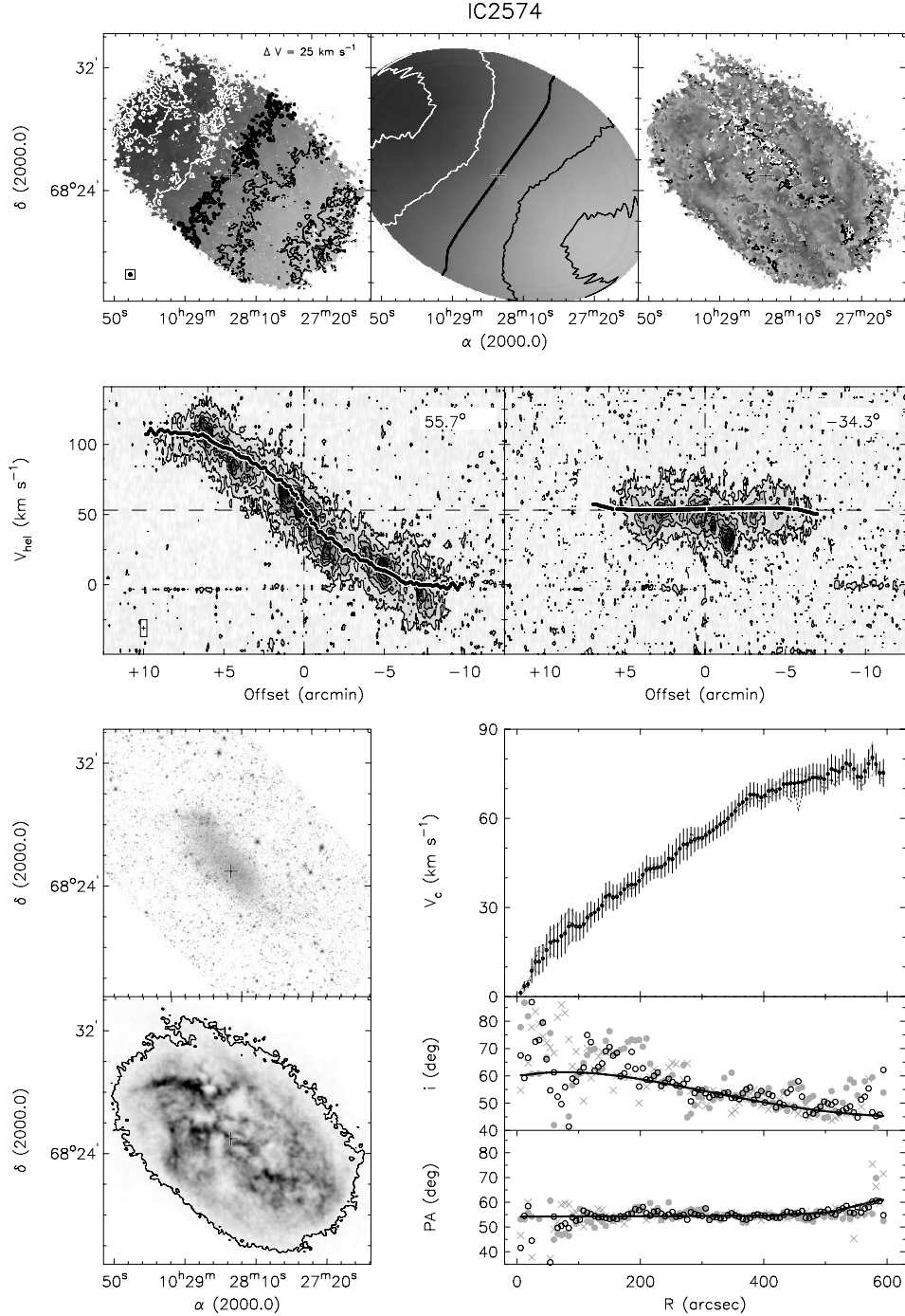


Figure 76. Summary panel for IC2574. See the [Appendix](#) for more information.

can be seen in the minor axis profile and the increased width of the profiles in the inner parts (visible in the major axis position–velocity diagram). With the position of the dynamical center fixed, the systemic velocity still shows large changes in the inner parts, most likely due to the effects of the bar. We fixed V_{sys} to the average value between $200'' < R < 400''$ and find $V_{\text{sys}} = 555.6 \pm 1.3 \text{ km s}^{-1}$. This agrees well with the central velocity from the global profile derived at the 20 (50)% level of 556.6 (555.7) km s^{-1} . The inclination and P.A. for $R \gtrsim 100''$ are straightforward to model, but at smaller radii

both show large variations. The sudden change in inclination at $R \sim 110''$ corresponds to the outer radius of the bright, compact spiral arms associated with the central bar, whereas the sudden change in P.A. at $R \sim 60''$ occurs where the bright tips of the straight central bar are found. As both of these changes are associated with non-rotational motions, we have for our tilted-ring models simply extrapolated the innermost unaffected values inwards.

NGC 2976. NGC 2976 is classified as an Sc galaxy. Its analysis is illustrated in Figure 73. The IRAC 3.6 μm image

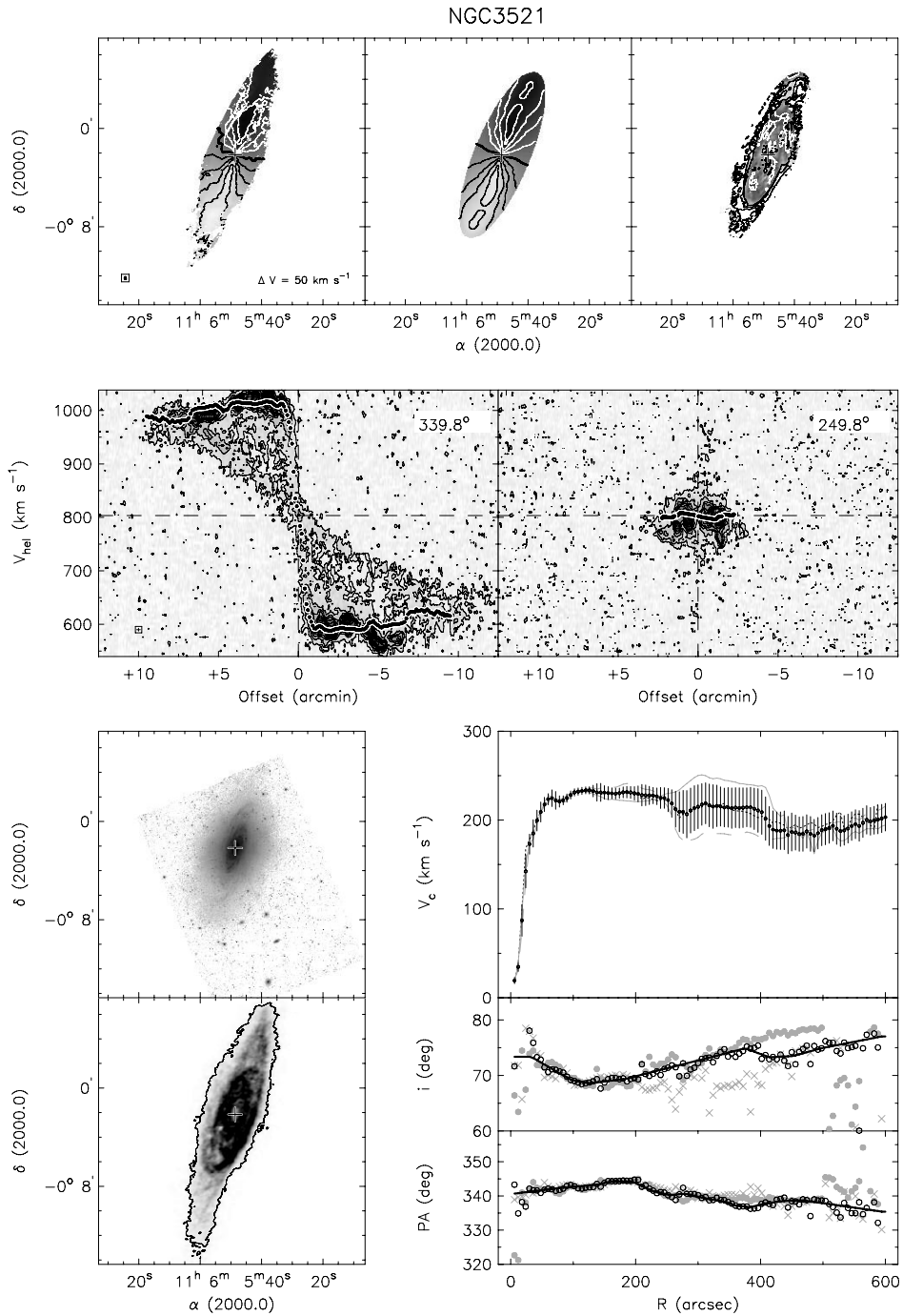


Figure 77. Summary panel for NGC 3521. See the [Appendix](#) for more information.

shows no sign of spiral arms or bar component. The stellar component of the galaxy is characterized by two regions of enhanced star formation at either end of the disk, which correspond to the two density enhancements seen in H α . Having fixed the dynamical center, we do not detect systematic trends of V_{sys} with radius except for a slightly larger scatter in the innermost few points. We therefore fix it to the average value for $R > 20''$ and find $V_{\text{sys}} = 1.1 \pm 1.3 \text{ km s}^{-1}$, which compares well with the central value of 2.6 (4.2) km s^{-1} derived from the global profile at the 20 (50)% level. The trend of P.A. with

radius is well defined, and can be approximated by a constant P.A. for $R > 70''$, with a modest increase within that radius. The inclination shows increased scatter within $R < 70''$, and we fix it to the average value derived for $80'' < R < 110''$. The final rotation curve agrees well with the curve derived with P.A. and i free. The residual field also shows no large residuals, indicating that circular motions describe the dynamics of this galaxy well.

NGC 3031. The analysis of NGC 3031 is illustrated in Figure 74. The IRAC 3.6 μm image as well as the H α total

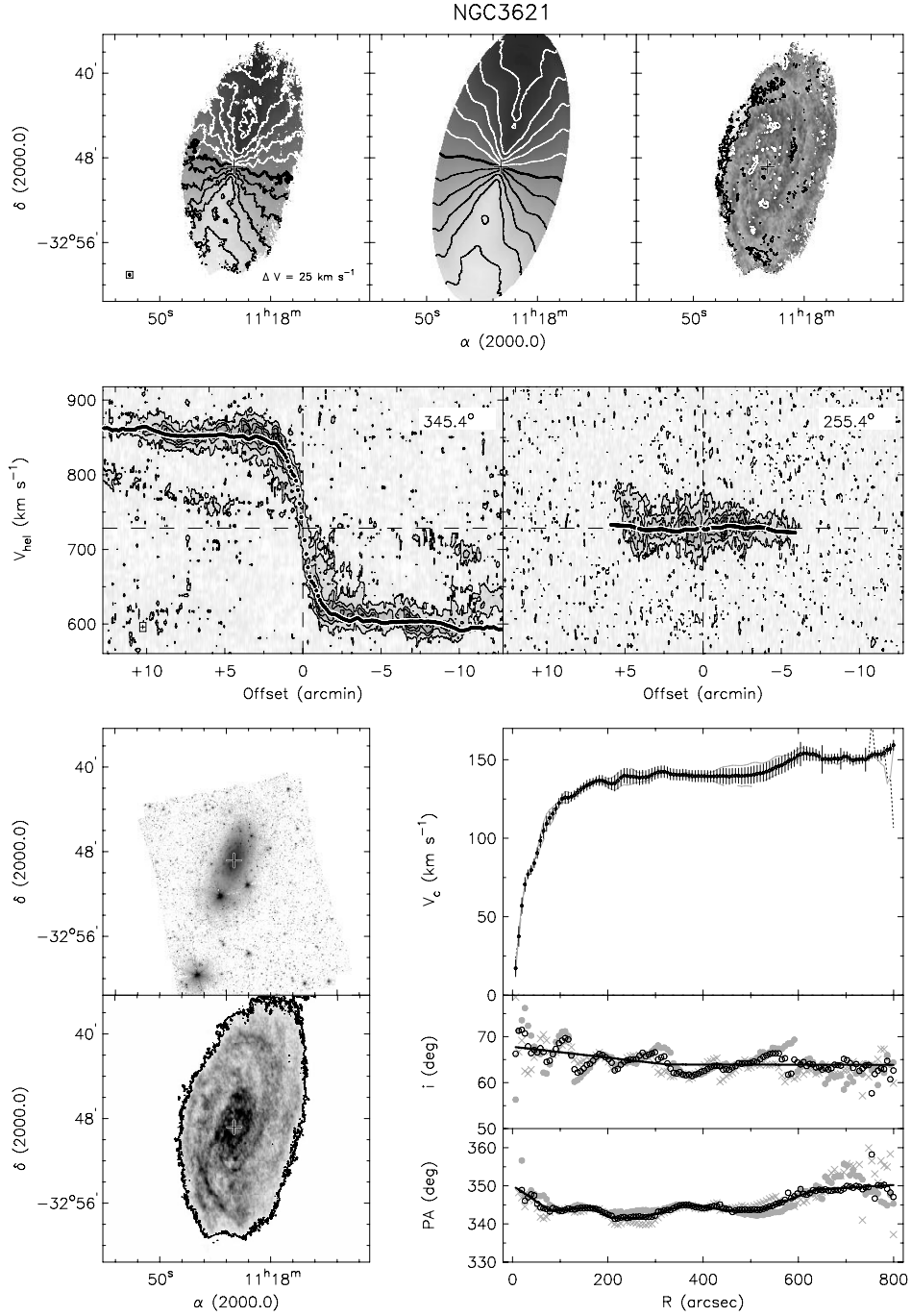


Figure 78. Summary panel for NGC 3621. See the [Appendix](#) for more information.

intensity map show two well-defined spiral arms. The H_I observations used here consist of a mosaic of two separate pointings. Because of this, it was necessary to use a primary-beam corrected data cube. These corrections cause an apparent increase of the noise toward the edges of the field, apparent in the major- and minor-axis slices. Careful blanking of these regions ensured that they did not affect the analysis presented here. Also note that due to the very large velocity width of the gas in the M81 system it was not possible to define line-free channels in order to subtract the continuum (see Walter

et al. 2008). Therefore, the total intensity H_I map as well as the position–velocity slices still contain the radio continuum emission. The central radio continuum source can be seen as the vertical high-intensity feature in the position–velocity slices. An inspection of the velocity field shows that M81 has clear noncircular motions associated with the prominent spiral arms. The residual velocity field clearly shows the effects of these streaming motions. It is also clear that beyond $R \gtrsim 800''$ the H_I gas is no longer in regular rotation around M81. At these large radii the motion of the gas is starting to become dominated by

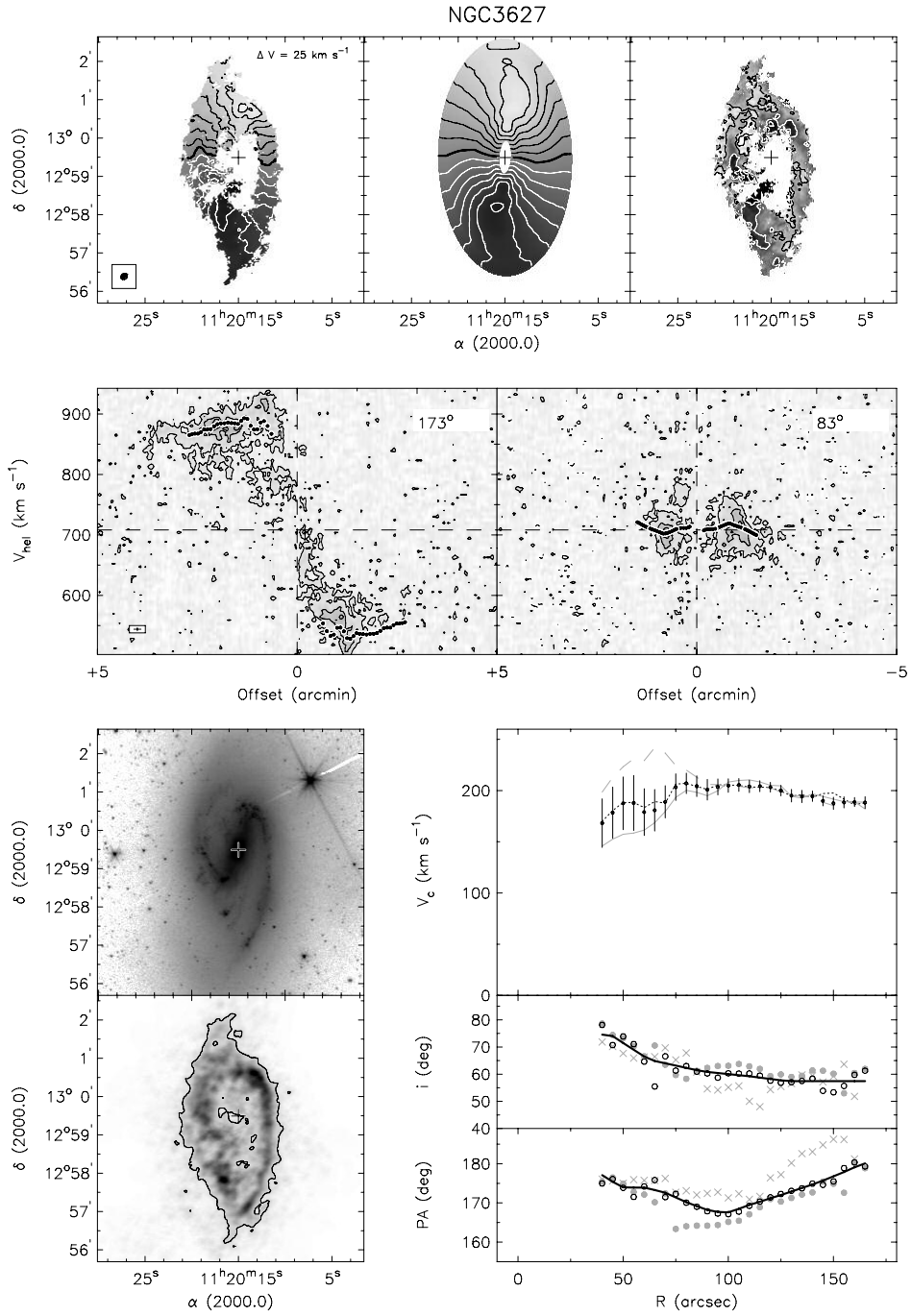


Figure 79. Summary panel for NGC 3627. See the [Appendix](#) for more information.

the tidal interaction processes within the group. For this reason we do not attempt to derive the rotation curve beyond that radius. More evidence for these tidal effects is evident in the minor axis slice where we see a sudden and large deviation of the gas from the systemic velocity. This corresponds to the strong twist in the systemic velocity contour seen in the eastern part of the outer velocity field. After fixing the position of the dynamical center, we determine the systemic velocity by first fixing i and P.A. to indicative values of 60° and 330° , respectively. We find V_{sys} to be constant within $R < 350''$ and use the average value of $-39.4 \pm 2.8 \text{ km s}^{-1}$. This agrees with the central value of

the global H I profile of -39.4 (-41.3) km s^{-1} at the 20 (50)% level. After fixing V_{sys} , and re-running ROTCUR we find well-defined distributions of i and P.A. The radius of $\sim 400''$ at which the sudden change in inclination occurs corresponds to the outer edge of the innermost H I “ring” visible in the integrated H I map. From the P.A. distribution, it is clear that the approaching and receding sides are not entirely symmetrical. The rotation curve itself, by contrast, is. The curve shows a very pronounced drop in the outer parts; however, given the position of M81 within an interacting system, this very likely carries no implication for the distribution of the dark matter.

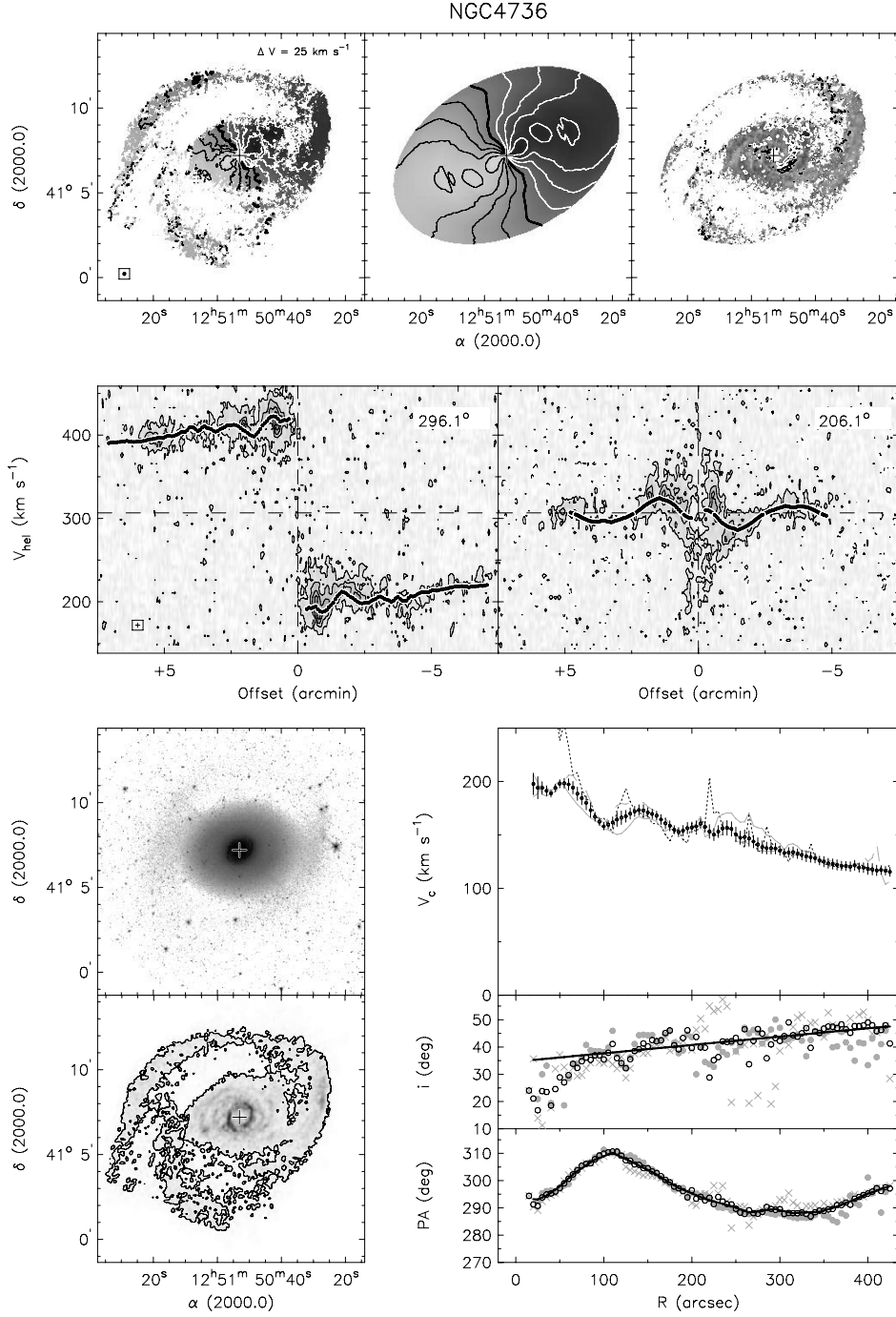


Figure 80. Summary panel for NGC 4736. See the [Appendix](#) for more information.

NGC 3198. The analysis of NGC 3031 is illustrated in Figure 75. The IRAC 3.6 μm image shows two well-defined strong spiral arms, with several less prominent arms branching off from the two main ones. The velocity field is regular with indications of a very modest warp. Small streaming motions due to the two dominant spiral arms show up as small kinks in the velocity contours. These are also visible in the residual velocity field. With the position of the center fixed, we find a well-behaved systemic velocity with an average value $V_{\text{sys}} = 660.7 \pm 2.6 \text{ km s}^{-1}$, which compares favorably

with the central velocity of 661.2 (661.7) km s^{-1} as derived from the global profile at the 20 (50)% level. The P.A. is well defined for all radii; for $R > 300''$, the distribution of i is also well defined, and shows a small but systematic increase. For $R < 300''$ the inclination shows some variations due to motions along the spiral arms (see the low-amplitude pattern visible in the residual velocity field). We therefore adopt an almost constant inclination for $R < 300''$. Note that the rotation curve does not depend on these assumptions: the curve with i and P.A. as free parameters equals the final curve almost

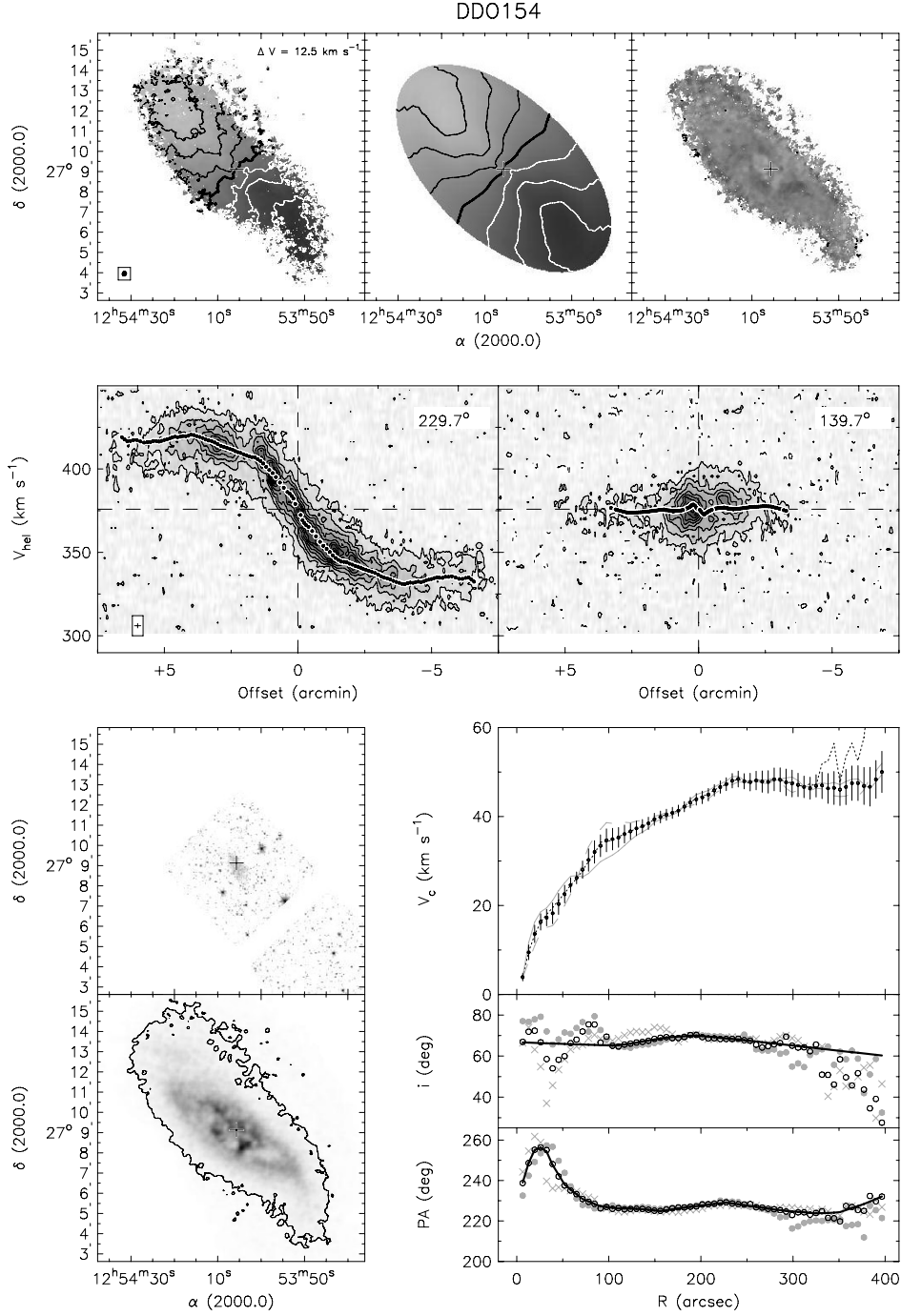


Figure 81. Summary panel for DDO 154. See the [Appendix](#) for more information.

point by point. The approaching and receding sides are very symmetrical.

IC 2574. The data and analysis of IC 2574 are given in Oh et al. (2008). For completeness, we show a summary of their results in Figure 76, but refer to their paper for a complete discussion.

NGC 3521. NGC 3521 is a disk galaxy showing a flocculent spiral structure. The inner H₁ disk seems to be in regular rotation, but the outer disk shows a much different behavior. This is most clearly visible in the channel maps (see

Walter et al. 2008), but can also be seen in the major-axis position–velocity slice, as shown in Figure 77. The central velocity derived from the symmetrical global profile is 798.2 (798.6) km s⁻¹ at the 20 (50)% level. After fixing the position of the dynamical center, the systemic velocity shows a systematic trend with radius and the largest radial variation observed within the THINGS sample. It is constant at a value of ~ 800 km s⁻¹ for $R \lesssim 250''$ (8 kpc) and $R \gtrsim 450''$ (15 kpc), but drops to a value of ~ 777 km s⁻¹ at intermediate radii. Due to the good agreement between V_{sys} values found in the inner and outer parts, we fix

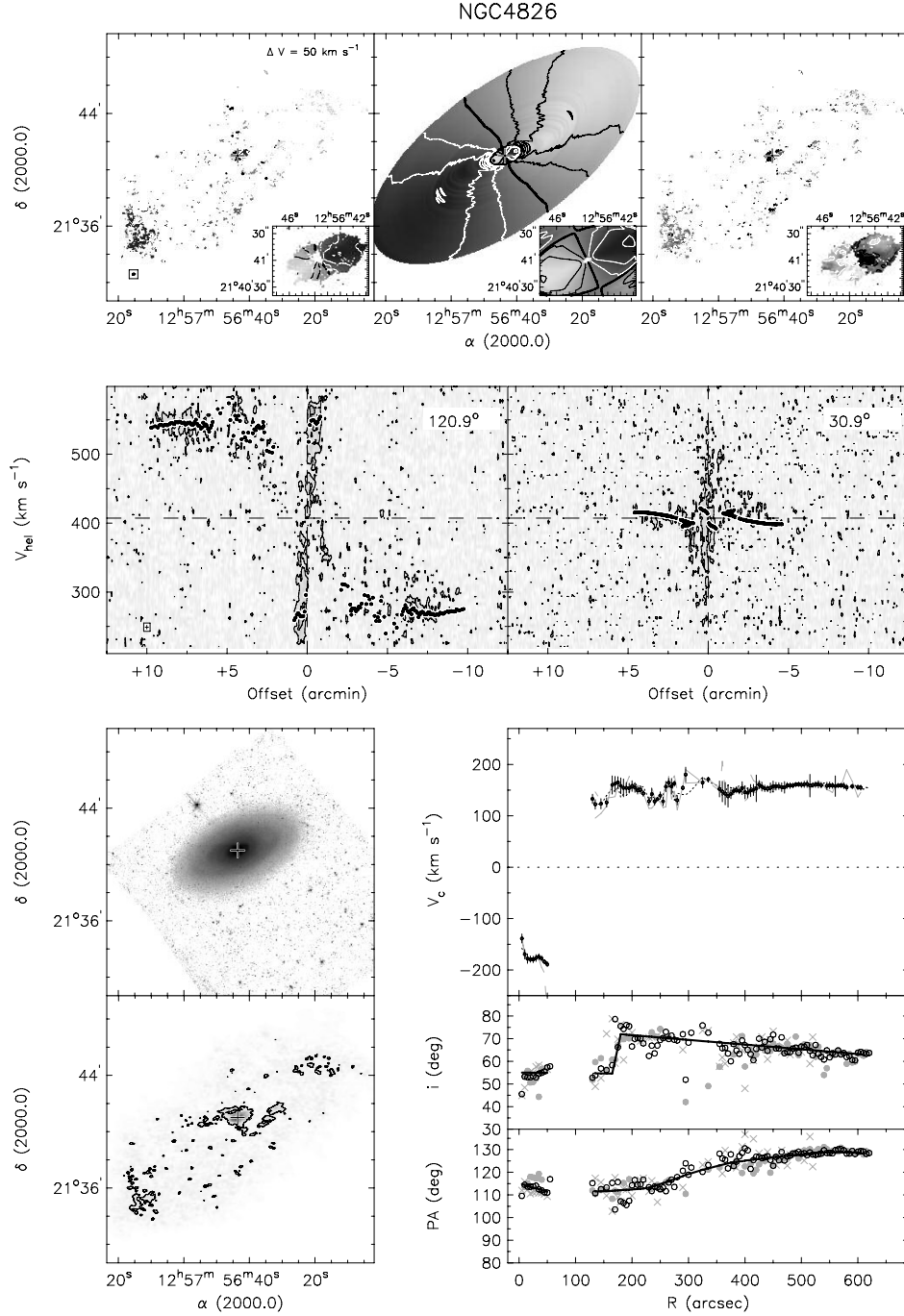


Figure 82. Summary panel for NGC 4826. See the [Appendix](#) for more information.

V_{sys} to the average value for $R < 250''$ and $R > 450''$ and get $V_{\text{sys}} = 803.5 \pm 4.5 \text{ km s}^{-1}$. This choice for V_{sys} leads to a rotation curve which shows a large difference between approaching and receding sides at the intermediate radii.

NGC 3621. NGC 3621 is a late-type spiral with an H_I distribution that is characterized by a regularly rotating disk and a warp in the line-of-sight (see the channel maps presented in Walter et al. 2008). This feature is also visible in the major-axis position–velocity diagram, as shown on Figure 78. To derive the velocity field of the disk component only, we blanked all

emission associated with the warp prior to deriving the velocity field. This velocity field and the associated integrated H_I map presented here, therefore, only show the disk component. For the full velocity field and H_I map see Walter et al. (2008). After fixing the position of the center, we find V_{sys} to be on average constant with radius. Small variations with a maximum amplitude of $\sim 5 \text{ km s}^{-1}$ are visible, but show no systematic trends with radius. We adopt the average value over the entire radial range as our best value: $V_{\text{sys}} = 728.5 \pm 2.7 \text{ km s}^{-1}$. This is consistent with the central value of 730.1 (728.8) km s^{-1} as

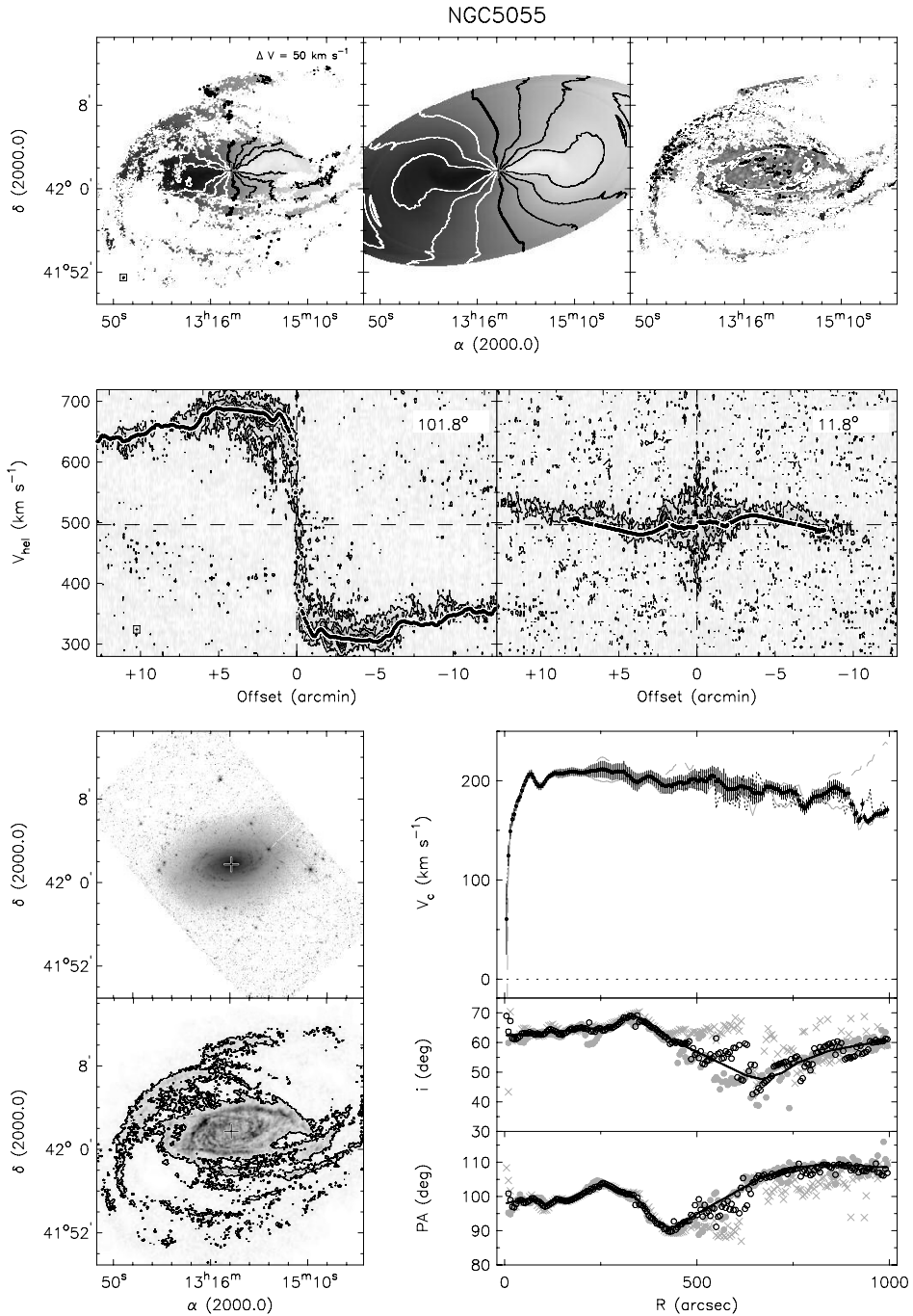


Figure 83. Summary panel for NGC 5055. See the [Appendix](#) for more information.

derived from the global H_I profile at the 20 (50)% level. The P.A. is well defined, and varies only slightly with radius. The inclination shows significant variations, but in general decreases with radius.

NGC 3627. NGC 3627, or M66, is a barred, interacting spiral galaxy that is part of the Leo Triplet. Our analysis of this galaxy is illustrated in Figure 79. The IRAC 3.6 μm image shows a pronounced bar, with a two-armed, asymmetric spiral structure. The western arm is also clearly visible in the integrated H_I map. The eastern arm is confused with other high-column density features. The pronounced spiral arms and asymmetry

of NGC 3627 do not make this a prime candidate for detailed studies that assume azimuthal symmetry. In the central parts, the H_I column density lies below the 3 σ level that we applied during the profile fitting, hence the absence of velocity information there. After fixing the position of the dynamical center, we fix P.A. and i to indicative values of 175° and 60°, respectively, and find V_{sys} values that vary slightly within $R \sim 100''$, but are constant outside that radius. We use the mean value for $R > 100''$ and find $V_{\text{sys}} = 708.2 \pm 1.1 \text{ km s}^{-1}$. This differs somewhat from the 20 (50)% level central value derived from the global H_I profile of 717.3 (720.3) km s^{-1} , but given the

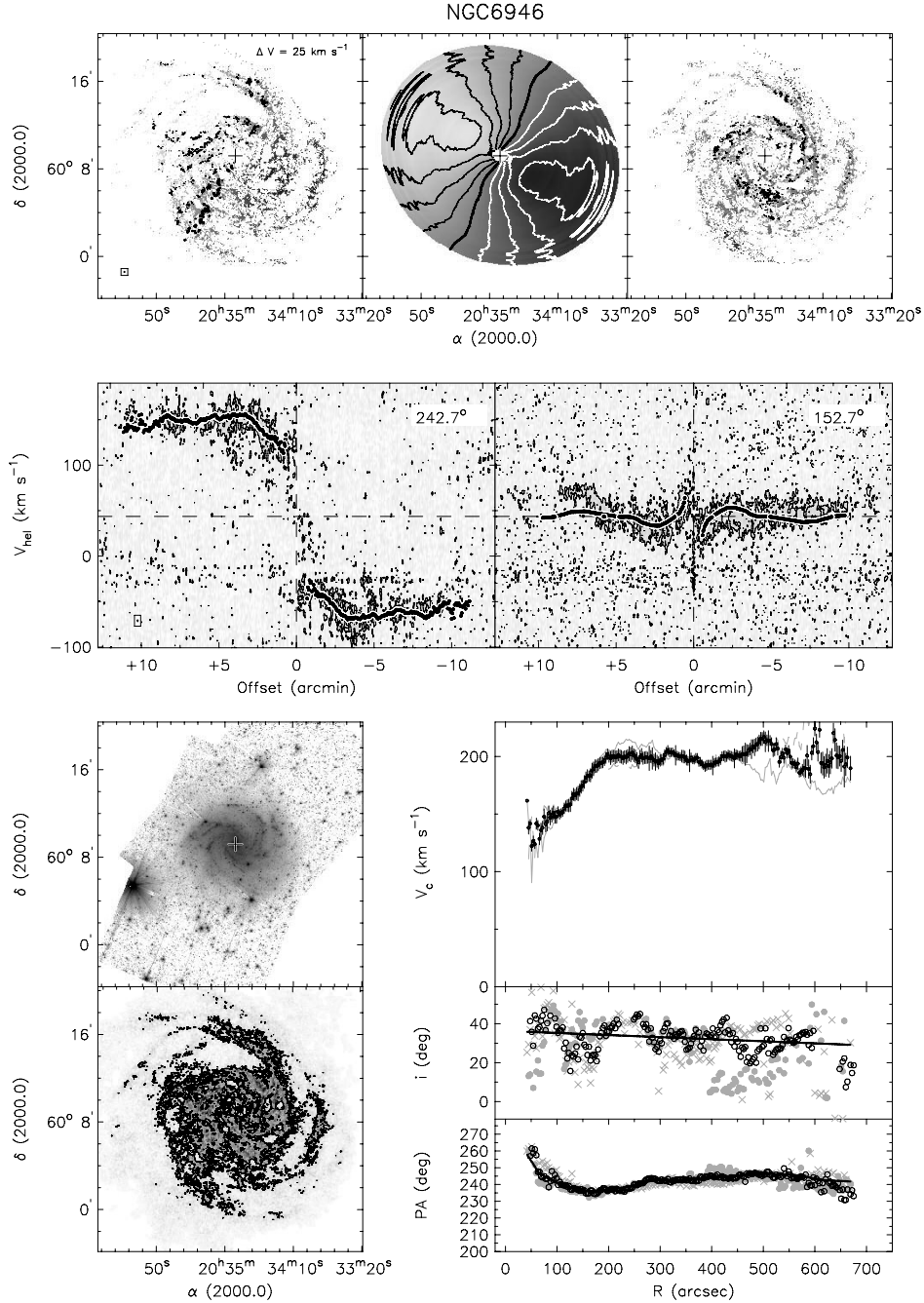


Figure 84. Summary panel for NGC 6946. See the [Appendix](#) for more information.

asymmetry of this galaxy, this should not come as a surprise. Trends of i and P.A. with radius are fairly straightforward to determine with both parameters showing modest variations. The approaching and receding sides show different radial trends, as might have been expected from the obvious asymmetry visible in the IRAC image. Nevertheless, the respective rotation velocities converge in the outer parts, leading to a well-determined flat outer rotation curve.

NGC 4736. NGC 4736 is dominated by an inner high surface brightness disk in the IRAC 3.6 μm image as shown in Figure 80. Prominent arms are visible in the integrated H α map. After fixing the position of the dynamical center, the

systemic velocity shows no systematic trends with radius and we adopt the average value $V_{\text{sys}} = 306.7 \pm 3.7 \text{ km s}^{-1}$. This corresponds well with the values derived from the global profile at the 20 (50)% level of 307.6 (306.6) km s^{-1} . The P.A. is very well defined and constructing a model is straightforward. The i shows a well-defined trend from $\sim 45^\circ$ in the outer parts to $\sim 35^\circ$ at $R \sim 80''$. At this radius, the slope of the i steepens, and the value appears to decrease to $\sim 20^\circ$ in the center. We consider this break in the i slope not physical; the inner region of NGC 4736 is known to be a region of noncircular motions and the radius where the break occurs coincides with the radius of the inner star formation ring (the “expanding H II regions

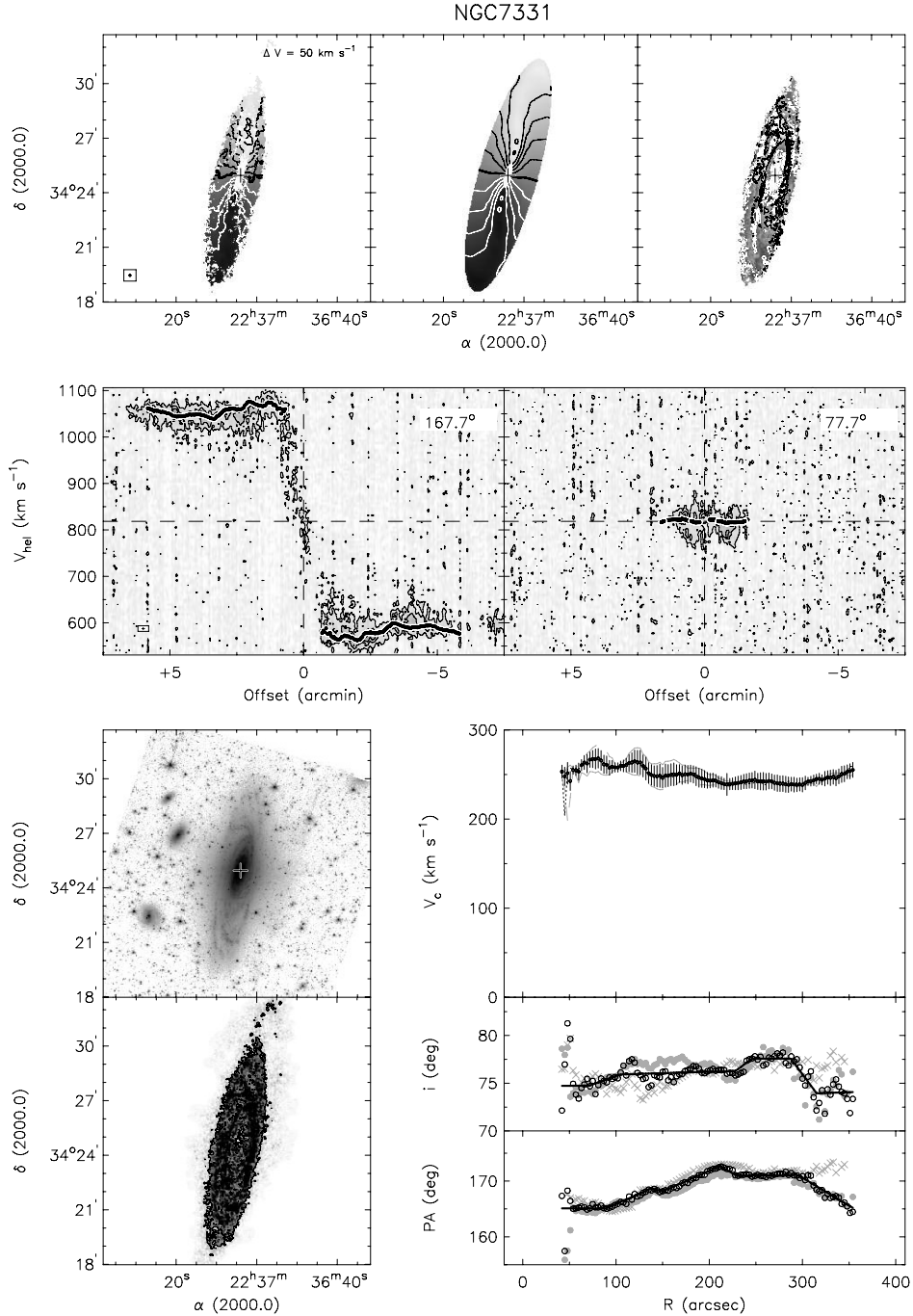


Figure 85. Summary panel for NGC 7331. See the [Appendix](#) for more information.

ring” described in Muñoz-Tuñón et al. (2004). The minor-axis position–velocity diagram also shows clear evidence for strong noncircular motions in the inner arc-minute. For our inclination model, we simply extrapolate inward the trend found for $R > 80''$. Despite the disturbed distribution of the H_I, the approaching and receding sides of the final rotation curve are remarkably similar. The velocity systematically decreases with radius: it peaks at $V = 211 \text{ km s}^{-1}$, and declines to $V = 115 \text{ km s}^{-1}$ in the outermost parts. As with NGC 3627, it is clear from the morphology that the assumption of azimuthal symmetry is

not appropriate. Trachternach et al. (2008) show that NGC 4736 has the second highest noncircular motions in the current sample (after NGC 3627) and any interpretation of its rotation curve should therefore be treated with care.

DDO 154. Our analysis of DDO 154 is illustrated in Figure 81. DDO 154 has no central radio continuum source or central light concentration to help pinpoint the dynamical center. The position of the dynamical center was therefore derived purely using the velocity field (see also Trachternach et al. 2008). The systemic velocity shows a stable

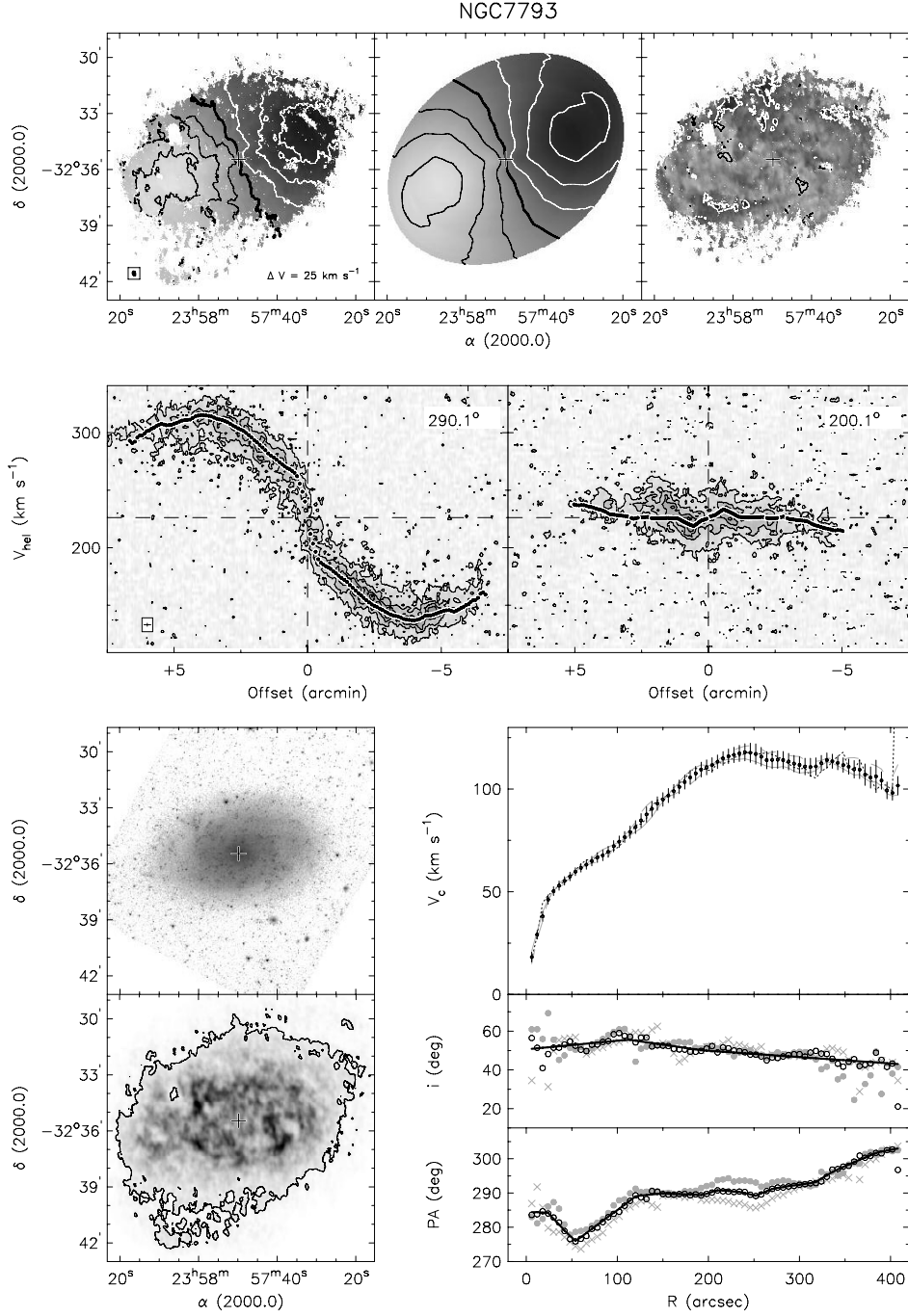


Figure 86. Summary panel for NGC 7793. See the [Appendix](#) for more information.

behavior. Using the average value within $R = 260''$ we find $V_{\text{sys}} = 375.9 \pm 1.4 \text{ km s}^{-1}$. This corresponds very well with the central values derived from the global H α profile at the 20 (50)% level of 375.5 (375.4) km s^{-1} . The P.A. is straightforward to model. The i shows some variation in the inner parts, mainly due to the small number of independent pixels per ring; here we simply extrapolated the model inwards from the smallest radius where i was well-behaved. The outer parts show an apparent steep drop in inclination. However, most of the gas contributing to these points is found in the outermost flocculent parts of the warp, and given the small filling factor of the rings there, it

is not clear how realistic this steep drop in i is. We therefore extrapolated our model outwards from the largest radii with well-determined i .

NGC 4826. As can be seen in Figure 82, the outer H α disk of NGC 4826 has a very low column density—one of the lowest in the entire THINGS sample. Only a small fraction of the disk has profiles with a peak value greater than 3σ . Nevertheless, this small filling factor, combined with the very regular kinematics in the outer disk is still sufficient to derive a well-defined outer rotation curve. Small insets in Figure 82 show the region of the counter-rotating disk, as well as the corresponding model and

residual velocity fields in more detail. After fixing the position of the dynamical center, we find no systematic trends of the systemic velocity with radius, and adopt the average value: $V_{\text{sys}} = 407.4 \pm 7.0 \text{ km s}^{-1}$. This value corresponds very well with the central value of 407.9 km s^{-1} as derived from the global H α profile for both the 20 and 50% level. The inclination and P.A. show clear trends with radius. A good description for the inclination is a constant value of $\sim 55^\circ$ in the inner parts, followed by break and a sudden increase to $\sim 70^\circ$ at $R \sim 180''$, in turn followed by a gradual decline in the outer parts to a value of $\sim 63^\circ$.

NGC 5055. As illustrated in Figure 83, the major-axis position–velocity diagram shows evidence for the presence of gas at velocities lower than the local rotation velocity. The structure of NGC 5055 as seen in the $3.6 \mu\text{m}$ image is regular, with signs of well-defined flocculent spiral arms. After fixing the position of the dynamical center we find that the systemic velocity shows a systematic variation, from a constant value of $\sim 496 \text{ km s}^{-1}$ within $R \lesssim 200''$ to a value of $\sim 510 \text{ km s}^{-1}$ in the outer parts. We make the assumption that the gas in the inner parts is likely to be more tightly bound to the system than the tenuous outer arms, and adopt the average value between $50'' < R < 180''$. We find $V_{\text{sys}} = 496.8 \pm 0.7 \text{ km s}^{-1}$. The central velocity as derived from the global profile at the 20 (50%) level is 499.3 (497.4) km s^{-1} . The P.A. and i values are well-defined for the inner H α disk. The distributions for the approaching and receding sides of the outer warped part differ significantly, leading to different approaching and receding rotation curves for $R \gtrsim 250''$.

NGC 6946. Our analysis of NGC 6946 is illustrated in Figure 84. For the position of the dynamical center we adopt the position of the central radio continuum source. The systemic velocity is fairly constant with radius. We adopt the average value within $500''$ of $V_{\text{sys}} = 43.7 \pm 3.3 \text{ km s}^{-1}$. This agrees well with the central value of 42.0 (45.1) km s^{-1} derived from the 20 (50)% level of the global H α profile. The P.A. is well-behaved and straightforward to describe. The inclination, when left free, shows a large scatter, showing the increased difficulty of determining the inclination using only dynamical information at low inclination values. Nevertheless, the large number of independent data points allow us to accurately model it as a linear radial dependence. The assumption we make is that the scatter around this average value is caused by small noncircular motions that have a disproportionately large influence due to the low inclination. Due to this inclination scatter we do not consider here the rotation curve derived using P.A. and i as free parameters.

NGC 7331. We illustrate our analysis of NGC 7331 in Figure 85. The velocity field, though regular on large scales, shows many wiggles in the velocity contours, often coinciding with the positions of the spiral arms. After fixing the position of the dynamical center, we find that the systemic velocity is well defined over the range $80'' < R < 280''$. Between $80''$ and $200''$ it varies systematically from $\sim 830 \text{ km s}^{-1}$ to $\sim 805 \text{ km s}^{-1}$, settling on a constant value of $818.3 \pm 0.9 \text{ km s}^{-1}$ between $200'' < R < 280''$. We have chosen the latter value as our V_{sys} value, comparing favorably with the central velocity from the global profile of 815.7 (816.5) km s^{-1} as measured at the 20 (50)% level. The varying V_{sys} value could indicate a kinematic lopsidedness (e.g., Schoenmakers et al. 1997; Schoenmakers 1999). A harmonic analysis of the velocity field to quantify this is presented in Trachternach et al. (2008). In the outer parts the P.A. values for approaching and receding sides

differ distinctly. At $R \sim 150''$ the inclinations are different as well, most likely due to streaming motions along the spiral arms. These show up clearly in the residual velocity field. Also note the large difference between the rotation curves of approaching and receding sides within $R \lesssim 200''$. The typical difference is $\sim 25 \text{ km s}^{-1}$, and shows why V_{sys} is difficult to constrain over this radial range. The major axis position–velocity diagram shows some H α outlining the rising part of the rotation curve, but the emission is too faint to fit a rotation curve. NGC 7331 was previously observed in H α by Begeman (1987), who already noted many of the features we have described above. The dynamical center as determined by Begeman (1987), coincides with ours to within the errors. Begeman (1987) also notes the same varying V_{sys} in the inner parts. He determines V_{sys} using only points at $R > 210''$ and finds a value $820.1 \pm 2.7 \text{ km s}^{-1}$. For the P.A., a trend very similar to ours was found. The trend we find in the inclination distribution is also present in the Begeman (1987) data, but with the much smaller number of resolution elements in that data set, a constant inclination model was chosen there.

NGC 7793. As shown in Figure 86, the velocity field of NGC 7793 is well defined with indications of a small-amplitude warp. The major-axis slice shows little evidence for extensive noncircular motions. The residuals are small, and prominent in only a few small areas in the outermost part of the disk. After fixing the position of the dynamical center we find the systemic velocity to be well defined: we adopt the average value between $40'' < R < 250''$ and find $V_{\text{sys}} = 226.2 \pm 1.2 \text{ km s}^{-1}$, agreeing well with a central velocity of 227.2 (226.6) km s^{-1} as derived from the global profile at the 20 (50)% level. The P.A. and i values are straightforward to model: the P.A. is well defined; the inclination shows a modest increase in the inner parts, followed by a gradual decline in the outer parts. The curve as derived with i and P.A. as free parameters is within the uncertainties equal to the one with i and P.A. fixed to their model values.

REFERENCES

- Battaglia, G., Fraternali, F., Oosterloo, T., & Sancisi, R. 2006, *A&A*, **447**, 49
- Begeman, K. 1987, PhD thesis, Univ. of Groningen
- Begeman, K. G. 1989, *A&A*, **223**, 47
- Bell, E. F., & de Jong, R. S. 2001, *ApJ*, **550**, 212
- Bell, E. F., McIntosh, D. H., Katz, N., & Weinberg, M. D. 2003, *ApJS*, **149**, 289
- Böker, T., Laine, S., van der Marel, R. P., Sarzi, M., Rix, H.-W., Ho, L. C., & Shields, J. C. 2002, *AJ*, **123**, 1389
- Boomsma, R. 2007, PhD thesis, Univ. of Groningen
- Bosma, A. 1978, PhD thesis, Univ. of Groningen
- Bosma, A. 1981, *AJ*, **86**, 1825
- Bottema, R. 1997, *A&A*, **328**, 517
- Bottema, R., Pestalba, J. L. G., Rothberg, B., & Sanders, R. H. 2002, *A&A*, **393**, 453
- Braun, R., Walterbos, R. A. M., Kennicutt, R. C., & Tacconi, L. J. 1994, *ApJ*, **420**, 558
- Broeils, A. H. 1992, PhD thesis, Univ. of Groningen
- Bullock, J. S., Kolatt, T. S., Sigad, Y., Somerville, R. S., Kravtsov, A. V., Klypin, A. A., Primack, J. R., & Dekel, A. 2001, *MNRAS*, **321**, 559
- Carignan, C., & Beaulieu, S. 1989, *ApJ*, **347**, 760
- Carignan, C., Charbonneau, P., Boulanger, F., & Viallefond, F. 1990, *A&A*, **234**, 43
- Carignan, C., & Freeman, K. C. 1988, *ApJ*, **332**, L33
- Carignan, C., & Puche, D. 1990, *AJ*, **100**, 394
- Carignan, C., & Purton, C. 1998, *ApJ*, **506**, 125
- Casertano, S., & van Gorkom, J. H. 1991, *AJ*, **101**, 1231
- de Blok, W. J. G. 2004, in IAU Symp. 220, Dark Matter in Galaxies, ed. S. D. Ryder et al. (Dordrecht: Kluwer), 69
- de Blok, W. J. G., & Bosma, A. 2002, *A&A*, **385**, 816
- de Blok, W. J. G., & McGaugh, S. S. 1997, *MNRAS*, **290**, 533
- de Blok, W. J. G., McGaugh, S. S., & Rubin, V. C. 2001, *AJ*, **122**, 2396

- de Blok, W. J. G., McGaugh, S. S., & van der Hulst, J. M. 1996, MNRAS, **283**, 18
 de Jong, R. S. 1996, A&A, **313**, 377
 Diemand, J., Zemp, M., Moore, B., Stadel, J., & Carollo, C. M. 2005, MNRAS, **364**, 665
 Fraternali, F., van Moorsel, G., Sancisi, R., & Oosterloo, T. 2002, AJ, **123**, 3124
 Gentile, G., Burkert, A., Salucci, P., Klein, U., & Walter, F. 2005, ApJ, **634**, L145
 Gentile, G., Tonini, C., & Salucci, P. 2007, A&A, **467**, 925
 Hayashi, E., et al. 2004, MNRAS, **355**, 794
 Hunter, D. A., van Woerden, H., & Gallagher, J. S. 1999, AJ, **118**, 2184
 Jarrett, T. H., Chester, T., Cutri, R., Schneider, S., & Huchra, J. P. 2003, AJ, **125**, 525
 Kamphuis, J., & Sancisi, R. 1993, A&A, **273**, L31
 Kennicutt, R. C., Jr., et al. 2003, PASP, **115**, 928
 Klypin, A., Kravtsov, A. V., Bullock, J. S., & Primack, J. R. 2001, ApJ, **554**, 903
 Kormendy, J., & Freeman, K. C. 2004, in IAU Symp. 220, Dark Matter in Galaxies, ed. S. D. Ryder et al. (Dordrecht: Kluwer), 377
 Kregel, M., van der Kruit, P. C., & de Grijs, R. 2002, MNRAS, **334**, 646
 Kregel, M., & van der Kruit, P. C. 2004, MNRAS, **352**, 787
 Kroupa, P. 2001, MNRAS, **322**, 231
 Kuzio de Naray, R., McGaugh, S. S., de Blok, W. J. G., & Bosma, A. 2006, ApJS, **165**, 461
 Leroy, A., Walter, F., Brinks, E., Bigiel, F., de Blok, W. J. G., Madore, B., & Thornley, M. D. 2008, AJ, **136**, 2782
 Marchesini, D., D'Onghia, E., Chincarini, G., Firmani, C., Conconi, P., Molinari, E., & Zucca, A. 2002, ApJ, **575**, 801
 McGaugh, S. S., & de Blok, W. J. G. 1998, ApJ, **499**, 41
 McGaugh, S. S., de Blok, W. J. G., Schombert, J. M., Kuzio de Naray, K., & Kim, J. H. 2007, ApJ, **659**, 149
 Moore, B. 1994, Nature, **370**, 629
 Moore, B., Ghigna, S., Governato, F., Lake, G., Quinn, T., Stadel, J., & Tozzi, P. 1999, ApJ, **524**, L19
 Moore, B., Quinn, T., Governato, F., Stadel, J., & Lake, G. 1999, MNRAS, **310**, 1147
 Mulder, P. S. 1995, A&A, **303**, 57
 Muñoz-Tuñón, C., Caon, N., & Aguerri, J. A. L. 2004, AJ, **127**, 58
 Navarro, J. F., Frenk, C. S., & White, S. D. M. 1996, ApJ, **462**, 563
 Navarro, J. F., Frenk, C. S., & White, S. D. M. 1997, ApJ, **490**, 493
 Navarro, J. F., et al. 2004, MNRAS, **439**, 1039
 Noordermeer, E., van der Hulst, J. M., Sancisi, R., Swaters, R. S., & van Albada, T. S. 2007, MNRAS, **376**, 1513
 Oh, S.-H., de Blok, W. J. G., Walter, F., Brinks, E., & Kennicutt, R. C., Jr. 2008, AJ, **136**, 2761
 Pahre, M. A., Ashby, M. L. N., Fazio, G. G., & Willner, S. P. 2004, ApJS, **154**, 235
 Paturel, G., Petit, C., Prugniel, P., Theureau, G., Rousseau, J., Brouty, M., Dubois, P., & Cambrésy, L. 2003, A&A, **412**, 45
 Pisano, D. J., Wilcots, E. M., & Elmegreen, B. G. 1998, AJ, **115**, 975
 Planesas, P., Colina, L., & Perez-Olea, D. 1997, A&A, **325**, 81
 Regan, M. W., et al. 2004, ApJS, **154**, 204
 Rhee, G., Valenzuela, O., Klypin, A., Holtzman, J., & Moorthy, B. 2004, ApJ, **617**, 1059
 Rix, H.-W. R., Kennicutt, R. C., Jr., Braun, R., & Walterbos, R. A. M. 1995, ApJ, **438**, 155
 Roberts, M. S., & Haynes, M. P. 1994, ARA&A, **32**, 115
 Rubin, V. C., Thonnard, N., & Ford, W. K., Jr. 1978, ApJ, **225**, L107
 Sargent, W. L. W., Sancisi, R., & Lo, K. Y. 1983, ApJ, **265**, 711
 Salpeter, E. E. 1955, ApJ, **121**, 161
 Sancisi, R., & Allen, R. J. 1979, A&A, **74**, 73
 Schoenmakers, R. H. M. 1999, PhD thesis, Univ. of Groningen
 Schoenmakers, R. H. M., Franx, M., & de Zeeuw, P. T. 1997, MNRAS, **292**, 349
 Shostak, G. S. 1973, A&A, **24**, 411
 Sicking, F. J. 1997, PhD thesis, Univ. of Groningen
 Simon, J. D., Bolatto, A. D., Leroy, A., & Blitz, L. 2003, ApJ, **596**, 957
 Simon, J. D., & Geha, M. 2007, ApJ, **670**, 313
 Sofue, Y., & Rubin, V. 2001, ARA&A, **39**, 137
 Spano, M., Marcelin, M., Amram, P., Carignan, C., Epinat, B., & Hernandez, O. 2008, MNRAS, **383**, 297
 Spergel, D. N., et al. 2007, ApJS, **170**, 377
 Stil, J. M., & Israel, F. P. 2002, A&A, **389**, 42
 Swaters, R. A. 1999, PhD thesis, Univ. of Groningen
 Swaters, R. A., Madore, B. F., & Trehewella, M. 2000, ApJ, **531**, L107
 Swaters, R. A., Madore, B. F., van den Bosch, F. C., & Balcells, M. 2003, ApJ, **583**, 732
 Tegmark, M., et al. 2004, Phys. Rev. D, **69**, 103501
 Teuben, P. J., & Sanders, R. H. 1985, MNRAS, **212**, 257
 Trachternach, C., de Blok, W. J. G., Walter, F., Brinks, E., & Kennicutt, R. C., Jr. 2008, AJ, **136**, 2720
 van Albada, T. S., Bahcall, J. N., Begeman, K., & Sancisi, R. 1985, ApJ, **295**, 305
 van Albada, T. S., & Sancisi, R. 1986, Phil. Trans. R. Soc. Lond. A, **320**, 447
 van den Bosch, F. C., Robertson, B. E., Dalcanton, J. J., & de Blok, W. J. G. 2000, AJ, **119**, 1579
 van der Hulst, J. M. 1997, A&A, **75**, 97
 van der Hulst, J. M., Terlouw, J. P., Begeman, K. G., Zwitser, W., & Roelfsema, P. R. 1992, in ASP Conf. Ser. 25, Astronomical Data Analysis Software and Systems I, ed. D. M. Worrall, C. Biemsderfer, & J. Barnes (San Francisco, CA: ASP), 131
 van der Kruit, P. C., & Searle, L. 1981a, A&A, **95**, 105
 van der Kruit, P. C., & Searle, L. 1981b, A&A, **95**, 116
 van der Marel, R. P., & Franx, M. 1993, ApJ, **407**, 225
 Verheijen, M. A. W. 1997, PhD thesis, Univ. of Groningen
 Visser, H. C. D. 1978, PhD thesis, Univ. of Groningen
 Visser, H. C. D. 1980, A&A, **88**, 149
 Walter, F., & Brinks, E. 1999, AJ, **118**, 273
 Walter, F., Weiss, A., Martin, C., & Scoville, N. 2002, AJ, **123**, 225
 Walter, F., et al. 2008, AJ, **136**, 2563
 Weldrake, D. T. F., de Blok, W. J. G., & Walter, F. 2003, MNRAS, **340**, 12
 Yun, M. S., Ho, P. T. P., & Lo, K. Y. 1994, Nature, **372**, 530